



Department of Applied Physics
Fluids and Flows Research Group
Science and Technology of Nuclear Fusion Research Group



Studying the Region of Magnetised Plasmas Near a Solid Surface

Master Thesis

Samuel Zeegers

Daily Supervisors: dr. Alessandro Geraldini (EPFL)
dr. Stephan Brunner (EPFL)

Academic Supervisors: prof. dr. Federico Toschi (TU/e)
dr. Josefine H.E. Proll (TU/e)

Committee Members: Prof. dr. Federico Toschi
dr. Josefine H.E. Proll
prof. dr. Guido Huijsmans
dr. Alessandro Corbetta
dr. ir. Michael A.R. Abdelmalik

Final version

Eindhoven, July 2022

Abstract

Turbulent transport is the main driving force of energy loss in a magnetically confined nuclear fusion reactor. Therefore, it is important to understand and predict turbulent transport. This is usually simulated using gyrokinetic codes; however, these codes cannot correctly resolve the boundary layer of the magnetised plasma: the magnetised sheath. The magnetised sheath consists of two regions: the Debye sheath and the magnetic presheath. The Debye sheath is a small positively charged region of a few Debye lengths, while the magnetic presheath is a quasi-neutral region of a few ion Larmor radii. The scale separation of magnetic presheath and Debye sheath only holds when the ion Larmor radius in the plasma is much larger than the Debye length.

Correct boundary conditions must be imposed for gyrokinetic codes by solving the steady state in the magnetised sheath kinetically. Current codes require a considerable amount of computational time (time dependent codes) or are only valid for small angle with the magnetic field and the wall (α).

Motivated by this, a novel numerical scheme is derived and implemented that simulates the magnetic pre-sheath and magnetised sheath without having to resolve the plasma frequency. This lowers the computational time. The scheme is also valid for general α .

Analytically it is shown that on the magnetic presheath scale, the plasma must marginally satisfy the Bohm condition at the Debye sheath entrance as a condition for quasi-neutrality. It is also shown that the potential scales with \sqrt{x} (where x is the distance from the wall) close to the Debye sheath entrance. Hence, there is a field singularity paired with the Bohm condition.

The novel numerical scheme is shown to be consistent with an existent code that simulates the magnetic presheath, which is valid for small α . Self-consistent quasi-neutral potential profiles are observed for all angles α in the magnetic presheath. It is shown that the solution of the small-angle code and the solution of numerical scheme start to deviate when $\alpha \sim 0.1$ rad. In the simulations for the entire magnetised sheath, the correct physics is reproduced by the self-consistent potential obtained from the code: a quasi-neutral magnetic presheath and a charged Debye sheath are observed. The solutions of the magnetised sheath converge to the solutions of the magnetic presheath when the fraction $\lambda_D/\rho_i \rightarrow 0$. Lastly, highly localised distribution functions at the wall are observed; the more shallow the angle α , the more localised the distribution function.

Acknowledgements

First and foremost I would like to thank my supervisor, Alessandro Geraldini. I could not have wished for a better supervisor, you have taught me a lot. Thank you for all the time you spend to help me and the long and interesting discussions we had. I am truly grateful that I was supervised by you. Then I would like to thank my other supervisor, Stephan Brunner for always showing interest in the project, joining many of the meetings I had with Alessandro and the good suggestions he provided. I would also like to thank Cristian Sommariva with help on optimizing my code. I would like to thank Federico Toschi and Josefina Proll for giving me the opportunity to do the project abroad, and for providing useful feedback during the project and on the report.

Thank you, to all the people at SPC who created an environment that was both pleasant to work in. I never experienced such a nice atmosphere in a scientific lab. Lastly, I would like to thank my family and friends without whom I wouldn't have been able to reach this point in my studies. You always kept me motivated. Zelda and Storm, thank you for reading my science communication product and providing me with useful feedback.

This work has been carried out within the framework of the EUROfusion Consortium, funded by the European Union via the Euratom Research and Training Programme (Grant Agreement No 101052200 — EUROfusion). Views and opinions expressed are however those of the author(s) only and do not necessarily reflect those of the European Union or the European Commission. Neither the European Union nor the European Commission can be held responsible for them.

Contents

1	Introduction	1
2	Theoretical background	4
2.1	Magnetic confinement fusion	4
2.2	Plasma physics	5
2.3	Plasma interacting with a wall	6
2.4	Kinetic theory	8
2.5	The Debye sheath	9
2.5.1	Fluid treatment	9
2.5.2	Kinetic treatment	10
2.6	The magnetised sheath	10
2.6.1	Fluid treatment	10
2.6.2	Kinetic treatment	11
3	Methods	16
3.1	Analytical description of the magnetic presheath	16
3.2	Calculating the ion density	18
3.3	Particle integration	20
3.4	Velocity sampling and entrance conditions	21
3.5	Self-consistent potential	26
3.5.1	Magnetic presheath	26
3.5.2	Magnetised sheath	27
3.6	Definition of the spatial grid	28
3.6.1	Magnetic presheath	28
3.6.2	Magnetised sheath	29
3.7	Speeding up the code	29
3.7.1	Parallelisation	30
3.7.2	Piece-wise constant electric field	31
4	Results and discussion	40
4.1	Shape of potential close to the wall and Bohm condition	40
4.2	Magnetic presheath simulations	46
4.3	Magnetised sheath simulations	52
4.4	General discussion	61
5	Conclusion	63
6	Outlook	64
A	Density Contribution Single Gryo-Ring	66

List of Figures

1.1 Schematic figure of tokamak and cross-section	2
1.2 Boundary layers of magnetised plasma	2
2.1 Debye sheath entrance in magnetised sheath	7
2.2 Effective potential curves	14
2.3 Phase space ion trajectories going from closed to open orbit	15
3.1 Incoming ion distribution at magnetic presheath entrance	17
3.2 Basis functions	19
3.3 Velocity coordinate system	21
3.4 Different type of trajectories in the magnetic presheath	22
3.5 Different type of trajectories close to the magnetic presheath entrance	23
3.6 Density contribution for a particle with and without turning points	25
3.7 Density contribution of gyroring in magnetic presheath without an electric field	26
3.8 Numerical potential profile obtained for linear grid spacing	29
3.9 Finite element representation of a function that goes with \sqrt{x}	30
3.10 Difference between dynamic and static scheduling	31
3.11 Possible $x(t)$ curves in a specific grid cell	32
3.12 Decision flow chart for finding t_a and t_b	33
3.13 Different $v_x(t)$ curves for particles with $v_x(0) > 0$ inside a grid cell	34
3.14 Decision flow chart of finding t_{left} and t_{right} for particles with $v_x(0) > 0$	35
3.15 Different $v_x(t)$ curves for particles with $v_x(0) < 0$	36
3.16 Decision flow chart of finding t_{left} and t_{right} for particles with $v_x(0) < 0$	37
4.1 Results of numerical method in the magnetic presheath for $\alpha = 1.8^\circ$	47
4.2 Results numerical method of magnetic presheath for different α	48
4.3 Distribution functions in the magnetic presheath as a function of v_x for different α	49
4.4 Distribution functions in the magnetic presheath as a function of v_y and v_z for different α	50
4.5 Distribution functions in the magnetic presheath as a function of v_x and v_z for different α	51
4.6 Potential profile in magnetic presheath for different α compared to small α potential profiles	52
4.7 Results of numerical method in the magnetised sheath for different α	53
4.8 Density of magnetised sheath in the Debye sheath region	54
4.9 Potential profiles in magnetised sheath approaching magnetic presheath solution when $\gamma \rightarrow 0$	55
4.10 Distribution functions in magnetised sheath approaching magnetic presheath solution when $\gamma \rightarrow 0$	56
4.11 Distribution function hitting solid target for different α as function of θ and ψ	57
4.12 Distribution function hitting solid target for specific v for different α as function of θ and ψ	59
4.13 Distribution function hitting solid target for different α as function of E and θ	60
A.1 Schematic used to calculate gyroring density contribution	66

List of Tables

1	Conditions for the distribution functions	49
---	---	----

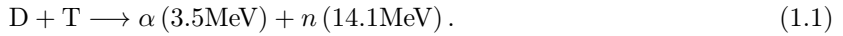
List of Algorithms

1	Algorithm for calculating τ	39
---	----------------------------------	----

1 Introduction

Humanity should act quickly to combat climate change before it is too late. The 2021 IPCC report shows projections that require joined effort from all the nations [1]. One of the main problems is the need to generate energy efficiently without emitting greenhouse gases. At this point, there are several available options, of which the most famous are: nuclear fission, wind, and solar energy. Nuclear fission produces radioactive waste, which is a problem itself, while wind and solar might have a problem of low energy density unless they become more efficient [2]. It has to be said that these problems are nothing compared to the problems caused by the production of gray energy [3]. Another possible way to generate green energy is nuclear fusion, which generates nuclear energy but fuses nuclei instead of splitting them as is done in nuclear fission. This does not generate heavy radioactive waste, and it is energy-dense. The large number of fusion reactions to produce net energy can only be achieved at very high temperatures, at which matter exists in the state of an ionised gas of electrons and ions. This ionised gas is known as plasma. Containing the plasma is one of the challenges in making nuclear fusion a reality.

Building a fusion reactor is often referred to as building the Sun on Earth. There are, however, some differences between a proposed fusion reactor and the fusion happening in the Sun. Most importantly, the way fusion reactions are produced is different. In a reactor, the power is generated by reactions between deuterium and tritium. These are chosen because they have the highest reaction rate for the lowest temperature, but for them to fuse efficiently, the temperature in the reactor should be around 15 keV (around 200 million Kelvin) [4]. The reaction is given by:



Here D stands for deuterium and T for tritium, α stands for the helium 4 nucleus that is formed, n stands for the neutron that is formed in the reaction, and the kinetic energy of the reactants is given by the numbers in the brackets. It is important to keep the deuterium and the tritium inside the reactor. They should also be close enough for the probability of particles overcoming the Coulomb barrier to be high enough. The process of keeping the "fuel" close together such that fusion reactions can happen is called confinement. In the Sun this is achieved by gravitational force¹, but this is not possible on Earth. A fusion reactor is likely going to be magnetically confined. Magnetic fields, which close back onto themselves in a doughnut-shaped, or toroidal, configuration are used. Due to the Lorentz force, charged particles closely follow the magnetic field lines, wrap around a toroidal surface. The particles are then confined around the torus. In practice, particle confinement is imperfect due to drifts, instabilities, and turbulence, and more ingenuity is required. Because the confinement is imperfect the particles travel slowly perpendicular to the magnetic field line and they will eventually leave the confinement region, this happens at a location called the divertor at the bottom of the reactor. All the magnetic field lines are lead towards this location; there, the particles hit a solid surface made out of tungsten, so-called target plates. A nuclear fusion reactor of the tokamak type is shown in Figure 1.1.

It is important to control the plasma parameters in such a way that a competitive power plant² efficiency is ensured. A big problem is keeping the plasma from cooling down. The plasma cools down due to across-field line transport dominated by turbulent transport, which arises due to steep gradients in density and temperature. The big gradients are desirable because they allow for smaller reactors with a very hot core, to achieve fusion, and a cooler edge to not melt the fusion device. To make a working fusion reactor it is thus important to understand the turbulence that occurs in the plasma. Turbulent plasmas often are simulated using large gyrokinetic codes, which solve a 5D version of the kinetic equation of the electrons and ions that make up the plasma. A kinetic equation describes the evolution of the distribution of position (usually 3 coordinates) and velocity (3 more coordinates) of the constituent particles in a macroscopic system. In this case, the gyrokinetic equation exploits known trajectories of particles in a strong magnetic field to reduce the dimensionality of the kinetic equation from 6D to 5D. One of these codes is the GENE code, which solves the 5D Vlasov equation using Runge-Kutta methods. And it calculates the background field through a quasi-neutrality equation [8]. This equation exploits the tendency of plasma to be neutral on the large length scales of turbulent structures: a charge anywhere in the plasma is very closely surrounded by equal and opposite charges. The codes require boundary

¹The Sun also uses a different fusion reaction, proton-proton chain, which it can get away with because it has a large volume.

²although a power plant is a final goal, for now, we are still trying to sustain fusion in steady-state.

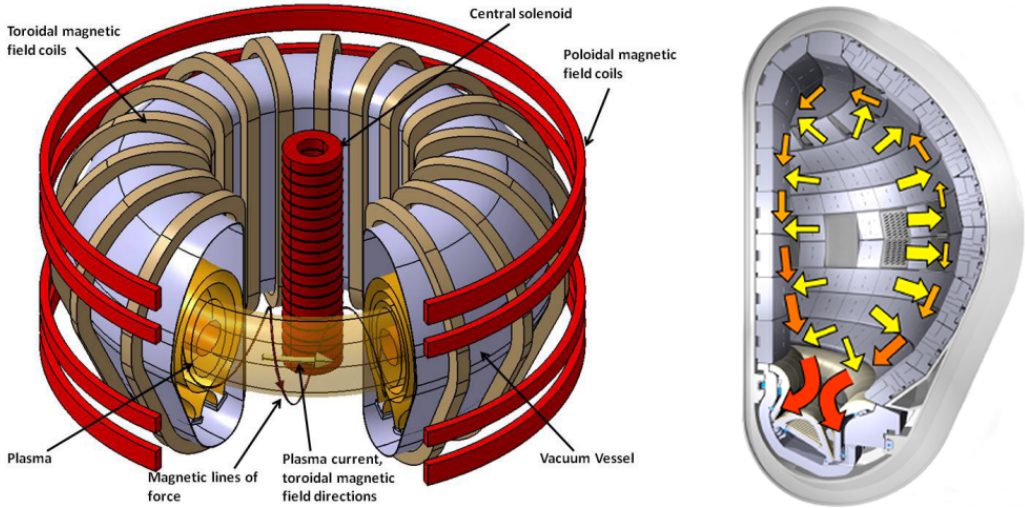


Figure 1.1: Schematic of a tokamak (left) taken from [5]. Note that the plasma is confined with toroidal and poloidal magnetic fields, creating a helical field. The field lines are directed to the divertor region below where they hit the target plates. On the right a figure taken from [6] showing a cross section with the heat fluxes towards the divertor. Most ions will hit the divertor at the bottom of the reactor.

conditions at the solid targets at the edge of the fusion device. To impose these boundary conditions, one must first understand what happens in the boundary layer, called the sheath, arising in front of the targets. Gyrokinetic codes cannot simulate the sheath system because the length and time scales important in the sheath are much smaller than the length and time scales of the gyrokinetic codes. This means that the sheath needs to be simulated separately in order to impose boundary conditions.

As stated before, it is key to understand the plasma boundary layer in a magnetised plasma. This system is known as the magnetised sheath. It consists of 2 regions: the Debye sheath and the magnetic presheath as depicted in Figure 1.2. The Debye sheath arises when any plasma interacts with a wall: it is a charged region with a strong electric field. The magnetic force in this region can be ignored. The plasma sheath has been studied since the 1920s, and a good review can be found in [9]. An important discovery in plasma sheath physics is Bohm's criterion. It states that ions can only enter the sheath when their speed is above or equal to a certain speed (Bohm's velocity). This was at first discovered with a fluid approach by Bohm [10], but later also discovered kinetically by Harrison and Thompson [11]. This implies that the ions need to be accelerated before they reach the Debye sheath. This acceleration happens in the presheath, a region where the charge density is zero. In the particular case of a magnetic presheath, the electric force and magnetic force are of similar size. The gyro-orbit of particles gets distorted in this region. Research into magnetised sheath had one of its biggest breakthroughs with the paper by Chodura [12], who discovered that ions enter the magnetic presheath at the Bohm velocity along the magnetic field line. For this report, the research by Geraldini is an important reference. With a small magnetic field angle (see angle α in Figure 1.2) expansion the author solves for a steady state electron repelling magnetic presheath. The author made a numerical model which forms the basis for this project. The

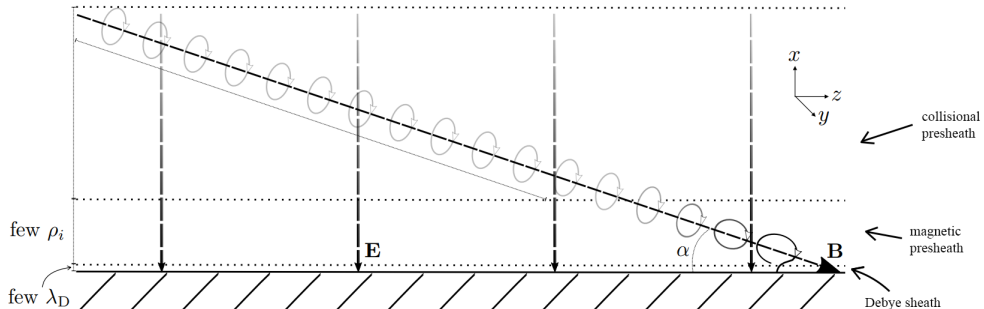


Figure 1.2: Plasma boundary layer in the presence of a magnetic field. Figure retrieved from [7].

numerical model is a way to find the steady state potential iteratively instead of by time dependence which was used in the Particle-In-Cell (PIC) method by Chodura. It is important to note that this numerical method is fast enough to generate boundary conditions more efficiently, but it is only valid for shallow angles [13, 14].

Since the sheath timescale is very fast, the codes that simulate turbulent transport in fusion devices only require steady state solutions of the sheath to impose boundary conditions. In the literature, the steady state is usually solved by solving in time, which may not be the most direct way. The approach presented in this report is a numerical method that kinetically solves for the steady state directly (in a fixed point method) for a general angle of the magnetic field with the wall. This has not been done before, and novel approaches are needed. It is similar to a method earlier used to simulate gyrotrons [15] and has several novel elements which make the method attractive for future sheath studies in fusion and other areas of plasma physics. The new method considered in this report is based on the PIC method, but it is not a PIC method because it doesn't rely on statistical sampling. It will solve the ion density for a certain guess of the electrostatic potential (ϕ) and then use the iterative solver defined in [14] to solve for the correct ϕ . This means that there will not be any time dependence and that it will only be used to find the steady state of the self-consistent potential. Furthermore, it can solve the sheath for general magnetic field angles, which makes the applications more varied. For example, Hall thrusters [16], plasma probes [17] and magnetic filters [18]. But it can also be used to check for the validity of the work by Geraldini, which was semi-analytical and valid for small angles. With the method proposed in this report, it will be possible to check what constitutes a small-enough angle to satisfy the small angle approximation of Geraldini. Furthermore, the numerical method can be extended to include more physics, like collisions, turbulence in 2D, arbitrary geometries and surface roughness.

Motivated by this the following research question is posed: **Can a numerical algorithm exploiting a fixed-point iteration directly solve for the steady state of a collisionless magnetised sheath for general magnetic field angles?** When this code is established, it is interesting to answer the following questions:

- How does the distribution function of ions reaching the solid target differ from that of ions entering the magnetised plasma sheath?
- Above what value of magnetic field angle does the existing magnetised sheath model by Geraldini, which requires a small angle between magnetic field and target, become invalid [13, 14]?
- Can the steady-state solution of the magnetised sheath be applied to develop boundary conditions for models used to simulate plasma in a fusion device?
- What functional dependency does the self consistent potential profile of a quasi-neutral magnetic presheath follow analytically close to the target?
- Can the Bohm condition be derived from the quasi neutrality condition of the magnetic presheath?

2 Theoretical background

This Section will first explain how nuclear fusion is achieved on Earth. It then will give a small background on plasma physics, after which plasma wall interactions are discussed. Then kinetic theory will be explained before going into the details of the Debye sheath. Finally, the magnetised sheath system is discussed, which is the main topic of this thesis.

2.1 Magnetic confinement fusion

It is worth understanding how nuclear fusion is achieved on Earth. Reaction 1.1 does not happen spontaneously, it requires a high activation energy. There are two main forces at play in the reaction: the coulomb force (an electromagnetic force), which repels the two hydrogen atoms preventing them from getting too close to each other, and the strong nuclear force, an attractive force between two nuclei when they are close to each other. It means that for particles to fuse, they need to be brought close together: close enough to be in the range where the strong nuclear force dominates. Thus for fusion, one needs an activation energy that is related to overcoming the coulomb "barrier"; in the Sun, this is achieved by gravity. On Earth, another trick has to be used.

This trick is heating a plasma to extremely high temperature (higher than the sun) until it is so energetic that enough particles can overcome the coulomb barrier. The most promising way to achieve these high temperatures in the plasma is by using magnetic confinement fusion. To understand which parameters are important to make fusion work, it becomes useful to look at the power balance of a thermonuclear fusion reactor. A reactor is subject to continuous energy loss that has to be balanced by heating of the plasma, which can either be self-heating or external heating. The optimal power generated by a fusion reaction is given by

$$p_{T_n} = \frac{1}{4} n^2 \langle \sigma \nu \rangle \epsilon, \quad (2.1)$$

where p_{T_n} stands for the thermonuclear power, $\langle \sigma \nu \rangle$ is the reaction rate, ϵ the energy per reaction and n the total ion density. As can be seen in Equation 1.1, about four-fifths of this power goes into the neutron, and the rest goes into the α particles. The α particles stay in the plasma, and thus the energy transferred to them will self heat the plasma. The total α heating power in the entire reactor is thus

$$\bar{P}_\alpha = \frac{V}{4} \overline{n^2 \langle \sigma \nu \rangle} \epsilon_\alpha, \quad (2.2)$$

where the bar denotes the average quantity and V the entire plasma volume. A self-sustained reactor needs to have an α particle heating that is equal to the heat loss in the reactor. The heat loss in the reactor can be written in terms of energy confinement time τ_E , which is a measure of how long the energy can stay in the plasma. The total power loss in a reactor is given by:

$$P_L = \frac{3\bar{n}T}{\tau_E} V. \quad (2.3)$$

This is because $3\bar{n}TV$ is the total Energy inside the reactor that stays in for a time τ_E . The condition for a reactor to self-sustain, assuming constant temperature and density, is:

$$n\tau_E > \frac{12}{\langle \sigma \nu \rangle} \frac{T}{\epsilon_\alpha}. \quad (2.4)$$

This is known as the Lawson criterion and is a cornerstone to making nuclear fusion a viable energy source [19]. An important parameter thus is the confinement time τ_E . A larger confinement time makes it easier to satisfy the condition. This means that a nuclear fusion reactor needs a good confinement. The confinement is achieved by magnetic fields. The charged particles of the plasma follow helical trajectories around the magnetic field lines. The radius of their circular orbit is the gyroradius (Larmor radius):

$$\rho_s = \frac{m_s v_{\perp,s}}{|q_s| B}, \quad (2.5)$$

ρ_s is the gyroradius, m_s the mass of the species s , $v_{\perp,s}$ the magnitude of the velocity perpendicular to the magnetic field line, q_s the charge of species s and B the magnitude of the magnetic field. The particles gyrate around the magnetic field line with frequency (gyrofrequency):

$$\Omega_s = \frac{q_s B}{m_s}. \quad (2.6)$$

Note that the direction of the gyration depends on the sign of the charge. The consequence of the particles having this motion in a magnetic field is that the transport perpendicular to the magnetic field line is highly reduced while the transport along the field line is barely impacted.

A simple confinement device would be a solenoidal-shaped device with the magnetic field directed through the axis of the solenoid (θ -pinch). Nuclear fusion research started with these devices, but throughout the years it became apparent that the end losses are too large to make an effective reactor. The most successful solution to this was by curving the solenoid into a toroidal shape. This shape is currently the most developed magnetically confined fusion concept. The toroidal shape however, also introduces some new problems, the magnetic field lines will be curved, and the magnetic coils winding poloidally around the torus will be spaced closer together on the inboard side than on the outboard side of the torus. Because of the latter asymmetry, there will be a gradient in the magnetic field: the field is stronger on the inboard side than on the outboard side. Both the curvature and the gradient in the magnetic field will cause the particles to drift. The particle drift velocity is given by:

$$\mathbf{v}_{d,c} = \frac{\frac{1}{2}m_s(v_{\parallel,s}^2 + v_{\perp,s}^2)}{q_s B} \frac{\mathbf{B} \times \nabla \mathbf{B}}{B^2}. \quad (2.7)$$

Here $\mathbf{v}_{d,c}$ is the drift velocity, m_s is the mass of species s , v_{\parallel} is the velocity of species s along the magnetic field, v_{\perp} is the velocity of species s perpendicular to the field line, q_s is the charge of species s , and \mathbf{B} is the magnetic field vector with magnitude B . The equation highlights that electrons and ions will drift in opposite direction. In general, if the ions drift upwards, the electrons drift downwards and vice-versa. This leads to charge separation and thus an electric field. The electric field will interact with the particle trajectories. The particles again will feel a drift due to the electric field given by:

$$\mathbf{v}_{d,\mathbf{E} \times \mathbf{B}} = \frac{\mathbf{E} \times \mathbf{B}}{B^2}. \quad (2.8)$$

This drift is not dependent on the species, and thus both the electrons and ions will drift radially outward, and confinement is lost. To solve this problem, a poloidal magnetic field must be applied that cancels these drifts. This poloidal magnetic field is generated with a current that runs toroidally in the plasma. The resulting device is called a tokamak, an illustration is shown in Figure 1.1.

2.2 Plasma physics

Plasma is often considered the 4th state of matter; the reason for this is that it simply forms by heating a gas to a high enough temperature [20]. Plasma is an ionised gas, and it is generally complex to describe. Unlike most fluids, plasmas interact with electric and magnetic fields, but the electric and magnetic fields are also changed by the particles in the plasma. Another reason for the complexity is that the plasma is so hot that the particles experience collisions on space and time scales much shorter than the scales of the applied fields or the fields generated by the plasma itself³. This makes plasmas dynamically nonlinear and difficult to analyse. Plasmas are generally described using 2 different ways:

1. Using distribution functions in kinetic theory (see Section 2.4): a microscopic description relying on statistical physics.
2. Using fluid theory: a description based on the change of macroscopic quantities. See Section 2.4 for how to retrieve the fluid quantities from the kinetic description.

It is worth iterating some important quantities and conventions that are often used in plasma physics. Naturally, in a plasma, all the quantities are dependent on the species.

The temperature T_s is generally expressed in terms of energy. For this report the temperature will be given in Joules J . Such that $T_s [J] = k_B T_s [K]$ with k_B the Boltzmann constant and T_s the temperature of species s expressed in the unit within the brackets. A common assumption is that the electron and ion temperature are equal, which means that the electrons and ions are in thermal equilibrium with each other. The temperature in the plasma is related to the normal velocity scale in the plasma known as the thermal velocity, which is given by:

$$v_{th,s} = \sqrt{\frac{T_s}{m_s}}. \quad (2.9)$$

³There are some cases where plasmas can be completely described by fluid models, usually when the plasma is cold

Now the important length and time scales in plasmas will be discussed. First, there is a characteristic length scale in which species s can travel without colliding with another particle. This is denoted by $\lambda_{mfp,s}$. The mean free path is much larger than the mean free path of particles in fluids, which is the main reason that plasma cannot generally be treated as a fluid. The important time scale related to this length scale is the collision frequency denoted by ν_s . Another important length scale for magnetised plasmas is the gyroradius, which has been introduced in Equation 2.5. The time scale related to this length scale is the gyro-frequency defined in Equation 2.6. The last and smallest length scale is the Debye length, defined by

$$\lambda_D = \sqrt{\frac{\epsilon_0 T_e}{n_e e^2}}. \quad (2.10)$$

Here n_e is the electron particle density, e the elementary charge and ϵ_0 the permittivity of free space. It is the value of a sphere's radius above which the average charge within the sphere is zero [21]. The important time scale related to this quantity is the plasma frequency, which is the frequency at which the electrons in the plasma naturally oscillate relative to the ions [22]. It is defined by:

$$\omega_{pe} = \sqrt{\frac{n_e e^2}{m_e \epsilon_0}}. \quad (2.11)$$

The Debye length is then equivalent to the thermal velocity divided by the plasma frequency. The following holds in most plasmas:

$$\begin{aligned} \lambda_D &\ll \rho_s \ll \lambda_{mfp,s}, \\ \omega_{pe} &\gg \Omega_s \gg \nu_s. \end{aligned} \quad (2.12)$$

Only when looking at the plasma from length scales that are comparable to the Debye length, the plasma appears to be charged. For length scales $l \gg \lambda_D$ the plasma appears neutral. This is known as the quasi-neutrality condition, and it is insightful to understand how this condition comes about.

In general, a plasma obeys Maxwell's equation, but since this report deals with an electrostatic plasma, the most important of those equations is Poisson's equation:

$$\nabla^2 \phi = -\frac{\rho}{\epsilon_0}. \quad (2.13)$$

Here ρ is the charge density and ϕ the potential. The potential variation across the plasma length l can be estimated to be:

$$\nabla^2 \phi \sim \frac{\phi}{l^2} \sim \left| \frac{e}{\epsilon_0} (Z n_i - n_e) \right|. \quad (2.14)$$

Here Z is the charge of the ion species, and n_i is the ion particle density. Generally in plasmas it is true that $\phi \lesssim T_e/e = \frac{e}{\epsilon_0} n_e \lambda_D^2$, where the Debye length was used. Then it is possible to write:

$$\frac{|Z n_i - n_e|}{n_e} \lesssim \frac{\lambda_D^2}{l^2}. \quad (2.15)$$

In the case where $l \gg \lambda_D$:

$$|Z n_i - n_e| \ll n_e. \quad (2.16)$$

It is then valid to set:

$$Z n_i = n_e. \quad (2.17)$$

This is known as the quasi-neutrality equation. The entire derivation breaks down, however, on small length scales, as shall be explained in further detail in Sections 2.3 and 2.5. This will be the case for a plasma close to a solid target, because in this region the sheath thickness is approximately equal to λ_D .

2.3 Plasma interacting with a wall

The plasma will eventually come into contact with the wall. When that happens, a potential difference between the wall and the bulk of the plasma builds up. The potential difference is the result of the mobility difference between electrons and ions: ions are heavier than electrons. They also have equal temperatures, and thus the electrons will move faster than the ions. More electrons hit the wall than ions in a unit time, charging the wall negatively [23] over time. There will be a thin positively charged

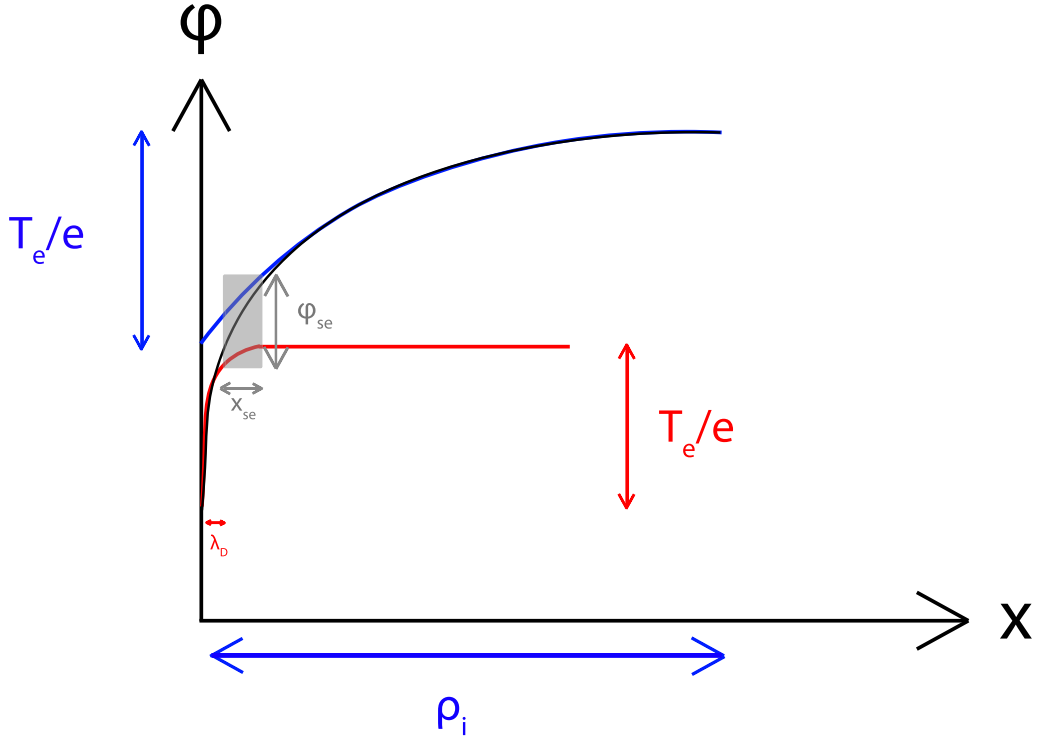


Figure 2.1: Depiction of the sheath entrance, the black line represents the self consistent potential profile of the entire magnetised sheath, the blue line represents the self consistent potential of the magnetic presheath and the red line the self consistent potential of the Debye sheath. The shaded grey region is the region where the magnetised sheath potential goes from following magnetic presheath solution to following the Debye sheath solution. This region of size x_{se} can be considered as the Debye sheath entrance. The potential drops a fraction of ϕ_{se} in this region. The scale separation between λ_D and ρ_i can be considered to be valid if $\phi_{se} \ll T_e/e$.

region where quasi-neutrality breaks down. The region is a few Debye lengths thick. At one point, a steady state is reached in which the ions and electrons have equal flux to the wall: the resulting type of diffusion is called ambipolar diffusion. At that point, the wall will not be charged more than it already had, and there will be a steady-state potential field. Not all of the potential drop occurs in a region where quasi-neutrality breaks down. There is a quasi-neutral region in which some of the potential drop occurs called the presheath. The length scale of this region λ_{ps} is much larger than the Debye length. It is generally justified to study both regions by scale separation [24, 25], taking the limit $\lambda_D/\lambda_{ps} \rightarrow 0$.

In the case that a magnetic field is normal to the wall, or if there is no magnetic field at all, the size of the pre-sheath is determined by the mean free path of the ions $\lambda_{mfp,i}$. If there is a magnetic field which is not normal to the wall, the sheath region is split up into three regions instead of two: the collisional pre-sheath, the magnetic pre-sheath and the Debye sheath. See Figure 1.2 for a depiction of the boundary layer of a magnetised plasma. The three regions: collisional presheath, magnetic presheath and Debye sheath are also shown. The collisional presheath has a length scale $\lambda_{mfp,i} \sin(\alpha)$, where α is the angle the magnetic field makes with the wall. Getting closer to the wall one will enter the magnetic presheath with length scale ρ_i (see Equation 2.5). Even closer to the wall is the Debye sheath with length scale λ_D . In this project, the plasma satisfies the following scale separation:

$$\lambda_D \ll \rho_i \ll \sin(\alpha) \lambda_{mfp,i}. \quad (2.18)$$

This physically means that the magnetic presheath can be described as being collisionless, and this is often a valid assumption. In this report, the term magnetised sheath is used to talk about the combination of magnetic presheath and Debye sheath.

It becomes convenient to define the coordinate system that is used in this report, this coordinate system is depicted in Figure 1.2. The electric field only has a component in the direction perpendicular to the wall, which is called the x direction. The magnetic field makes an angle of α with the wall in such a way

that it is defined in the x, z plane. The wall is assumed to be perfectly flat and symmetric in the y and z coordinates.

The fact that one assumes that $\lambda_D/\rho_i \rightarrow 0$ means that one understands the Debye sheath to be an infinitesimally small region in the magnetic presheath scale. Infinitesimally small means that in the scale separated regime, the Debye sheath has 0 thickness on the magnetic presheath scale. Hence, $x/\rho_i = 0$ can be treated as the entrance of the Debye sheath that has zero thickness. Looking from the Debye sheath scale, the location of the Debye sheath entrance is described by $x/\lambda_D \rightarrow \infty$. Hence, in the scale separated regime the Debye sheath entrance is well defined as a single point. This is, however, not the case if one would look at the magnetised sheath as a whole. In that case the Debye sheath entrance is actually a "fuzzy" region. To understand that it is useful to refer to Figure 2.1, in this figure a typical potential profile in the scale separated magnetic presheath is sketched in blue, the potential drop is in the order of T_e/e . A typical potential profile of the scale separated Debye sheath is sketched in red, the potential drop in the Debye sheath is also in the order of T_e/e . The black curve is the potential profile for the entire magnetised sheath. It can be seen that for large x it follows the magnetic presheath curve and for small x it follows the Debye sheath curve. The Debye sheath entrance can then be understood as the region where the magnetised sheath solution goes from following the magnetic presheath solution to following the Debye sheath solution. This highlights that the Debye sheath entrance goes from a well defined point to a region in which a potential drop occurs. The size of the region decreases (and also the potential drop in the region) when the fraction λ_D/ρ_i decreases.

It is important to note a few things about this boundary layer and the three regions. The collisional presheath is characterised by the strong magnetic force, in particular $|\mathbf{v} \times \mathbf{B}| \gg |\mathbf{E}|$. So, in this region, the particles follow the magnetic field lines while making a circular orbit around it. Importantly, gyrokinetic codes assume circular gyro-orbits and thus can simulate this region. The magnetic presheath is characterised by the fact that the magnetic force is comparable to the electric force: $|\mathbf{v} \times \mathbf{B}| \sim |\mathbf{E}|$. This in turn, means that the circular gyro-orbits get distorted, and they are transitioning from circular gyro-orbits to non-circular and finally open orbits. This is also graphically depicted in Figure 1.2. This is the reason why gyrokinetic codes can only simulate the region of the plasma up to the magnetic presheath entrance; the plasma state at the magnetic presheath entrance needs to be provided as boundary conditions. The Debye sheath is characterised by an electric field that is much stronger than the magnetic field: $|\mathbf{v} \times \mathbf{B}| \ll |\mathbf{E}|$. This means that the gyro-orbit is lost.

An application of the numerical method described in this report will be generating boundary conditions for gyrokinetic codes. For the boundary conditions, only a steady-state solution of the magnetised sheath is needed. This is because a gyrokinetic code simulates time scales much larger than the ion gyro-period. But the magnetised sheath equilibrates in a few gyro-periods because that is the characteristic time for an ion to cross the magnetised sheath.

2.4 Kinetic theory

This section was based on the books [26, 27, 28, 29]. The latter introduces kinetic theory from the basics of classical mechanics. In this report, kinetic theory is used to solve for the magnetised sheath system, and thus a small introduction to kinetic theory will be given.

In kinetic theory, plasmas are described using distribution functions for a species s (f_s) in phase space. Usually, this phase space is six dimensional with three velocity and three positional coordinates. The time evolution of this distribution function is then given by

$$\frac{df_s}{dt} = \frac{\partial f_s}{\partial t} + \nabla \cdot (\mathbf{v} f_s) + \nabla_{\mathbf{v}} \cdot (\mathbf{a} f_s), \quad (2.19)$$

where \mathbf{v} is the velocity, \mathbf{a} is the acceleration and $\nabla_{\mathbf{v}} f$ is the gradient operator with respect to the velocity coordinates i.e. $\partial f / \partial v_i$. It is possible to prove Equation 2.19 by taking a phase space volume and calculating the flux of f through the boundary of the volume. After using the Gauss theorem one obtains the desired equation. In plasma physics $\mathbf{a} = e/m_s (\mathbf{E}(x) + \mathbf{v} \times \mathbf{B})$ is given by the Lorentz force. Note that in this case $\nabla_{\mathbf{v}} \cdot \mathbf{a} = 0$, and note that also $\nabla \cdot \mathbf{v} = 0$ since \mathbf{v} is a phase space coordinate just like \mathbf{x} , and thus independent of \mathbf{x} . This simplifies Equation 2.19 to:

$$\frac{df_s}{dt} = \frac{\partial f_s}{\partial t} + \mathbf{v} \cdot \nabla f_s + \mathbf{a} \cdot \nabla_{\mathbf{v}} f_s. \quad (2.20)$$

If there are no sources or sinks present, the distribution function is conserved, meaning:

$$\frac{\partial f_s}{\partial t} + \mathbf{v} \cdot \nabla f_s + \mathbf{a} \cdot \nabla_{\mathbf{v}} f_s = 0. \quad (2.21)$$

Note the distribution function is conserved along particle trajectories. This is an important notion that will be used throughout the report.

The moments of the distribution function contain collective information about the system, such as:

$$\begin{aligned} \mathcal{N}_s &= \int d\mathbf{v} \int d\mathbf{x} f_s \\ n_s(\mathbf{x}, t) &= \int f_s(\mathbf{x}, \mathbf{v}, t) d\mathbf{v} \\ \mathbf{\Gamma}_s(\mathbf{x}, t) &= \int \mathbf{v} f_s(\mathbf{x}, \mathbf{v}, t) d\mathbf{v}, \end{aligned} \quad (2.22)$$

where \mathcal{N}_s denotes the number of particles, n_s is the particle density and $\mathbf{\Gamma}_s(\mathbf{x}, t) = n_s \mathbf{u}_s(\mathbf{x}, t)$ is the particle flux with \mathbf{u}_s the flow velocity of a specific species. This means that one can go from a kinetic model to a fluid model by taking moments of the distribution function. Note that in general, by taking moments of the distribution function, physical information is lost (unless one takes an infinite number of moments), but it does make the physics that is being described more tangible.

2.5 The Debye sheath

The Debye sheath is the positively charged region close to the wall. The characteristic length scale of the Debye sheath is λ_D . In this section, the Debye sheath will be discussed as a separate region, where scale separation is used. This section will first go through the fluid treatment of the Debye sheath and then go through the kinetic treatment.

2.5.1 Fluid treatment

When a plasma comes into contact with a wall, a boundary layer will form called the Debye sheath. The Debye sheath is only a few Debye Lengths (λ_D) thick: in general this thickness is very small compared with the size of the plasma (L). As discussed in Section 2.3 there is a clear distinction between the Debye sheath and the rest of the plasma, they are described by different equations because they describe different length scales. The important difference is that the rest of the plasma is quasi-neutral while the Debye sheath is not. The Debye sheath has a net charge and thus an electric field. It arises because of the higher mobility of the electrons relative to the ions. If the electron and ion temperature are about equal, there will be about 63 electrons hitting the wall for every ion hitting the wall. This means that a negative charge will build up at the wall, and eventually ions will be accelerated towards the wall, and electrons will be repelled until a steady state is reached.

If one looks at the plasma as a fluid one can already obtain useful results about the plasma, namely the Bohm condition. For a derivation see [9]. In that paper the author obtains that a monotonic potential profile can only exist if the following condition is met:

$$u_\infty \geq v_B, \quad (2.23)$$

where u_∞ is the ion flow velocity at the sheath entrance in the direction perpendicular to the wall, and v_B is the Bohm velocity defined as

$$v_B = \sqrt{\frac{T_e}{m_i}}. \quad (2.24)$$

Equation 2.23 emphasises the existence of a presheath, in which the ions are accelerated to the Bohm velocity. On the scale of the presheath, this acceleration goes accompanied by a singularity in the electric field [9]. This is reminiscent of breaking the sound barrier in hydrodynamic theory. In this case, the "sound" velocity is the velocity of the ion acoustic waves [30] which is the same as the Bohm velocity. This means the that sheath entrance is defined on the presheath scale as the singularity, which indicates the breaking of the ion acoustic sound barrier [31, 32]. Another interesting analogue can be made between a plasma hitting a wall and a fluid expanding into a vacuum. A fluid expanding into a vacuum will reach the sound speed at the vacuum fluid boundary [33]. This is because the vacuum is a perfect sink

for fluids. Similarly, for plasmas, the perfect sink is the wall; the ions and electrons recombine, and the plasma state disappears. Note that this singularity is a trait of the asymptotic theory and is not physical. It happens precisely because a scale separation was assumed. If one considers the Debye sheath and the presheath as a whole, there won't be any singularities in the fields, nor will there be a clear definition of the Debye sheath entrance.

2.5.2 Kinetic treatment

It is also possible to look at the sheath kinetically. This part will go through the basic theory also discussed in [9] and [34], but with the simplification of collisionless plasmas⁴. To solve for the potential inside the sheath again, Poisson's equation has to be solved. The difference now is that the density has to be described using kinetic theory and thus distribution functions as in Equation 2.22. This means that Poisson's equation can be written as:

$$\epsilon_0 \nabla^2 \phi = -e \left(\sum_s Z_s \int f_s(\mathbf{x}, \mathbf{v}, t) d\mathbf{v} - \int f_e(\mathbf{x}, \mathbf{v}, t) d\mathbf{v} \right) \quad (2.25)$$

Where \sum_s indicates a sum over all the different ion species with different charges Z_s and different distribution functions f_s . The plasma sheath can be treated to be 1D. This is because smooth non-curved walls are considered. In the case that curved geometries and surface roughness are considered the problem cannot be treated as 1D. In the 1D case, the particles just move perpendicular towards (or away from) the wall, and there is complete symmetry along the wall. Thus only the axis that is perpendicular to the wall matters, this axis is called x , and the velocity in that direction is called v . Furthermore, the simplification of only one ion species is made with a charge Z . This means that the Laplacian in Equation 2.25 is just a second derivative with respect to x .

This equation can be solved under the assumption that the electrons entering the Debye sheath follow a Maxwellian distribution⁵. Some electrons will be repelled, and thus there are electrons with a small positive velocity in the sheath, which is not the case for the ions that will be accelerated. Using that the sheath entrance has to be quasi-neutral, one can obtain a solvability condition for Equation 2.25:

$$\frac{v_B^2}{n_e} \int_0^\infty \frac{f_i(v_{x,i}(\infty))}{v_{x,i}^2(\infty)} dv_{x,i} \leq 1, \quad (2.26)$$

which is known as the kinetic Bohm condition. Note the similarity between the result obtained by the fluid theory, which was the solvability condition of Equation 2.23. This solvability condition again shows the existence of the presheath in which the ions are accelerated to Bohm's velocity. It is linked to a divergence in the electric field of the sheath entrance on the presheath scale [9]. An important observation is that the Bohm condition only appears because a scale separation was assumed. Physically there is no clear definition of a sheath entrance and also not a solvability condition like the Bohm condition for the plasma boundary layer.

2.6 The magnetised sheath

In this section, the magnetised sheath, which is a combination of the magnetic presheath and the Debye sheath, is discussed. The latter was discussed in Section 2.5 by looking at it as a scale separated region. The magnetised sheath can be studied in two ways, either by looking at the Debye sheath and the magnetic presheath as one region or by looking at the Debye sheath as a single scale separated region and the magnetic presheath as a single scale separated region. This section will mainly focus on the magnetic presheath as the Debye sheath is already discussed. Only Section 2.6.2.1 will give a general description of both regions as one. The results of the numerical method in this report will discuss also the magnetised sheath as a whole as well as only the magnetic presheath.

2.6.1 Fluid treatment

This approach considers the plasma in the magnetic presheath as a fluid. This analysis follows the work by Riemann [35]. The geometry assumed here is the one that is also depicted in Figure 1.2. Thus the magnetic field makes an angle α with the wall, and the distance to the wall is x .

⁴In the Debye sheath this is a valid assumption because the length scale of the Debye sheath is usually much smaller than the mean free path of the particles.

⁵Just like the assumption of adiabatic electrons this assumption is valid when most electrons are repelled.

The magnetic presheath is described by the ion fluid equations, the Navier Stokes equations, and the mass conservation law:

$$\nabla \cdot (n_i \mathbf{v}) = 0 \quad (2.27)$$

$$m_i \mathbf{v} \cdot \nabla \mathbf{v} = e (\mathbf{E} + \mathbf{v} \times \mathbf{B}). \quad (2.28)$$

Here \mathbf{v} is the average ion flow velocity, $\mathbf{E} = -\nabla\phi = -\frac{d\phi}{dx}\mathbf{e}_x$ is the electric field given an electric potential ϕ , \mathbf{B} is the magnetic field. In Equation 2.28 it was assumed that $T_i \ll T_e$, this is known as the cold ion limit. Note also that Equation 2.28 is the steady state Navier Stokes equation with electro-magnetic force.

In the magnetic presheath quasi-neutrality is satisfied, which can be derived by taking $l = \rho_i$ in the analysis done in Section 2.2. Furthermore, adiabatic electrons are assumed, which is a valid assumption because most electrons are reflected away from the target, and they achieve thermal equilibrium. This gives then that the ion density is given by:

$$n_i = n_e = n_0 e^{\frac{e\phi}{T_e}}. \quad (2.29)$$

Here n_0 is the density at the entrance of the Debye sheath where it is set that $\phi = 0$; this is not done in the later sections of this report, but it simplifies the analysis of the fluid model. It is possible to obtain from Equations 2.27-2.29 the following:

$$v_x \frac{dv_z}{dx} = \Omega v_y \sin(\alpha), \quad (2.30)$$

$$v_x \frac{dv_y}{dx} = -\Omega v_x \cos(\alpha) - \Omega v_x \sin(\alpha), \quad (2.31)$$

$$\left(v_x - \frac{c_s^2}{v_x} \right) \frac{dv_x}{dx} = \Omega v_y \cos(\alpha). \quad (2.32)$$

Here c_s is given by $c_s = \left[\frac{T_e}{m_i} \right]^{1/2}$, and the $\mathbf{v} \times \mathbf{B}$ force was calculated using that $\mathbf{B} = -B \sin(\alpha) \mathbf{e}_x + B \cos(\alpha) \mathbf{e}_z$. Note also that $\Omega = \frac{eB}{m_i}$. There is an obvious singularity in these equations at $|v_x| = c_s$. This singularity indicates the entrance of the Debye sheath. This means that the ion current to the wall is given by $n_0 c_s$. The flux is conserved so $n_i v_x = n_0 c_s$, combined with Equation 2.29 it gives that ϕ is related to the flow by:

$$\phi = -\frac{T_e}{e} \log \left| \frac{v_x}{c_s} \right|. \quad (2.33)$$

Inside the plasma $|v_x| < c_s$, which means that the potential is positive inside the plasma and 0 at $x = 0$. But importantly, the potential is monotonic and thus $E > 0 \forall x$.

With this it is possible to derive the Chodura condition at the entrance of the magnetic presheath (see [35] for the derivation). The Chodura condition is

$$u_{\parallel,\infty} \geq v_B^2, \quad (2.34)$$

where $u_{\parallel,\infty}$ is the flow velocity of the plasma parallel to the magnetic field, and v_B is again the Bohm velocity as defined in Equation 2.24.

It is important to reiterate the two results obtained here in combination with the results from the fluid theory of the Debye sheath in the previous section. A plasma entering the Debye sheath needs to have a (super)sonic flow speed perpendicular to the wall. This is paired with a divergence in $\frac{dv_x}{dx}$ on the magnetic presheath scale. This in turn leads to a divergence in $\frac{d\phi}{dx}$ or in the force at $x = 0$. This divergence is integrable, however, because otherwise, energy wouldn't be conserved. Furthermore, the particle has to enter the magnetic presheath with a (super)sonic flow parallel to the magnetic field line.

2.6.2 Kinetic treatment

After considering the fluid description, this section will describe the kinetic theory. The kinetic theory is more general, and thus results from the kinetic theory are more valuable. The fluid description is expected to break down in the magnetised sheath because the distribution functions will not be Maxwellian anymore.

2.6.2.1 Mathematical description of the magnetised sheath

To solve for the magnetised sheath kinetically one has to solve the Vlasov equation combined with the ion orbits. In general, the Vlasov equation for species s can be written as:

$$\frac{\partial f_s}{\partial t} + \mathbf{v} \cdot \nabla f_s + \dot{\mathbf{v}} \cdot \nabla_v f = 0. \quad (2.35)$$

The magnetic field is given by:

$$\mathbf{B} = B \cos(\alpha) \mathbf{e}_z - B \sin(\alpha) \mathbf{e}_x, \quad (2.36)$$

where \mathbf{e}_z is the unit vector in the direction parallel to the wall for coordinate z and \mathbf{e}_x is the unit vector pointing towards the wall for coordinate x . When there is a magnetic field, particles make a gyrating motion around the magnetic field line. The frequency of this motion is given by the gyrofrequency:

$$\Omega_s = \frac{Z_s e B}{m_s}. \quad (2.37)$$

The thermal gyroradius is the typical radius of an ion gyro-orbit and is defined by:

$$\rho_{t,s} = \frac{v_{t,s}}{\Omega}, \quad (2.38)$$

The geometry assumed in this report is the one in Figure 1.2. As stated before, this means that there is a symmetry in the z and y coordinate. The electric field has only an x component i.e. $\mathbf{E} = -\frac{d\phi}{dx} \mathbf{e}_x$, and the magnetic field is defined in the x, z plane i.e. $\mathbf{B} = \mathbf{B} = -B \sin(\alpha) \mathbf{e}_x + B \cos(\alpha) \mathbf{e}_z$. This makes the problem effectively a 1D 3V problem. Only one spatial dimension is of interest, the x direction, but 3 velocity directions are important because they are all interlinked via the equations. The electrons are assumed to follow a Boltzmann distribution:

$$n_e = n_\infty e^{\frac{e\phi}{T_e}}. \quad (2.39)$$

With n_∞ the density at the entrance of the magnetic presheath.

The equations of motion for an ion moving through this magnetised sheath system are given by:

$$\begin{aligned} \dot{x} &= v_x \\ \dot{v}_x &= -\frac{\Omega}{B} \frac{d\phi}{dx} + \Omega v_y \cos(\alpha) \\ \dot{v}_y &= -\Omega v_x \cos(\alpha) - \Omega v_z \sin(\alpha) \\ \dot{v}_z &= \Omega v_y \sin(\alpha). \end{aligned} \quad (2.40)$$

Note the similarities between Equations 2.30, 2.31, 2.32 and Equation 2.40, the forces felt by the fluid and the particles are exactly the same. In this report, the steady state solution of the system is of interest; this means that Equation 2.35 for the ions simplifies to:

$$v_x \frac{df_i}{dx} + \dot{\mathbf{v}} \cdot \nabla_v f_i = 0. \quad (2.41)$$

Equation 2.40 gives the value of $\dot{\mathbf{v}}$. There are two unknowns in this system, the distribution function $f(x, \mathbf{v})$ and the potential $\phi(x)$. In the steady-state problem the potential $\phi(x)$ determines the correct solution for $f(x, \mathbf{v})$ from the boundary condition at the magnetic presheath entrance $f_\infty(\mathbf{v}_\infty)$ via the equations of motion. The physical solution of ϕ has to also satisfy Poisson's equation:

$$\epsilon_0 \frac{d^2 \phi}{dx^2} = e(Zn_i - n_e), \quad (2.42)$$

where the electron density follows a Boltzmann distribution Equation 2.39 and the ion density is given by its distribution function $f_i(x, \mathbf{v})$:

$$n_i(x) = \int f_i(x, \mathbf{v}) d^3 \mathbf{v}. \quad (2.43)$$

So Equation 2.41 and Equation 2.42 together with Equation 2.40 for the trajectories give the mathematical description of the magnetised sheath.

2.6.2.2 Particle trajectories in magnetic presheath

This Section will be heavily based on [7, 13, 14], so the interested reader is referred to those works.

To make analytical progress Geraldini et al. made use of the scale separation, which was explained in Section 2.3. Using the scales of the magnetic presheath, it turns out that Equation 2.42 simplifies to the quasi-neutrality equation because the length scale of the magnetic presheath is $\rho_i \gg \lambda_D$. Then to make more analytical progress, Geraldini et al. assumed a shallow angle of the magnetic field with the wall i.e. $\alpha \ll 1$. For fusion, this is most often a valid assumption because a small angle α minimises the heat load on the target [36]. For the limiting case setting $\alpha = 0$ in Equation 2.40 will change the last three equations to:

$$\dot{v}_x = -\frac{\Omega}{B} \frac{d\phi}{dx} + \Omega v_y, \quad (2.44)$$

$$\dot{v}_y = -\Omega v_x, \quad (2.45)$$

$$\dot{v}_z = 0. \quad (2.46)$$

Using $\dot{x} = v_x$ and Equation 2.45 one obtains:

$$\bar{x} = \frac{v_y}{\Omega} + x. \quad (2.47)$$

Here \bar{x} is a constant of integration, and it gives a representation of the x position of the ion orbit. The perpendicular energy of a particle moving with $\alpha = 0$ is defined by its perpendicular kinetic energy added to its potential energy:

$$U_{\perp} = \frac{1}{2} v_x^2 + \frac{1}{2} v_y^2 + \frac{\Omega \phi}{B}. \quad (2.48)$$

Then $\dot{U}_{\perp} = v_x \dot{v}_x + v_y \dot{v}_y + \frac{d\phi}{dt} \frac{\Omega}{B}$, note that here $\frac{d\phi}{dt}$ is the change of potential a particle feels while moving through the system i.e. it is the total derivative: $\frac{d\phi}{dt} = \frac{\partial \phi}{\partial t} + \mathbf{v} \cdot \nabla \phi = v_x \frac{d\phi}{dx}$. It is clear that adding Equation 2.44 multiplied by v_x to Equation 2.45 multiplied by v_y results in a proof that $\dot{U}_{\perp} = 0$. Furthermore v_z is a constant of motion, thus there are three constants of motion in the case that $\alpha = 0$. \bar{x} , U_{\perp} and the total energy U . In the case that $\alpha \ll 1$ they change slowly over time except for U which is, of course, still conserved. With these three approximately conserved quantities one can obtain the three velocity components. Using Equation 2.47 and Equation 2.48 one obtains for v_x :

$$v_x = \sigma_x V_x(x, \bar{x}, U_{\perp}) \quad \text{with} \quad V_x(x, \bar{x}, U_{\perp}) = \sqrt{2(U_{\perp} - \chi(x, \bar{x}))}. \quad (2.49)$$

Where $\sigma_x = \pm 1$ to account for the positive and negative branches of v_x . Here $\chi(x, \bar{x}, U_{\perp})$ is the so called effective potential. This effective potential is given by:

$$\chi(x, \bar{x}) = \frac{1}{2} \Omega^2 (x - \bar{x})^2 + \frac{\Omega \phi(x)}{B} \quad (2.50)$$

Similarly for v_y and v_z one will find respectively:

$$v_y = \Omega(x - \bar{x}) \quad (2.51)$$

$$v_z = \sigma_{\parallel} V_{\parallel}(U_{\perp}, U) \quad \text{with} \quad V_{\parallel}(U_{\perp}, U) = \sqrt{2(U - U_{\perp})}. \quad (2.52)$$

The effective potential in Equation 2.50 is an important quantity, and it pays off to look a bit more into the different effective potential curves are possible. The different curves also give rise to different types of particle trajectories.

First it must be noted that $v_x \in \mathbb{R}$, which means that $U_{\perp} \geq \chi(x, \bar{x})$ follows from Equation 2.49. This means that particles can get trapped in the effective potential curve. If for some x it holds that $\chi(x) > U_{\perp}$ then the particle cannot reach that position x . In general, a particle will get trapped around two locations x_b (bottom) and x_t (top) such that $x_t > x_b$ and $\chi(x_b) = \chi(x_t) = U_{\perp}$. Then there will also be a minimum in the effective potential curve x_m such that $x_t \leq x_m \leq x_b$. These situations are depicted in Figure 2.2. For an effective potential that has a minimum at x_m , there are two possible types of effective potential.

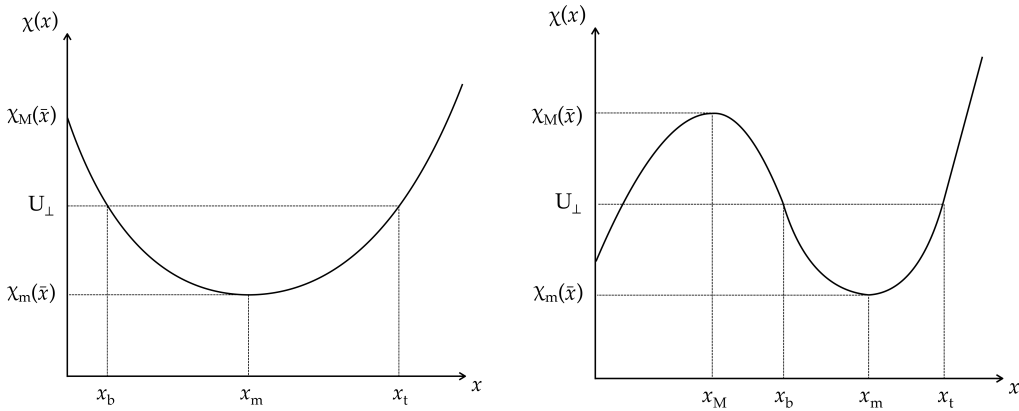


Figure 2.2: The two different types of effective potential curves, type I on the left and type II on the right. Both have a stationary point at $x = x_m$. Additionally the type II curve is characterised by a second stationary point $x = x_M$ corresponding to a maximum. Both types allow closed orbits for any value of U_\perp in the range $\chi_m \leq U_\perp \leq \chi_M$ with bottom and top bouncepoints given by x_b and x_t respectively. Figure retrieved from Geraldini [7]

- a type I effective potential has only one stationary point corresponding to a minimum. There will be a local maximum at $x = 0$, which is not a stationary point.
- a type II effective potential has two stationary points: one corresponding to a minimum x_m and the other corresponding to a maximum x_M .

These different types of effective potentials also give rise to different types of curves. The type II potential gives rise to the more interesting trajectories. Two of these are displayed in Figure 2.3. This figure describes the non-trivial trajectories that one has to deal with in the magnetised sheath problem. Note especially that particles in a type II potential always will have a point x_M where the magnetic force and electric force in the x direction are exactly equal and opposite. If at that point the particle also has $v_x = 0$, the particle will have a trajectory like the one on the left in Figure 2.3. At this point, \ddot{v}_x will determine if a particle will have a turning point or not. This usually results in a particle trajectory where the particle will move tangentially to the wall for a long time.

There is a distinction, which is useful to make, between open orbits and closed orbits. Closed orbits are orbits for which there will be still a turning/bounce point in future times. Open orbits will not have any bounce points in future times. Ion trajectories approaching the wall can be either an open orbit without bounce points or a successive combination of closed orbits until the orbit becomes open close to the wall. When α becomes smaller, the closed orbit particle density becomes bigger compared with the open orbit particle density. Getting closer to the wall naturally increases the open orbit particle density. It can be useful to express both types of particles in different distribution functions with $f_{op}(x, v_x, v_y, v_z)$ the open orbit distribution function (*op* for open) and $f_{cl}(x, v_x, v_y, v_z)$ the closed orbit distribution function (*cl* for closed).

2.6.2.3 Analytical results on distribution function

With the small-angle approximation of the magnetic presheath, it is possible to do more analytic derivations. Only the important results will be highlighted here; for more detailed information on the derivation the reader is referred to Geraldini et al. [13, 14]. Geraldini exploits the method of characteristics on the open and closed ion distribution functions. This method, in the small α approximation, works well because there is an adiabatic invariant $\mu = \frac{1}{\pi} \int_{x_b}^{x_t} V_x(x, \bar{x}, U_\perp) dx$ that is conserved to lowest order. In the equation for μ , x_b and x_t denote the top and bottom bounce point as in Figure 2.2. Then quasi neutrality is imposed combined with Boltzmann electrons. The analysis then proceeds by looking at an asymptotic expansion of the quasi neutrality equation near the magnetic presheath entrance $\frac{x}{\rho_i} \rightarrow \infty$. Furthermore, $n_{i,op}$ can be assumed to be zero compared with the closed orbit density at the magnetic presheath entrance. This is because at the magnetic presheath entrance most orbits will be closed for small α . Note that this is not true for general values of α ; this will become clear in Section 3.4. Expanding both the adiabatic electron density and the closed orbit ion density around $\frac{x}{\rho_i} \rightarrow \infty$ leads

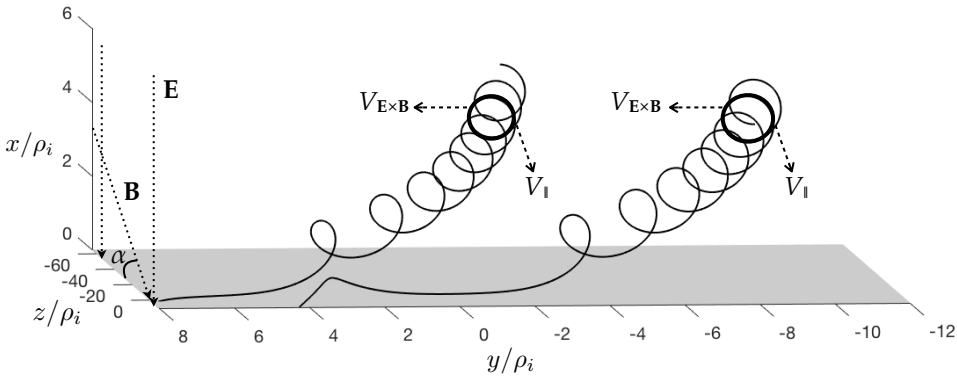


Figure 2.3: Two different ion trajectories, for different values of gyrophase angle θ when entering the magnetic presheath. The wall is indicated by the shaded plane. The electric and magnetic fields are indicated with the dotted black lines, $\alpha = 0.05$ radians. Note that most of the trajectory is represented by superimposed rings in this figure. As can be seen the ions stream along the magnetic field line with velocity V_{\parallel} . When the ions approach the wall, they will feel the strong electric field, and they will stream with a drift velocity in the $\mathbf{E} \times \mathbf{B}$ (y) direction with speed $V_{\mathbf{E} \times \mathbf{B}}$. Since these are type II orbits, there is a point (x_M) in which the electric and magnetic forces on the ion are equal and opposite, where the trajectories spend a long time moving almost tangential to the wall. The trajectory on the left crosses x_M with near-zero v_x , while the trajectory on the right crosses x_M with the largest velocity possible. Note that the trajectory on the left spends an extremely long time moving parallel to the wall in the y direction. Figure retrieved from Geraldini [7]

to an expression that can be analysed further. By carefully setting all the orders in the resulted equation equal Geraldini obtains the kinetic version of Chodura's condition at the magnetic presheath (see Equation 2.34 for the fluid version):

$$Zv_B^2 \int \frac{f_\infty(\mathbf{v})}{v_z^2} d^3\mathbf{v} \leq n_{e,\infty}. \quad (2.53)$$

Note that for the small angle approximation $\alpha \ll 1$, v_z is approximately the particle velocity along the magnetic field. Further, a functional dependency of the potential close to the magnetic presheath entrance is found; in particular it is found that $\phi(x) \sim \frac{1}{x^2}$.

Next, an asymptotic expansion of the quasi-neutrality equation is done around $x = 0$. In this case $n_{i,cl} \neq 0$ close to $x = 0$, but $n_{i,cl}(0) = 0$, because if particles have hit the wall they were by definition not closed. Again carefully looking at the terms in the expansion and setting them equal, two main results are obtained. One is that for quasi-neutrality to hold, the kinetic Bohm condition should be marginally satisfied when the plasma reaches $x = 0$ i.e.:

$$Zv_B^2 \int \frac{f_0(\mathbf{v})}{v_x^2} d^3\mathbf{v} = n_{e,0}. \quad (2.54)$$

As can be seen, this is identical to marginally satisfying Equation 2.26. Satisfying the Bohm condition is paired with a divergence in the electric field; in particular, Geraldini finds that:

$$\delta\phi(x) = \phi(x) - \phi(0) \sim x^{\frac{1}{2}}. \quad (2.55)$$

This, in turn, means that the electric field and thus the force a particle feels close to the wall diverges with $\frac{1}{\sqrt{x}}$.

Note that Equation 2.54 and Equation 2.55 were derived assuming small α . In this report both conditions will be proven for general angle α .

3 Methods

In this Section, the novel numerical algorithm is explained. This is done by looking at the analytical description of the magnetic presheath (Section 3.1), showing how an ion density is found that satisfies the Vlasov equation given a potential (Section 3.2). It turns out that particles need to be integrated forwards in time. How this is done is told in Section 3.3. There will be some constraints on the velocity sampling; not all particles will hit the wall, and there will be singularities in the single particle density contributions. Section 3.4 will explain this. With the ion density that satisfies the Vlasov equation, one still needs to obtain an electrostatic potential that is self-consistent i.e. solves Poisson's equation. The iterative procedure for this will be discussed in Section 3.5. That section will be split up into a part that will look at the magnetic presheath and a part that will look at the entire magnetised sheath. The magnetic presheath is characterised by an nonphysical divergence in the electric field at $x = 0$. Dealing with this divergence means that the grid has to be defined carefully. The grid definition is shown in Section 3.6. The numerical method is optimised as much as possible with respect to a low computational time. How this is done is analysed in Section 3.7.

3.1 Analytical description of the magnetic presheath

The coordinate system in Figure 1.2 is used. Hence the sheath region is assumed to be symmetric in z and y . The system needs to be solved kinetically, and only a steady state solution is needed. This means that the Vlasov Equation 2.21 can be simplified to:

$$v_{x,i} \frac{\partial f_i}{\partial x} + \dot{\mathbf{v}}_i \cdot \nabla_v f_i = 0. \quad (3.1)$$

In this equation $\dot{\mathbf{v}}_i$ is given by the equations of motion for the ion, meaning that in general $\dot{\mathbf{v}}_i = \frac{\mathbf{F}_i}{m_i}$. In the magnetic presheath there is an electric field and a magnetic field: $\mathbf{F}_i = -e \frac{d\phi}{dx} \mathbf{e}_x + e \mathbf{v}_i \times \mathbf{B}$. The Vlasov equation for this system is thus given by:

$$v_{x,i} \frac{\partial f_i}{\partial x} + \frac{-e \frac{d\phi}{dx} \mathbf{e}_x + e \mathbf{v}_i \times \mathbf{B}}{m_i} \cdot \nabla_v f_i = 0. \quad (3.2)$$

The other equation that describes the system is Poisson's equation given by Equation 2.42. It makes sense to normalise these equations with respect to the magnetic presheath length scales. The length scale of the magnetic presheath is the ion Larmor radius (ρ_i). Furthermore, the magnetic presheath is characterised by the fact that the magnetic force is comparable to the electric force on the particle and thus $v_{th,i} B \sim \frac{d\phi}{dx} \sim \frac{T_e}{e\rho_i}$. Here B is the magnitude of the magnetic field, and $v_{th,i}$ the thermal velocities of the ions: the characteristic velocity of the ions. With these characterised sizes normalised variables are defined:

$$\hat{\mathbf{v}} = \frac{\mathbf{v}}{v_{th,i}}, \quad \hat{\phi} = \frac{e\phi}{T_e}, \quad \hat{n}_s = \frac{n_s}{n_{e,\infty}}, \quad \hat{x} = \frac{x}{\rho_i}, \quad \hat{\mathbf{B}} = \frac{e\rho_i v_{th,i} B}{T_e} \quad (3.3)$$

Where $n_\infty = n_{e,\infty} = Z n_{i,\infty}$ is the density at the sheath entrance for both electrons. In the normalised variables Equation 3.2 reduces to:

$$\hat{v}_{x,i} \frac{\partial f_i}{\partial \hat{x}} + \left(\frac{-d\hat{\phi}}{d\hat{x}} \mathbf{e}_x + \hat{\mathbf{v}}_i \times \hat{\mathbf{B}} \right) \cdot \frac{\partial f_i}{\partial \hat{\mathbf{v}}} = 0 \quad (3.4)$$

Poisson's equation reduces to:

$$\frac{\epsilon_0 T_e}{e^2 n_\infty \rho_i^2} \frac{d^2 \hat{\phi}}{d\hat{x}^2} = \hat{n}_e - \hat{n}_i. \quad (3.5)$$

Note that $\lambda_D = \sqrt{\frac{\epsilon_0 T_e}{e^2 n_\infty}}$. So the factor in front can be written as $\frac{\lambda_D^2}{\rho_i^2} \ll 1$. Thus the entire left hand side of Equation 3.5 can be ignored in the magnetic presheath. This gives that the magnetic presheath is, in fact, quasi-neutral i.e. $\hat{n}_i = \hat{n}_e$. To avoid confusion later when discretising the equations the normalised potential will not be denoted with a hat. It will always be explicitly stated if the variable is normalised.

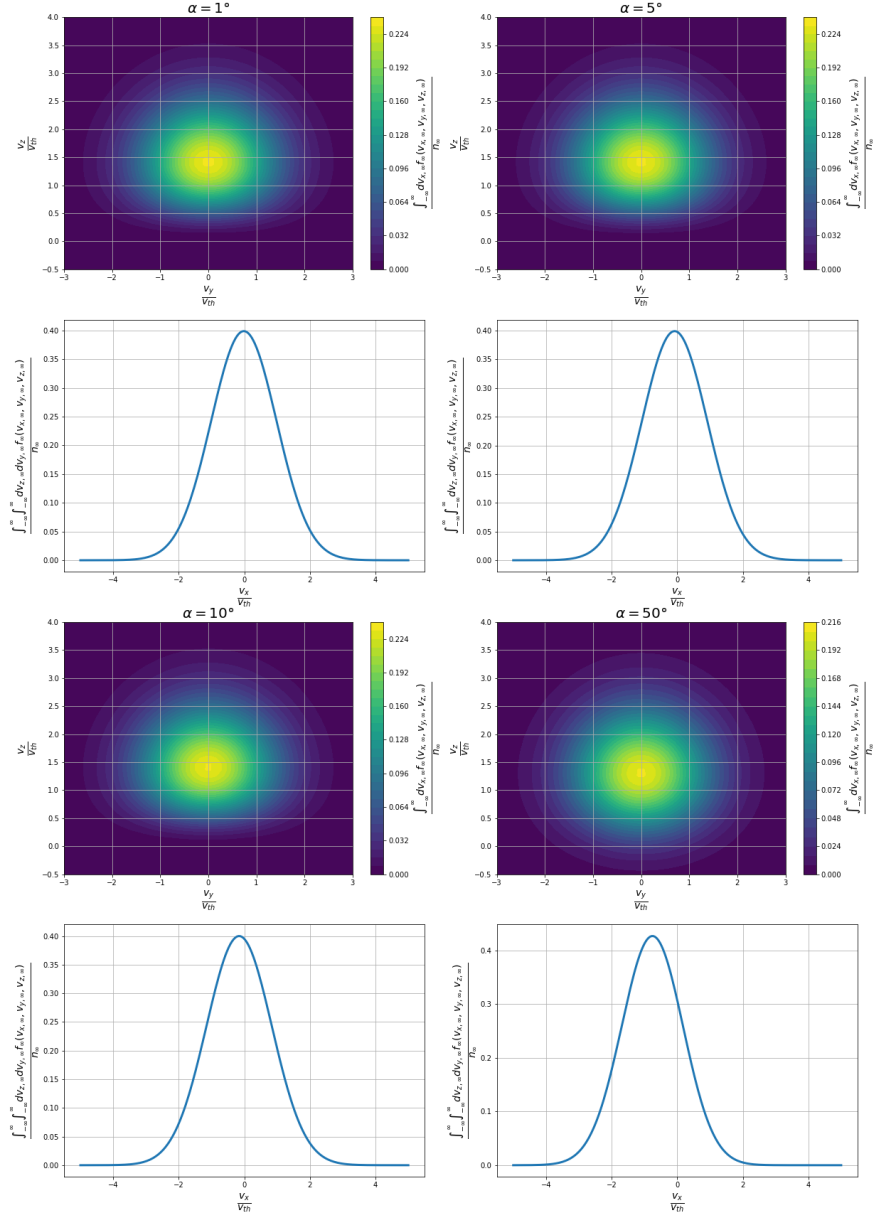


Figure 3.1: Graphical depiction of the incoming ion distribution function for different angles α

Hence the magnetic presheath is described by Equation 3.4 and the quasi-neutrality equation. There will be boundary conditions on the ion distribution function. First of all, an absorbing wall is assumed meaning: $f_i(0, \mathbf{v}) = 0$ if $v_x > 0$. At the sheath entrance, a boundary condition is imposed: it is assumed that there are no ions that are being reflected out of the magnetic presheath. This is a valid assumption for the ions as the electric field accelerates them towards the wall, and thus once they enter the sheath with a parallel velocity directed towards the wall, they will hit the wall. This means that $f_i(\infty, \mathbf{v}) = 0$ if $v_{\parallel} < 0$. Here v_{\parallel} is the velocity parallel to the magnetic field line. Furthermore, the distribution function of the ions is assumed to be a modified Maxwellian for the incoming ions: $f_i(\infty, \mathbf{v}) = f_{i,\infty}(\mathbf{v}_{\infty})$ for $v_{\parallel} > 0$. The distribution function is chosen such that Chodura's condition at the sheath entrance is satisfied (Equation 2.34). In particular the distribution function is given by:

$$f_{\infty}(v_{x,\infty}, v_{y,\infty}, v_{z,\infty}) = \begin{cases} 0 & \text{for } v_{\parallel} \leq 0 \\ \frac{4}{\pi^{\frac{3}{2}}} \left(\frac{m_i}{2T_e}\right)^{\frac{5}{2}} v_{\parallel}^2 \exp\left(-\frac{m_i}{2T_e} v^2\right) & \text{for } v_{\parallel} > 0. \end{cases} \quad (3.6)$$

For small angle, $\alpha \ll 1$, this reduces to the distribution function used by Geraldini in [7]. The distribution is shown in Figure 3.1. The final assumption is that electrons are adiabatic i.e. $n_e = n_{\infty} e^{\frac{e\phi}{T_e}}$. Note that

the incoming distribution function depends on the magnetic field angle α because v_{\parallel} is the velocity parallel to the magnetic field i.e. $v_{\parallel} = -v_x \sin(\alpha) + v_z \cos(\alpha)$.

First, the focus will be on calculating the ion density given a potential, which will be dealt with in the next section. In other words an ion density will be found that satisfies Equation 3.4 given a potential.

3.2 Calculating the ion density

To find a distribution function that solves Equation 3.4 it is convenient to use a Lagrangian (PIC) representation. To obtain this, one first uses the trivial relation:

$$\begin{aligned} f_i(x, \mathbf{v}) &= \int_{\mathbb{R}^3} d^3 \mathbf{v}' \int_0^\infty dx' f_i(x', \mathbf{v}') \delta(x - x') \delta(\mathbf{v} - \mathbf{v}') \\ &= \int_{\mathbb{R}^3} d^3 \mathbf{v}' \int_0^{\tau_i} dt v'_x(t) f_i(x'(t), \mathbf{v}'(t)) \delta(x - x'(t)) \delta(\mathbf{v} - \mathbf{v}'(t)). \end{aligned} \quad (3.7)$$

Here $dx' = v'_x dt$ was used, and τ_i is the transition time for ions of the magnetic presheath. Note that $f_i(x', \mathbf{v}')$ that solves Equation 3.4 is unknown. But the boundary conditions are known. This means that it is key to mold Equation 3.7 into a form that only depends on the incoming distribution function and incoming \mathbf{v} . For this a transformation of variables is done:

$$f_i(x, \mathbf{v}) = \int_{\mathbb{R}^3} d^3 \mathbf{v}_\infty v_{x,\infty} f_{i,\infty}(\mathbf{v}_\infty) \int_0^{\tau_i} dt \delta(x - x'(t, \mathbf{v}_\infty)) \delta(\mathbf{v} - \mathbf{v}'(t, \mathbf{v}_\infty)). \quad (3.8)$$

Here \mathbf{v}_∞ is the velocity at the sheath entrance. Note that the following relation was used: $v_x f(x, \mathbf{v}) d\mathbf{v} = v_{x,\infty} f_\infty(\mathbf{v}_\infty) d\mathbf{v}_\infty$. This relation is valid because phase space volume is conserved [29]. It is now possible to obtain $f(x, \mathbf{v})$ by integrating the particle trajectory over the ion transit time for all possible initial velocities \mathbf{v}_∞ at x_∞ . To calculate the ion density one has to integrate the ion distribution function over \mathbf{v} , thus:

$$\begin{aligned} n_i &= \int_{\mathbb{R}^3} d^3 \mathbf{v} f_i(x, \mathbf{v}) = \int_{\mathbb{R}^3} d^3 \mathbf{v} \int_{\mathbb{R}^3} d^3 \mathbf{v}_\infty v_{x,\infty} f_{i,\infty}(\mathbf{v}_\infty) \int_0^{\tau_i} dt \delta(x - x'(t, \mathbf{v}_\infty)) \delta(\mathbf{v} - \mathbf{v}'(t, \mathbf{v}_\infty)) \\ &= \int_{\mathbb{R}^3} d^3 \mathbf{v}_\infty v_{x,\infty} f_{i,\infty}(\mathbf{v}_\infty) \int_0^{\tau_i} dt \delta(x - x'(t, \mathbf{v}_\infty)). \end{aligned} \quad (3.9)$$

To compute this equation numerically, it is most convenient to write the ion density in terms of finite element basis functions ⁶:

$$n_i(x) = \sum_{\alpha} \hat{n}_i^{\alpha} \Lambda^{\alpha}(x), \quad (3.10)$$

where $\Lambda^{\alpha}(x)$ are the polynomial basis functions and \hat{n}_i^{α} the coefficients of the density. This is a way to discretise the ion density. It is possible to project Equation 3.9 onto finite elements, which makes it possible to solve it numerically. One obtains:

$$\int_{\mathbb{R}_{\geq 0}} dx \sum_{\alpha} \hat{n}_i^{\alpha} \Lambda^{\alpha}(x) \Lambda^{\beta}(x) = \int_{\mathbb{R}^3} d^3 \mathbf{v}_\infty v_{x,\infty} f_{i,\infty}(\mathbf{v}_\infty) \int_0^{\tau_i} dt \Lambda^{\beta}(x'(t, \mathbf{v}_\infty)). \quad (3.11)$$

Note that on the right hand side the term $\int_0^{\tau_i} dt \Lambda^{\beta}(x'(t, \mathbf{v}_\infty))$ is an integral in time over the particle trajectories $x'(t, \mathbf{v}_\infty)$, which is reminiscent of a Particle-in-cell (PIC) simulation. A PIC method samples particles according to the distribution function and then uses a Monte-Carlo integration to integrate over the particle trajectories at each time step. The advantage in this new approach is two-fold: first, it integrates the distribution function directly over velocity space and thus does not rely on sampling particles randomly according to the distribution function. Second, it integrates over time directly instead of using the Monte-Carlo approach. Note that both advantages exploit the fact that a steady state solution is sought directly without solving for the time evolution. The equation can be seen as a linear algebra equation where $r^{\beta} = \int_{\mathbb{R}^3} d^3 \mathbf{v}_\infty v_{x,\infty} f_{i,\infty}(\mathbf{v}_\infty) \int_0^{\tau_i} dt \Lambda^{\beta}(x'(t, \mathbf{v}_\infty))$ and $M^{\alpha\beta} = \int_{\mathbb{R}_{\geq 0}} dx \Lambda^{\alpha}(x) \Lambda^{\beta}(x)$. This means that Equation 3.11 can be written as:

$$M^{\alpha\beta} \hat{n}_i^{\alpha} = r^{\beta}, \quad (3.12)$$

⁶For more information on the finite element method see e.g. [37, 38, 39].

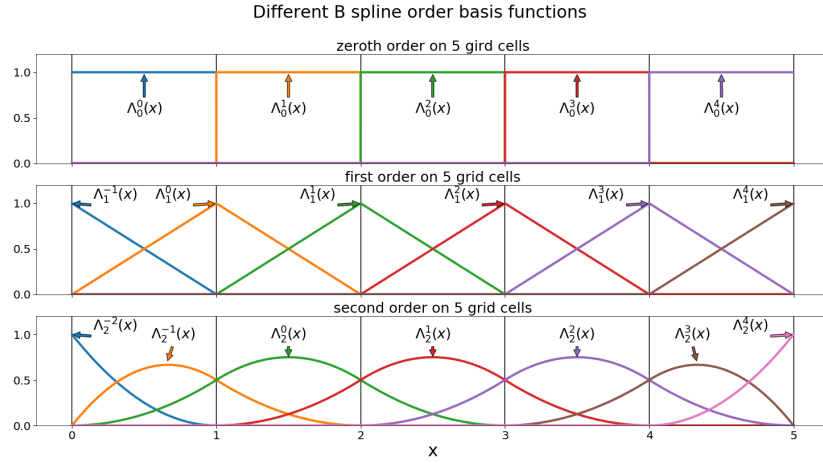


Figure 3.2: Different order basis functions defined on an equidistant grid are shown. The different basis functions have different colors. Note that the boundary basis functions are defined such that they are equal to one at the boundary of the interval.

where an implicit sum over repeated indices is assumed. The matrix $M^{\alpha\beta}$ is commonly referred to as the mass matrix. It is a symmetric band matrix where the number of diagonal bands is related to the order of the basis functions. Equation 3.12 forms the backbone of this numerical method as it gives a way to calculate the ion density by calculating the particle trajectories. In other words, it is possible to obtain the ion density for a given potential field. This means that the scheme can obtain an ion density such that the Vlasov equation (Equation 3.4) is satisfied, but it does not guarantee that the quasi-neutrality equation is satisfied. To this end, one can make use of an iterative scheme. This scheme updates the potential field until a self-consistent potential field is found i.e. an electrostatic potential that solves the Vlasov equation and the quasi-neutrality equation.

In this report either second-order or first-order polynomial basis functions are used. See Figure 3.2 for a reference of the different order basis functions up to second order. The basis functions that are used are B-spline basis functions that are defined in [39]. The zeroth-order basis functions are piece-wise constant. To define them start by defining the finite interval $[a, b]$ subdivided into N_x intervals:

$$a = x_0 \leq x_1 \leq \dots \leq x_{N_x} = b, \quad (3.13)$$

where x_i denotes the i^{th} grid point. The j^{th} basis function of order p is then defined as $\Lambda_p^j(x)$. The zeroth order basis functions are then defined as piece-wise constant:

$$\Lambda_0^i(x) = \begin{cases} 1 & \text{if } x_i \leq x < x_{i+1} \\ 0 & \text{otherwise.} \end{cases} \quad (3.14)$$

The linear basis function can be expressed in terms of the zeroth-order basis function:

$$\Lambda_1^i = \frac{x - x_i}{x_{i+1} - x_i} \Lambda_0^i + \frac{x_{i+2} - x}{x_{i+2} - x_{i+1}} \Lambda_0^{i+1}. \quad (3.15)$$

The quadratic basis functions can also be expressed in terms of the zeroth-order basis functions:

$$\begin{aligned} \Lambda_2^i &= \frac{(x - x_i)^2}{(x_{i+2} - x_i)(x_{i+1} - x_i)} \Lambda_0^i \\ &+ \left[\left(\frac{x - x_i}{x_{i+2} - x_i} \right) \left(1 - \frac{x - x_{i+1}}{x_{i+2} - x_{i+1}} \right) + \left(\frac{x - x_{i+1}}{x_{i+2} - x_{i+1}} \right) \left(1 - \frac{x - x_{i+1}}{x_{i+3} - x_{i+1}} \right) \right] \Lambda_0^{i+1} \\ &+ \left(1 - \frac{x - x_{i+1}}{x_{i+3} - x_{i+1}} \right) \left(1 - \frac{x - x_{i+2}}{x_{i+3} - x_{i+2}} \right) \Lambda_0^{i+2}. \end{aligned} \quad (3.16)$$

If there are N_x zeroth-order basis functions, then there are $N_x + p$ p^{th} order basis functions. Note that in both Equation 3.15 and Equation 3.16 the index i runs from respectively -1 and -2 to $N_x - 1$. Note

that this then leads to nodes x_i that are outside the domain. To deal with this, boundary conditions of the basis functions have to be properly defined.

To do this, the definition is chosen such that $\Lambda_p^{-p}(b) = 1$ and $\Lambda_p^{N_x-1}(a) = 1$, $p \in \{0, 1, 2\}$. This can be also clearly seen in Figure 3.2 (there $a = 0$ and $b = 5$). Then the boundary basis functions of both linear and quadratic order basis functions are defined by:

$$\begin{aligned}\Lambda_1^{-1} &= \frac{x_1 - x}{x_1 - x_0} \Lambda_0^0 \\ \Lambda_1^{N_x-1} &= \frac{x - x_{N_x-1}}{x_{N_x} - x_{N_x-1}} \Lambda_0^0 \\ \Lambda_2^{-2} &= \left(\frac{x_1 - x}{x_1 - x_0} \right)^2 \Lambda_0^0 \\ \Lambda_2^{N_x-1} &= \left(\frac{x - x_{N_x-1}}{x_{N_x} - x_{N_x-1}} \right)^2 \Lambda_0^0.\end{aligned}\tag{3.17}$$

Note that Λ_{-1}^2 and $\Lambda_{N_x-2}^2$ is not defined yet. Note that the sum of splines defined in a certain element always is equal to 1. Thus Λ_{-1}^2 and $\Lambda_{N_x-2}^2$ can be defined as respectively:

$$\begin{aligned}\Lambda_2^{-1} &= 1 - \Lambda_2^{-2} - \Lambda_2^0 \\ \Lambda_2^{N_x-2} &= 1 - \Lambda_2^{N_x-1} - \Lambda_2^{N_x-3}.\end{aligned}\tag{3.18}$$

The subscript p , to denote the order of the basis function, will be dropped in the future. If it is used it is explicitly stated.

3.3 Particle integration

As stated before the vector r^β in Equation 3.12 is calculated using a simulation that is reminiscent to a Particle-in-Cell simulation. This is because the particle trajectories are followed forward in time to obtain the contribution from each particle to the density. The global idea behind this is that the particles are injected with some entrance velocity \mathbf{v}_∞ . Not all particles with every possible velocity \mathbf{v}_∞ are going to hit the wall. To understand this, it makes sense to rewrite the equations of motion for the particles in terms of new coordinates, more specifically, a coordinate system that aligns with the magnetic field. This is done by a simple rotation of the coordinate system with a rotation matrix:

$$\begin{pmatrix} \cos(\alpha) & 0 & \sin(\alpha) \\ 0 & 1 & 0 \\ -\sin(\alpha) & 0 & \cos(\alpha) \end{pmatrix}.$$

This gives a new coordinate system (denoted by ') such that:

$$\begin{pmatrix} v'_x \\ v'_y \\ v'_z \end{pmatrix} = \begin{pmatrix} v_x \cos(\alpha) + v_z \sin(\alpha) \\ v_y \\ -v_x \sin(\alpha) + v_z \cos(\alpha) \end{pmatrix}.\tag{3.19}$$

As the magnetic field has components $\mathbf{B} = -\sin(\alpha)\mathbf{e}_x + \cos(\alpha)\mathbf{e}_z$, the velocity component v'_z will be aligned with the magnetic field, and thus v'_z will be denoted as v_\parallel . In these coordinates, the equations of motion assuming only an electric field in the x direction can be written as:

$$\begin{aligned}\dot{x} &= v'_x \cos(\alpha) - v_\parallel \sin(\alpha) \\ \dot{v}'_x &= -\frac{\Omega}{B} \frac{d\phi}{dx} \cos(\alpha) + \Omega v'_y \\ \dot{v}'_y &= -\Omega v'_x \\ \dot{v}_\parallel &= \frac{\Omega}{B} \frac{d\phi}{dx} \sin(\alpha).\end{aligned}\tag{3.20}$$

Note that from these equations, it is easy to see that the electric field only accelerates the particles towards the wall. If a particle will hit the wall without the electric field, it will definitely hit the wall with the electric field. At the sheath entrance, the electric force is so small that it can be neglected

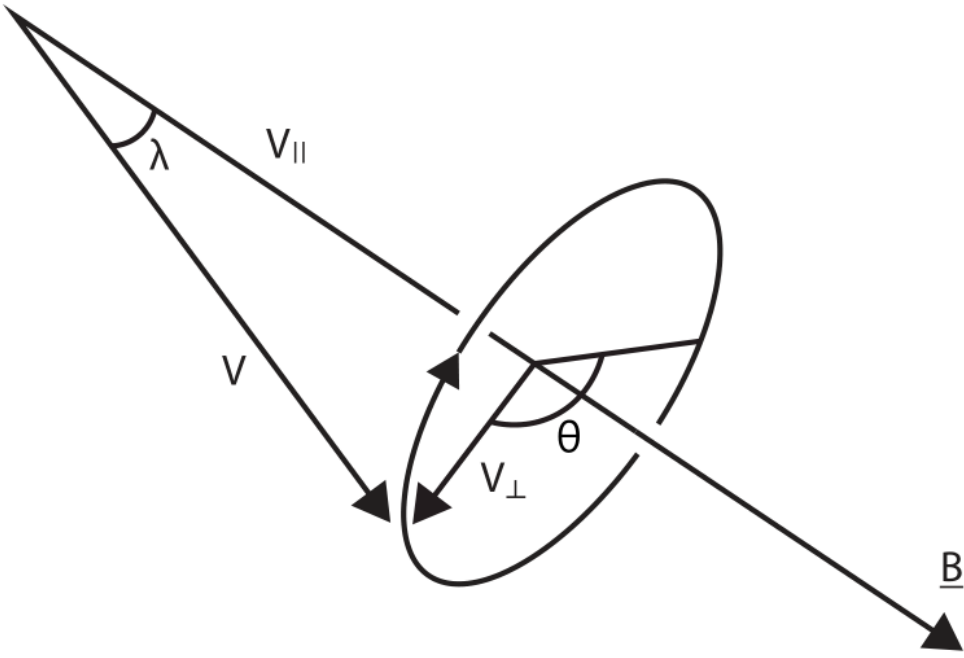


Figure 3.3: Velocity coordinates used, the velocity can be expressed using $(v_{\parallel}, v_{\perp}, \theta)$ with v_{\parallel} and v_{\perp} respectively representing the velocity parallel and perpendicular to the magnetic field. In another coordinate system the pitch angle $\lambda = \arctan\left(\frac{v_{\perp}}{v_{\parallel}}\right)$ is used to give the velocity as (v, λ, θ) .

compared with the magnetic force. If $v_{\parallel} < 0$, the particle will move away from the wall, while if $v_{\parallel} > 0$, the particle will move towards the wall. At the sheath entrance, no force can make v_{\parallel} change sign, and thus only particles with $v_{\parallel} > 0$ at the sheath entrance will hit the wall. Note that this means that ions in the magnetic presheath will always have $v_{\parallel} > 0$.

Hence, in the numerical scheme only particles with $v_{\parallel} > 0$ will be injected into the system, and their trajectory will be calculated until they will hit the wall. The trajectories are calculated numerically using a Runge-Kutta 4th order integrator with the equations of motion given by Equation 3.20. Then for each particle, the contribution to the density will be calculated by integrating the particle trajectory in time:

$$M^{\alpha\beta} \mathcal{N}_{i,\text{single}}^{\alpha} = \int_0^{\tau_i} dt v_{x,\infty} \Lambda^{\beta}(x'(t, \mathbf{v}_{\infty})). \quad (3.21)$$

Integrating these contributions for all possible entrance velocities will give the value of r^{β} .

3.4 Velocity sampling and entrance conditions

It turns out that it is not desirable to sample the velocities from Cartesian coordinates (v_x, v_y, v_z) . Instead, the particles are sampled from a spherical coordinate system (v, λ, θ) with v the magnitude of the velocity of the particle, λ the pitch angle, and θ the gyrophase angle. A graphical description of the coordinate system is shown in Figure 3.3. The mathematical description of these coordinates is:

$$\begin{aligned} \lambda &= \arctan\left(\frac{\sqrt{(v'_y)^2 + (v'_x)^2}}{v_{\parallel}}\right) \\ \theta &= \arctan\left(\frac{-v'_y}{v'_x}\right) \\ v &= \sqrt{v_{\parallel}^2 + (v'_y)^2 + (v'_x)^2}. \end{aligned} \quad (3.22)$$

To understand why this is useful, it is helpful to refer to Figure 3.4 where three different type of tra-

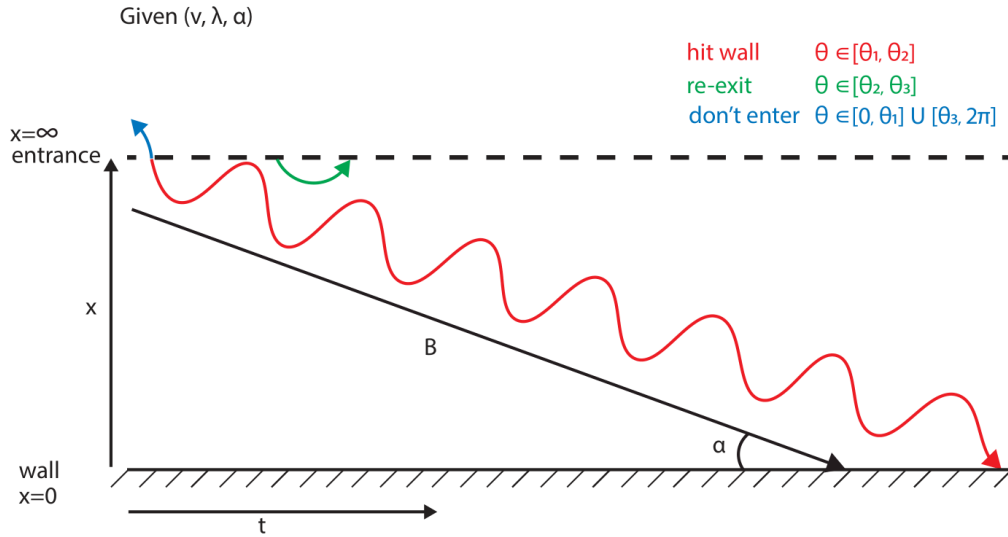


Figure 3.4: Figure showing the possible types of trajectories based on the velocity at the sheath entrance. Given a certain velocity v pitch angle λ at the sheath entrance and the angle of the magnetic field with the wall α , the type of trajectory purely depends on the gyrophase angle θ at the sheath entrance. The trajectory is an example of a trajectory that will hit the wall without re-exiting the system. The green trajectory is an example of a particle that will re-exit the system before hitting the wall. The blue trajectory is an example of a particle not entering the system.

jectories for particles with $v_{||} > 0$ are shown. Note that all these particles will eventually hit the wall because they have positive $v_{||}$, but depending on their v_∞ , only 2 of the 3 types of trajectories will enter the system: the green and the red curves. Again, the blue curve will eventually enter the system as it must hit the wall, but the trajectory of the blue curve still has a part that is outside of the system. If one would follow the trajectory outside the system one will find that the blue curve will arrive at the sheath entrance at a later time with a different v_∞ , at which point it almost certainly will enter the system. Since there will be an integration over all v_∞ , the particles that don't enter the system (blue curve) or the ones that enter and then re-exit (green curve) need only to be considered when they are in the system. When they exit, they need to be forgotten, since they will in fact be accounted for by integrating over all possible v_∞ at the sheath entrance. If one would follow all the trajectories until they hit the wall, one would double count most of the particles in the system. It might be insightful to realise that a particle from the blue trajectory will, if you let time pass, eventually become a green trajectory (with a different v_∞ , which will eventually become a red trajectory (with another different v_∞).

It is thus important to be able to analytically determine whether a trajectory will re-exit the system or reach the target without re-exiting. If most trajectories re-exit the system, the numerical sampling of the ones that do not re-exit must be enhanced. It turns out that given a certain v_∞ , λ_∞ , and magnetic field angle α the type of trajectory is determined by the particle's gyrophase at the sheath entrance θ_∞ . It turns out that if $\theta_\infty \in [\theta_1, \theta_2]$ the particle will enter the system at the considered v_∞ and will hit the wall without re-exiting (the red curve in Figure 3.4). The particles with $\theta_\infty \in [\theta_2, \theta_3]$ will enter the system at the considered v_∞ but will re-exit the system before hitting the wall (the green curve in Figure 3.4). The particles with $\theta_\infty \notin [\theta_1, \theta_3]$ will not enter the system at the considered v_∞ (the blue curve in Figure 3.4).

The calculation of θ_1 and θ_3 proceeds by noting that $v_x = 0$ at $\theta_\infty = \theta_1$ or $\theta_\infty = \theta_3$. From Equation 3.20 it can be seen that $v_x = v'_x \cos(\alpha) - v_{||}(\alpha)$, which gives in spherical coordinates:

$$v_x = v \sin(\lambda) \cos(\theta) \cos(\alpha) - v \cos(\lambda) \sin(\alpha). \quad (3.23)$$

One can then find that $v_x < 0$ when $\cos(\theta) < \frac{\tan(\alpha)}{\tan(\lambda)}$. One finds:

$$\begin{aligned} \theta_1 &= \arccos\left(\frac{\tan(\alpha)}{\tan(\lambda)}\right), \\ \theta_3 &= 2\pi - \theta_1, \end{aligned} \quad (3.24)$$

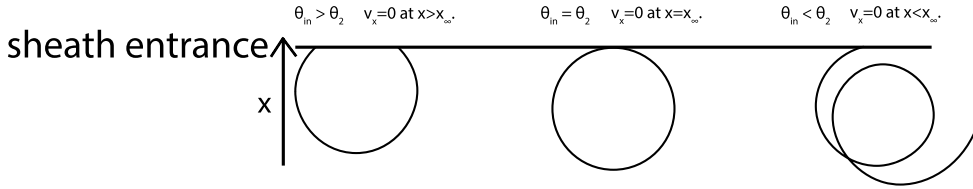


Figure 3.5: Three different trajectories entering the sheath are shown. The trajectory on the right will continue to hit the wall, i.e. it is part of trajectories 1. This means that its gyrophase when entering the sheath is smaller than θ_2 . It means that the second time the particle reaches $v_x = 0$, it will be at a location $x < x_\infty$. The trajectory on the left will re-exit the system, i.e. it is part of trajectories 2. This means that its gyrophase when entering the sheath is larger than θ_2 . It will reach $v_x = 0$ for the second time at a position $x > x_\infty$. Then the trajectory in the middle is the trajectory that glazes the sheath entrance, meaning that it is exactly in between being part of trajectories 2 and trajectories 1. This means that it enters the sheath with a gyrophase angle equal to θ_2 and it will reach its second $v_x = 0$ exactly when it is at position $x = x_\infty$.

such that if $\theta_\infty \in [\theta_1, \theta_3]$ the particle will enter the sheath system.

To find θ_2 , one has to look at the particle trajectories near the sheath entrance. They can be analytically obtained because near the sheath entrance the electrostatic force is negligible compared with the magnetic force. It thus makes sense to look at Equation 3.20 without an electric field:

$$\begin{aligned}\dot{x} &= v'_x \cos(\alpha) - v_{\parallel} \sin(\alpha) \\ \dot{v}'_x &= \Omega v'_y \\ \dot{v}'_y &= -\Omega v'_x \\ \dot{v}_{\parallel} &= 0.\end{aligned}\tag{3.25}$$

In particular one is interested in $x(t)$, which can be expressed in the coordinate system described in Equation 3.22 and shown in Figure 3.3. It becomes apparent that $v_{\parallel}(t) = v_{\parallel}$ is constant. One can find $v'_x(t)$ by taking the time derivative of the equation for \dot{v}'_x and inserting the equation for \dot{v}'_y . One finds that $v'_x(t) = \cos(\Omega t) v_{\perp} \cos(\theta_\infty) - \sin(\Omega t) v_{\perp} \sin(\theta_\infty)$, where $v_{\perp} = (v'_x)^2 + (v'_y)^2$ is constant and θ_∞ is the entrance gyrophase angle. The solution for $v'_x(t)$ can be written using a sum trigonometric identity as $v'_x(t) = v_{\perp} \cos(\Omega t + \theta_\infty)$. This means that the trajectory is given by:

$$x(t) = x_\infty + \frac{v_{\perp}}{\Omega} \cos(\alpha) [\sin(\Omega t + \theta_\infty) - \sin(\theta_\infty)] - \sin(\alpha) v_{\parallel} t.\tag{3.26}$$

It is important to note that a gyro-period is constant and equal to $\frac{2\pi}{\Omega}$. In Figure 3.5 three possible trajectories are drawn for particles entering the sheath system. Note that a particle entering the sheath with $\theta_\infty > \theta_2$ will re-exit the system, and a particle entering the sheath with $\theta_\infty < \theta_2$ will stay in the sheath to eventually hit the wall. There is a boundary case where a particle exactly grazes the sheath entrance. This means that when the particle reaches x_∞ for the second time, it will have $v_x = 0$. Since this is the boundary case, the particle exactly enters the sheath with $\theta_\infty = \theta_2$. It will graze the sheath entrance at $v_x = 0$ and this means that its gyrophase is $\theta_1 \bmod 2\pi$, because that is the solution for $v_x(\theta) = 0$ where v_x goes from positive to negative. As this happens after one gyro-orbit, it means that for the trajectory that grazes the sheath entrance $\theta = \theta_1 + 2\pi$. Since the particle started at $\theta_\infty = \theta_2$ it means that the particle has travelled a time equal to $\frac{2\pi + \theta_1 - \theta_2}{\Omega}$. This is because the particle enters the system at $\theta_2 > \theta_1$ and grazes the sheath entrance at $2\pi + \theta_1$. At this time $x(t) = x_\infty$ and thus θ_2 can be solved by solving (remember $\theta_\infty = \theta_2$):

$$\frac{v_{\perp}}{\Omega} \cos(\alpha) [\sin(2\pi + \theta_1) - \sin(\theta_2)] - \sin(\alpha) v_{\parallel} \frac{2\pi + \theta_1 - \theta_2}{\Omega} = 0.\tag{3.27}$$

This can be written as:

$$\sin(\theta_2) - \frac{\sin(\alpha)}{\tan(\lambda)} \theta_2 = \sin(\theta_1) - \frac{\tan(\alpha)}{\tan(\lambda)} (\theta_1 + 2\pi).\tag{3.28}$$

This equation gives the solution for θ_2 given λ , α and θ_1 . Hence, particles that will hit the wall before re-exiting are particles that are sampled from $\theta_\infty \in [\theta_1, \theta_2]$, while particles that re-exit the system are particles sampled from $\theta_\infty \in [\theta_2, \theta_3]$. This means that an appropriate sampling procedure goes as follows:

1. Sample m_v particles from their velocity $v \in [dv, v_{max}]$ with mesh size dv .
2. Sample $m_{\lambda,1}$ particles from $\lambda \in [\alpha, 2\pi]$ with mesh size $d\lambda_1$, and sample $m_{\lambda,2}$ particles from $\lambda \in [0, \alpha)$ with mesh size $d\lambda_2$.
3. Given λ and α calculate θ_1 and θ_3 .
4. Given λ , α and θ_1 calculate θ_2 .
5. Sample $m_{\theta,1}$ particles from $[\theta_1, \theta_2]$ with mesh size $d\theta_1$.
6. Sample $m_{\theta,2}$ particles from $[\theta_2, \theta_3]$ with mesh size $d\theta_2$.

It turns out that it is important to sample the particles that will hit the wall at the specified \mathbf{v}_∞ finely i.e. $d\theta_1$ should be small. To understand this fact one has to go back to the scheme of the ion density calculation, in particular when the transformation from v_x to $v_{x,\infty}$ was made. Looking at Equation 3.8 and Equation 3.7, something to note is how particles with turning points are handled. In Equation 3.7 particles with turning points have $v_x \rightarrow 0$. But when the integration variable is changed from \mathbf{v} to \mathbf{v}_∞ a singularity in the integrand occurs. This happens because $v_x \rightarrow 0$ and to get to the integral over \mathbf{v}_∞ conservation of phase space volume is used: $d^3\mathbf{v}' f_i(x', \mathbf{v}') = \frac{v_{x,\infty} f_{i,\infty}(\mathbf{v}_\infty)}{v'_x} d^3\mathbf{v}_\infty$. This relation has a singularity when $v'_x \rightarrow 0$. This singularity is not physical, and it therefore turns out to be integrable. The reason for the integrability is that the velocity v'_x will be integrated with respect to x in the scheme. It turns out that for when $v'_x \rightarrow 0$, $v'_x \propto \sqrt{x}$. This can be derived from looking at the equations of motion close to a turning point:

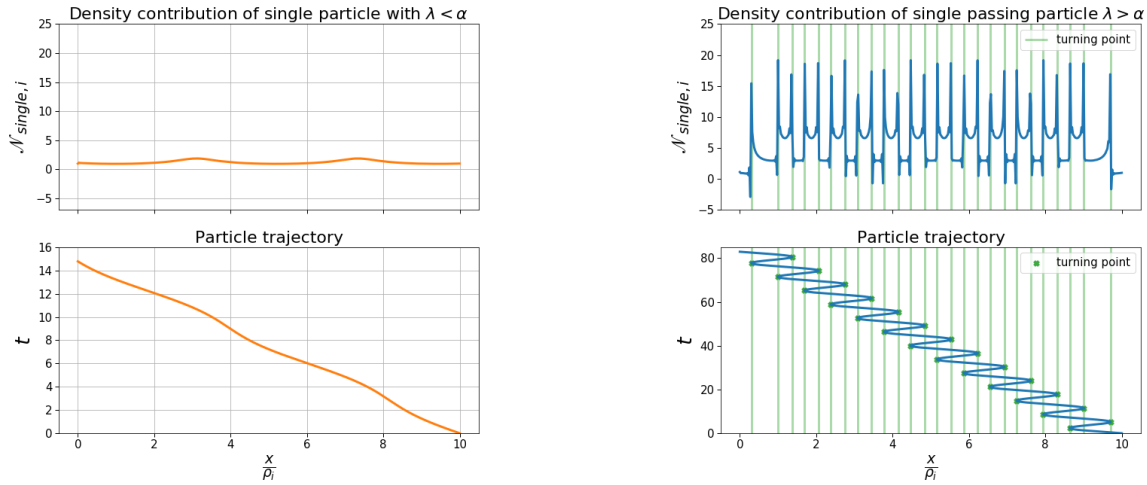
$$\begin{aligned}\dot{x} &= v_x \\ \dot{v}_x &= -\frac{\Omega}{B} \frac{d\phi}{dx} + \Omega v_y \cos(\alpha) \\ \dot{v}_y &= -\Omega v_x \cos(\alpha) - \Omega v_z \sin(\alpha) \\ \dot{v}_z &= \Omega v_y \sin(\alpha).\end{aligned}\tag{3.29}$$

Close to a turning point ($v_x \rightarrow 0$) $x(t)$ will be parabolic to leading order, which can be motivated by the use of a Taylor series around the turning point $x_{turning}$ at $t = t_{turning}$:

$$x(t) = x_{turning} + v_x(t - t_{turning}) + \dot{v}_x \frac{(t - t_{turning})^2}{2} + \mathcal{O}((t - t_{turning})^3).$$

Close to a turning point $v_x \approx 0$ and thus $x(t) \propto t^2$, which in turn means that $v_x \propto t$. Because of this $v_x \propto \sqrt{x}$, and thus the integral over x with the term $\frac{1}{v_x}$ is integrable.

It is important to understand how this singularity manifests itself in the numerical scheme. The density is obtained by Equation 3.11, where there is no integration over x and there is no $\frac{1}{v_x}$ term. Instead the space is discretised and there is an integral over the time a particle spends in the grid-cell. The time a particle spends in the grid-cell is always finite and never diverges. Instead of a divergence one sees some particles, near a turning point, spending a very large time in one specific grid-cell. The range of gyrophase angles for which this happens is small, and must be resolved properly to obtain the density contribution from particles in their turning points correctly. This means that after integrating over sufficiently many θ_∞ the density contribution will be represented correctly. There is however a subtlety in this; the integral is discretised; each basis function has a finite support, meaning it has a finite range on which it is non zero. The integral gives one value to each β of the basis function. If one of those becomes inaccurate because of the turning points the single particle density becomes inaccurate at the location where that specific basis function is non zero. So for each basis function, or for each element, the integral over θ must be accurate enough to integrate the particles with turning points correctly. This means that there need to be enough particles with turning points in a specific element, to make sure that their behaviour is well resolved. So increasing the spatial grid resolution can only be done if the numerical velocity resolution is increased accordingly. This makes it numerically expensive to work with fine x grids, and it is desirable to keep the x -grid as coarse as possible to describe the potential



(a) Density contribution and trajectory of a particle with $\lambda < \alpha$, so without turning points. As can be seen the density contribution of this particle as defined by Equation 3.21 does not diverge.

(b) Density contribution and trajectory of a particle with $\lambda > \alpha$, so with turning points. The density contribution of this particle as defined by Equation 3.21 diverges when the particle has a turning point.

Figure 3.6: Two different particle trajectories and their density contributions. This highlights how turning points of particles interact with the density contribution.

field accurately. In Figure 3.6b the divergences of the single particle trajectory density contributions are plotted. And as can be seen, the density contribution spikes up when a particle reaches a turning point. In Figure 3.6a the density contribution of a particle that does not have turning points can be seen. It can be seen that these particles do not have these spikes in their density contribution.

To highlight the fact that these spikes disappear when integrating over velocities, one can numerically calculate the density of a single gyroring. With a gyroring, it is meant that one integrates over all the possible gyroangles. The density contribution is then given by:

$$M^{\alpha\beta} \mathcal{N}_{i,gyro}^\alpha = \frac{1}{2\pi} \int_0^{2\pi} d\theta_\infty \int_0^{\tau_i} dt v_{x,\infty} \Lambda^\beta(x(t, \theta_\infty)). \quad (3.30)$$

This should integrate out the spikes in $\int_0^{\tau_i} dt v_{x,\infty} \Lambda(x'(t, \theta_\infty))$. In Figure 3.7 the density contribution of a single gyroring is shown compared with the analytical result. This simulation is done for a velocity $v = v_{th}$, a pitch angle $\lambda = 0.9\frac{\pi}{2}$ and $\alpha = \frac{\pi}{4}$. The derivation can be found in Appendix A. It can be seen that, indeed, the spikes have disappeared due to the integration over θ_∞ . Notably, the numerical solution does not recover the analytical result exactly. There are two locations where it struggles, at the wall at $x = 0$ and at the point where the first particles start hitting the wall. The reason that the numerical solution struggles there is inherently linked to the numerical method. The analytical solution namely has a discontinuity in its derivative at both locations. The density contribution close to the wall follows a \sqrt{x} behaviour, and thus the derivative of the density contribution diverges at $x = 0$. Similarly, before the particles start hitting the wall, the density contribution is completely flat. But when the particles start hitting the wall, the density contribution starts to drop linearly, and thus has a discontinuous jump in the derivative.

For the finite element method to work, the function that one wants to describe should have a continuous derivative [37]. This is the reason that the finite element method struggles to represent the density contribution from a gyroring in these regions. Since particles with different \mathbf{v}_∞ will start hitting the wall at different locations. Conversely, the discontinuity in the analytical gyro-orbit density contribution will disappear when integrating over all possible v and λ . The discrepancy between the analytical solution and the numerical solution at $x = 0$ is not expected to be solved by integrating over the other velocity coordinates because the density contribution from all possible gyro-rings has the same discontinuous derivative at $x=0$. Hence, a grid in x has to be defined carefully resolve this discontinuity.

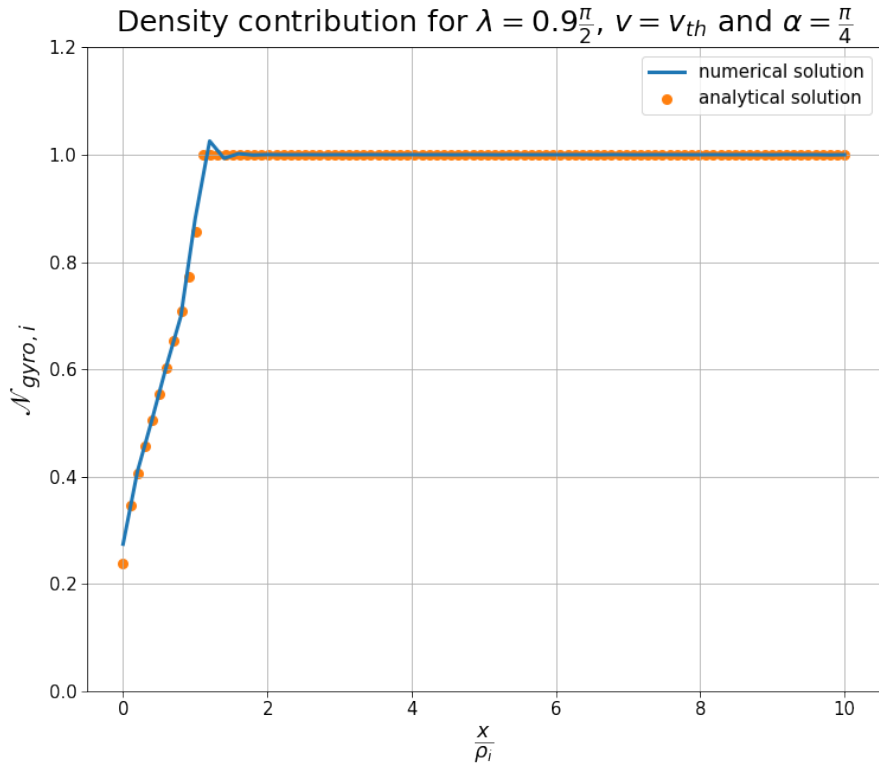


Figure 3.7: Graph of the density contribution of a single gyroring as defined by Equation 3.30 compared with the analytical result derived in Appendix A. It can be seen that there are no more divergences but that the numerical method struggles only at the points where the derivative of the analytical function is either discontinuous or diverges.

3.5 Self-consistent potential

In this section the iterative method to find the self-consistent potential field is shown. The section is split into a part that discusses the magnetic presheath and the entire magnetised sheath. The scheme to find the magnetic presheath solution is a special case of the magnetised sheath method.

3.5.1 Magnetic presheath

The quasi-neutrality equation with Boltzmann electrons is given by:

$$n_{e,\infty} e^{\frac{e\phi}{T_e}} = Z n_i(x), \quad (3.31)$$

with $\phi = 0$ at $x = x_\infty$ the entrance of the magnetic presheath. In the normalised units considered in Equation 3.3 this equation becomes:

$$e^{\phi(x)} = n_i(x), \quad (3.32)$$

where n_i is the normalised ion density and the hats are dropped to avoid confusion with the finite element coefficients. At iteration k $n_{i,k}$ is the density profile obtained by solving Equation 3.12 with potential ϕ_k . Then the potential will get updated such that at the next iteration it satisfies quasi-neutrality with the density of the previous iteration i.e. $e^{\phi_{k+1}} = n_{i,k}$. To get a linear equation in ϕ_{k+1} a multiplication with $e^{-\phi_k}$ is done: $e^{\phi_{k+1}-\phi_k} = e^{-\phi_k} n_{i,k}$. Taylor expanding the left hand side in small values of $\phi_{k+1} - \phi_k$ the final scheme is obtained:

$$\phi_{k+1} = \phi_k + e^{-\phi_k} (n_{i,k} - e^{\phi_k}). \quad (3.33)$$

It is clear that the potential gets updated depending on how well the previous iteration satisfied quasi-neutrality. This equation has to be discretised. For this, the finite element method is used. The potential

field is written in terms of finite element basis functions:

$$\phi_k(x) = \sum_{\alpha} \hat{\phi}_k^{\alpha} \Lambda^{\alpha}(x). \quad (3.34)$$

Projecting Equation 3.33 onto finite elements the following is obtained:

$$\hat{\phi}_{k+1}^{\alpha} M^{\beta\alpha} = \tilde{r}_k^{\beta}, \quad (3.35)$$

where $M^{\beta\alpha}$ is the same mass matrix as in Equation 3.12 and \tilde{r}^{β} a vector given by:

$$\tilde{r}^{\beta} = \int_0^{\infty} dx \left[\hat{\phi}_k^{\gamma} \Lambda^{\gamma}(x) + \exp(-\hat{\phi}_k^{\gamma} \Lambda^{\gamma}(x)) \left(\hat{n}_{i,k}^{\gamma} \Lambda^{\gamma}(x) - \hat{\phi}_k^{\gamma} \Lambda^{\gamma}(x) \right) \Lambda^{\beta}(x) \right], \quad (3.36)$$

where repeated Greek indices are summed over. This scheme allows for finding a quasi-neutral self consistent electric field.

In practice using Equation 3.35 directly to obtain the potential of the next iteration might be unstable. Therefore actually the following relation is used:

$$\phi_{k+1}^{\alpha} = (1-w)\phi_k^{\alpha} + w(M^{\beta\alpha})^{-1} \tilde{r}_k^{\beta}, \quad (3.37)$$

where w is a scalar weight for the next update, usually $w \in [0.2, 0.3]$.

3.5.2 Magnetised sheath

Simulating the Debye sheath together with the magnetic presheath by solving the steady state directly would be a paradigm shift: it would allow the simulation of the magnetic presheath in the time and length scales of a gyro-orbit, while resolving the Debye sheath length and time scales only where it is necessary (in the Debye sheath). In contrast to this, PIC codes simulate the time evolution of the magnetised sheath by resolving the Debye length and the plasma frequency everywhere, while Eulerian codes can adapt the spatial grid but are still constrained to resolve the dynamics at the plasma frequency timescale. This already shows the potential speedup of this approach. By including the Debye sheath, the problem setting changes compared with the one highlighted in Section 3.1. The magnetised sheath system does not satisfy quasi-neutrality everywhere. To find a potential updating scheme it is useful to look at Equation 3.5 and define $\gamma = \frac{\lambda_D}{\rho_i}$:

$$\gamma^2 \frac{d^2\phi}{dx^2} = n_i - n_e, \quad (3.38)$$

where all quantities are normalised like in Equation 3.3, but the hats are dropped to avoid confusion with the finite element coefficients. The potential updating scheme derived in Section 3.5.1 does not hold in this case. For this, a completely new updating scheme is developed, which will work inside the magnetic presheath as well as in the Debye sheath. Given the potential field of the previous iteration ϕ_k and the ion density of the previous iteration $n_{i,k}$, the potential field for the next iteration is updated, imposing that the next iteration solves Poisson's equation with the ion density of the previous iteration:

$$\begin{aligned} \gamma^2 \phi''_{k+1} &= e^{\phi_{k+1}} - n_{i,k}, \\ \gamma^2 \phi''_{k+1} &= e^{\phi_{k+1}-\phi_k} e^{\phi_k} - n_{i,k}. \end{aligned} \quad (3.39)$$

Linearising $e^{\phi_{k+1}-\phi_k}$ one then obtains the updating scheme that will be used:

$$\gamma^2 \phi''_{k+1} - \phi_{k+1} e^{\phi_k} = e^{\phi_k} [e^{-\phi_k} (e^{\phi_k} - n_{i,k}) - \phi_k], \quad (3.40)$$

which results in the scheme used for the magnetic presheath if $\gamma^2 \frac{d^2\phi^{k+1}}{dx^2} \ll 1$. Projected on finite elements this scheme becomes:

$$\hat{\phi}_{k+1}^{\alpha} \int_0^{\infty} \left[\gamma^2 \Lambda^{\alpha\prime\prime}(x) \Lambda^{\beta}(x) - e^{\phi_k(x)} \Lambda^{\alpha}(x) \Lambda^{\beta}(x) \right] dx = \int_0^{\infty} \left[(e^{\phi_k(x)} - n_{i,k}(x)) - e^{\phi_k(x)} \phi_k(x) \right] \Lambda^{\beta}(x) dx. \quad (3.41)$$

After integration by parts:

$$\hat{\phi}_{k+1}^{\alpha} \int_0^{\infty} \left[\gamma^2 \Lambda^{\alpha\prime}(x) \Lambda^{\beta\prime}(x) + e^{\phi_k(x)} \Lambda^{\alpha}(x) \Lambda^{\beta}(x) \right] dx = \int_0^{\infty} [\phi_k - e^{-\phi_k} (e^{\phi_k} - n_{i,k})] e^{\phi_k(x)} \Lambda^{\beta}(x) dx, \quad (3.42)$$

where the boundary terms $\phi_{k+1}^\alpha \gamma^2 [\lambda^{\alpha'}(x) \lambda^\beta(x)]_0^\infty$ have been ignored because Dirichlet boundary conditions need to be imposed, meaning that the boundary terms of the integration by parts are zero because all the basis functions but the two boundary ones are zero on the boundary. These Dirichlet boundary conditions are denoted by ϕ_0 , the potential at the wall, and ϕ_∞ , the potential at x_∞ (generally zero). The equation can again be written in matrix vector form:

$$\hat{\phi}_{k+1}^\alpha G_k^{\alpha\beta} = \bar{r}_k^\beta. \quad (3.43)$$

Here \bar{r}_k^β is almost the same as in Equation 3.36, but with an extra factor of e^{ϕ_k} in the integrand, and it is given by:

$$\bar{r}_k^\beta = \int_0^\infty [\phi_k - e^{-\phi_k} (e^{\phi_k} - n_{i,k})] e^{\phi_k(x)} \Lambda^\beta(x) dx, \quad (3.44)$$

and matrix $G_k^{\alpha\beta}$ is defined as:

$$G_k^{\alpha\beta} = D^{\alpha\beta} + \tilde{M}_k^{\alpha\beta}. \quad (3.45)$$

Here $\tilde{M}_k^{\alpha\beta}$ is almost the same mass matrix as seen before but instead given by:

$$\tilde{M}^{\alpha\beta} = \int_0^\infty e^{\phi_k(x)} \Lambda^\alpha(x) \Lambda^\beta(x) dx, \quad (3.46)$$

and

$$D^{\alpha\beta} = \gamma^2 \int_0^\infty \Lambda^{\alpha'}(x) \Lambda^{\beta'}(x) dx. \quad (3.47)$$

It is worth to write the equation out to see how the boundary conditions are implemented in this approach:

$$\begin{pmatrix} 1 & 0 & 0 & \cdots & 0 \\ G_k^{2,1} & G_k^{2,2} & G_k^{2,3} & \cdots & G_k^{2,N+p-1} \\ \vdots & \ddots & \ddots & \ddots & \vdots \\ G_k^{N+p-2,1} & G_k^{N+p-2,2} & G_k^{N+p-2,3} & \cdots & G_k^{N+p-1,N+p-1} \\ 0 & 0 & 0 & \cdots & 1 \end{pmatrix} \begin{pmatrix} \hat{\phi}_{k+1}^1 \\ \hat{\phi}_{k+1}^2 \\ \vdots \\ \hat{\phi}_{k+1}^{N+p-2} \\ \hat{\phi}_{k+1}^{N+p-1} \end{pmatrix} = \begin{pmatrix} \phi_0 \\ \bar{r}_k^2 \\ \vdots \\ \bar{r}_k^{N+p-2} \\ \phi_\infty \end{pmatrix}. \quad (3.48)$$

This makes sure that the boundary conditions are satisfied at each iteration. The final updating scheme with a weight w becomes:

$$\phi_{k+1}^\alpha = (1-w)\phi_k^\alpha + w \left(G_k^{\beta\alpha} \right)^{-1} \bar{r}_k^\beta. \quad (3.49)$$

3.6 Definition of the spatial grid

3.6.1 Magnetic presheath

As will be proven in Section 4.1 the potential in the magnetic presheath will follow a \sqrt{x} dependence close to $x = 0$. In Figure 3.8 a potential profile obtained from the numerical scheme to solve the magnetic presheath for a magnetic field angle of $\alpha = \pi/100$ can be seen, compared with the semi-analytical result by Geraldini [13, 14, 7]. In the simulation an equidistant grid spacing was used of $dx = \rho_i/5$. It can be seen that the potential profile obtained has a significant error compared with the one obtained by Geraldini's small-angle code. This is because of the \sqrt{x} dependence near $x = 0$, an equidistant grid spacing in x cannot capture the large potential drop near the wall. Motivated by this, it makes sense to define a grid that is equidistant in \sqrt{x} near the wall and equidistant in x far away from the wall, not to over-resolve the problem far away from the wall. The definition of the grid is taken from [7] and is given by:

$$x_i = \left(\sqrt{\kappa + i\delta} - \sqrt{\kappa} \right)^2. \quad (3.50)$$

Here $i \geq 0$ is the i -th grid point in x , κ and δ are constants that determine the grid spacing. In this equation, x is normalised with respect to the ion Larmor radius. If $\kappa = 0$, the grid spacing is equidistant in x . Unless stated otherwise, $\kappa = 1$ in the simulation results below.

Describing a function $f(x)$ with \sqrt{x} behavior close to $x = 0$ is, however, not solved entirely by this definition of the grid. The function \sqrt{x} has a divergent derivative around $x = 0$, this means that it is not possible to describe the function with finite elements, because it is not Taylor expandable [37]. The result of trying to describe a function $f(x)$ that has \sqrt{x} dependence close to $x = 0$ is shown in Figure 3.9. It is good to keep this in mind, although making the grid finer and finer around $x = 0$ will ensure that the \sqrt{x} behavior is approximated better.

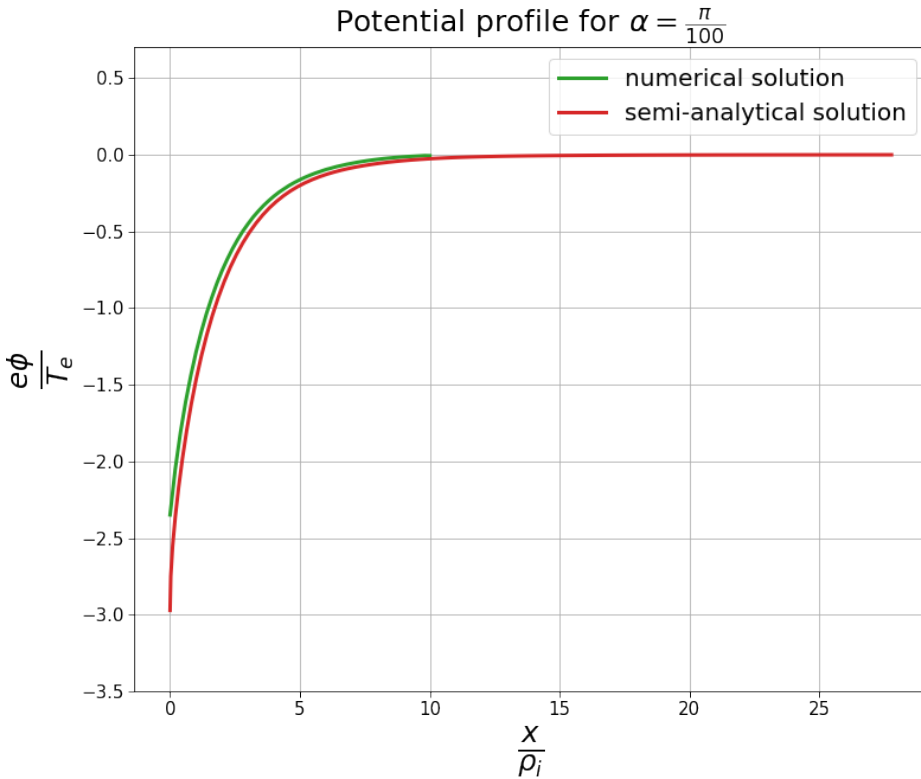


Figure 3.8: Numerically obtained self-consistent potential with a grid equidistantly spaced in x and an magnetic field angle $\alpha = \pi/100$. This highlights that the numerical method struggles near $x = 0$, because there the potential is expected to have a \sqrt{x} dependence. This means that the derivative of the potential $\phi(x)$ around $x = 0$ is divergent.

3.6.2 Magnetised sheath

If the Debye sheath is included, the \sqrt{x} behavior disappears because the only reason why this \sqrt{x} behaviour occurs, as will be shown in Section 4.1, is the quasi-neutrality condition. This condition is not valid anymore at distances from the wall comparable to the Debye length. The \sqrt{x} behaviour close to the wall in the magnetic presheath is nonphysical, as it results in a divergent electric field and thus a divergent force. In that sense, it is logical that this dependence disappears when getting rid of the scale separation. The grid in the magnetised sheath should resolve the Debye length only where necessary i.e. close to the wall, and should resolve the ion Larmor radius everywhere else. This is done by having an equidistant grid in x with grid spacing Δx_{ds} close to the wall: up to $m\lambda_D$ away from the wall, with $m \in \mathbb{N}$. After that, a grid that again is defined like Equation 3.50 but then with $m\lambda_D$ added to it, to make it start at $m\lambda_D$. This gives the definition of the grid:

$$x_i = \begin{cases} i\Delta x_{ds} & \text{for } i \leq m \frac{\lambda_D}{\Delta x_{ds}} \\ \left(\sqrt{\kappa + \left(i - m \frac{\lambda_D}{\Delta x_{ds}} \right) \delta} - \sqrt{\kappa} \right)^2 + m\lambda_D & \text{for } i > m \frac{\lambda_D}{\Delta x_{ds}}, \end{cases} \quad (3.51)$$

where $i \geq 0$ indicates the i -th grid point in the x -grid.

3.7 Speeding up the code

In this section the methods used for speeding up the code are discussed. First, the parallelisation procedure is explained, in the case of the numerical method developed here it is relatively straightforward. Then there will be section that highlights the importance of breaking down the problem into smaller pieces. Intuitively one would think that it is not possible to solve the particle trajectories inside the magnetised sheath for an arbitrary electric field analytically. However, when one looks closely at the

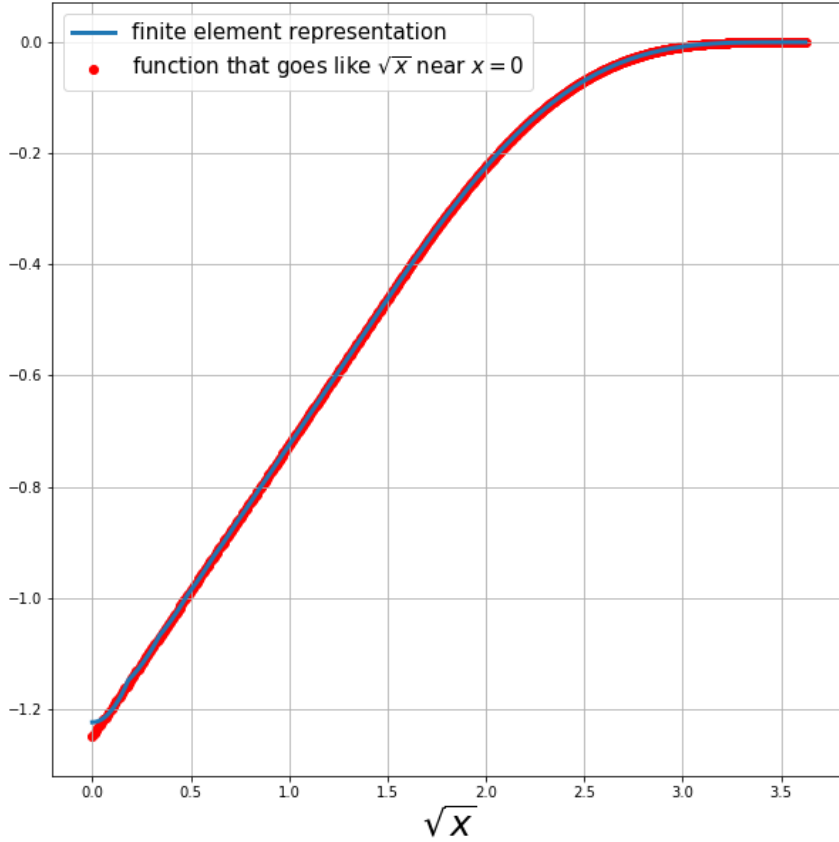


Figure 3.9: Finite element representation with quadratic basis functions of a function that goes with \sqrt{x} close to $x = 0$. Showing that the representation has trouble around $x = 0$.

problem one notices that the electric field is piece-wise constant when linear basis functions are used. This means that the particle trajectories can actually be solved piece-wise analytically. This paradigm shift will greatly decrease the computational cost of the numerical method.

3.7.1 Parallelisation

The idea of parallelisation is to distribute the tasks between multiple processor cores. Implemented correctly, this leads to a speedup. The nature of the approach described in the report lends it to be easily parallelised. Each thread can treat one trajectory at once. When all particles have finished their trajectories, they combine their results on the master thread. Integrating all particle trajectories over their velocity space and time yields the vector r^β from Equation 3.12. The most important notion for this parallelisation to work properly is that each thread will need to have a **private** copy of the vector. Each thread i has a separate vector r_i^β that is initialized to 0 when the integration over \mathbf{v} is started. They write the particle contribution to the density of the private vector. At the end, the total vector r_{total}^β is calculated by summing over all the N threads:

$$r_{total}^\beta = \sum_i^N r_i^\beta. \quad (3.52)$$

A second point to realise is that the workload of each thread is not at all constant. Seen on Figure 3.10 are two different ways of offloading the work to different threads in a loop. On the y -axis, the workload is depicted for different tasks. In the case of static offloading: the tasks will be distributed in terms of

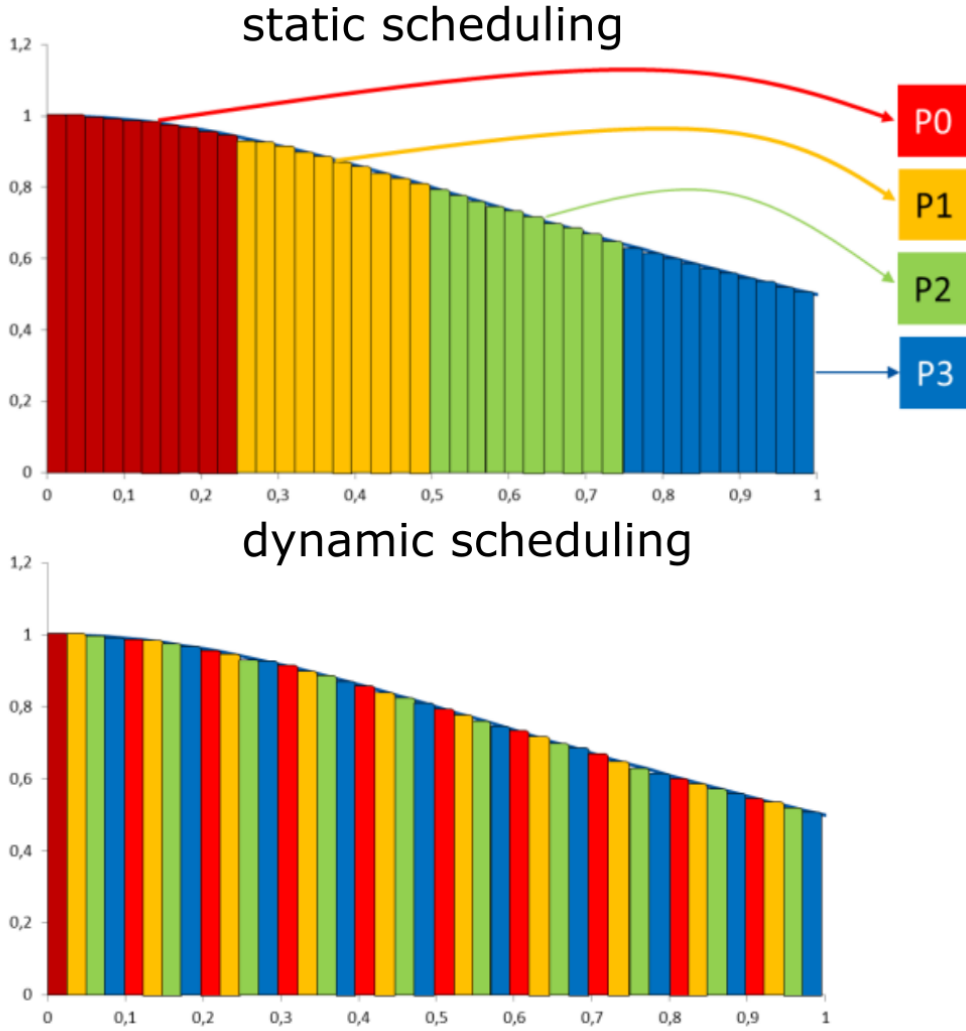


Figure 3.10: The difference between dynamic and static scheduling in parallel loops. The tasks executed by different threads are color coded. In the case of static scheduling a batch is pre-defined, while in the case of dynamic scheduling the tasks are given to the threads on the go. The x-axis represents the number of tasks that have to be performed while the y-axis represents the workload. Retrieved from [40].

batches over the different threads. While in dynamic scheduling: the tasks in the loop will be distributed according to when a task is finished. If the workload of tasks is equal, the static scheduling is faster because it has less overhead, but if the workload is very far from equal, the dynamic scheduling is faster. The latter is the case for integrating through the particle trajectories, because there are particle trajectories that are long. Particles with long trajectories have low velocity v and large pitch angle λ and particles with short trajectories have a large velocity v and a small pitch angle $\lambda < \alpha$. So the best way is to give the threads new tasks based on when they finished and not give the tasks in predefined batches. Otherwise, there will be one thread still running its long trajectories while the others are idle.

3.7.2 Piece-wise constant electric field

In this section a speedup of the code is discussed, this speedup is related to the fact that with linear basis functions, the potential is piece-wise linear inside the grid cells. This means that in each grid cell the electric field is piece-wise constant, resulting in local equations of motion that can be solved analytically. To explain this, the section is split up into different parts. The first section (Section 3.7.2.1) will discuss the analytical trajectories inside the grid cell. It turns out that it is necessary to know the time a particle spends in a grid cell (denoted as τ) to obtain the density contribution of each particle to a specific grid cell. To obtain τ it is necessary to understand the different type of trajectories particles can have inside the grid cell. The second section (Section 3.7.2.2) will discuss these different trajectories, and more

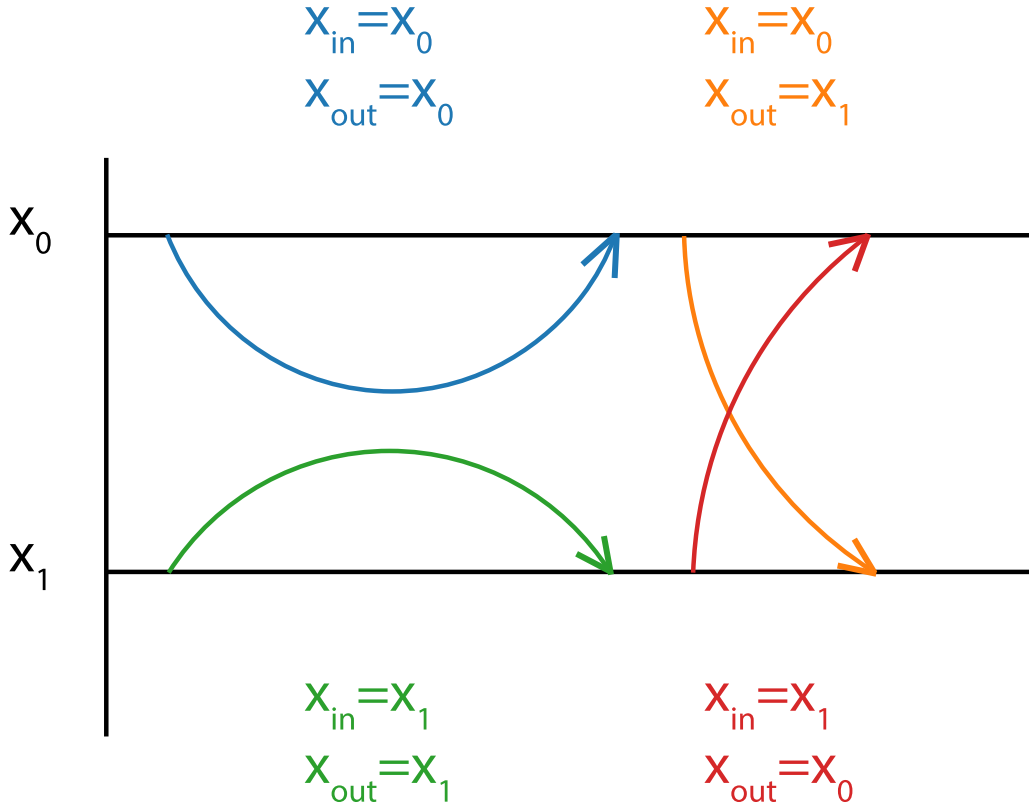


Figure 3.11: Different possible $v_x(t)$ curves with $v_{\parallel} > 0$ and turning points points where $\dot{v}_x(t) = 0$. It is important to acknowledge the curves and distinguish them based on their $v_x(0)$ and $\dot{v}_x(0)$ as is explained below.

importantly, discusses tests to distinguish them from each other. The final section (Section 3.7.2.3) will then combine everything and explain the entire algorithm.

3.7.2.1 Particles in a constant electric field

As stated before if first-order basis functions are used, the electric field is piece-wise constant because it is the derivative of the piece-wise linear basis functions. It is possible to obtain the particle trajectories in a constant electric field analytically. So looking at the elements separately, the trajectory inside the element can be obtained analytically. Suppose a particle is at the entrance of a grid cell at time $t = 0$, at location $x_{in} \in \{x_0, x_1\}$ with $x_0 > x_1$ with velocity \mathbf{v}_0 then suppose that the particle will re-exit the grid cell at $x_{out} \in \{x_0, x_1\}$ at time τ . Note that a particle entering at x_0 can exit at both x_0 and x_1 , since the particles can have turning points. Similarly, a particle entering at x_1 can exit at both x_0 and x_1 . A simplified depiction is shown in Figure 3.11, which does not show particles with more than 1 turning point in a specific grid cell. The analysis below allows for those particles none the less.

It is possible to find the trajectory of the particle inside the grid cell analytically. The electric field is locally constant and denoted by κ , so the equations of motion are given by:

$$\begin{aligned}\dot{x} &= v_{x'} \cos(\alpha) - v_{\parallel} \sin(\alpha) \\ \dot{v}_{x'} &= -\frac{\Omega}{B} \kappa \cos(\alpha) + \Omega v_y \\ \dot{v}_y &= -\Omega v_{x'} \\ \dot{v}_{\parallel} &= \frac{\Omega}{B} \sin(\alpha) \kappa.\end{aligned}\tag{3.53}$$

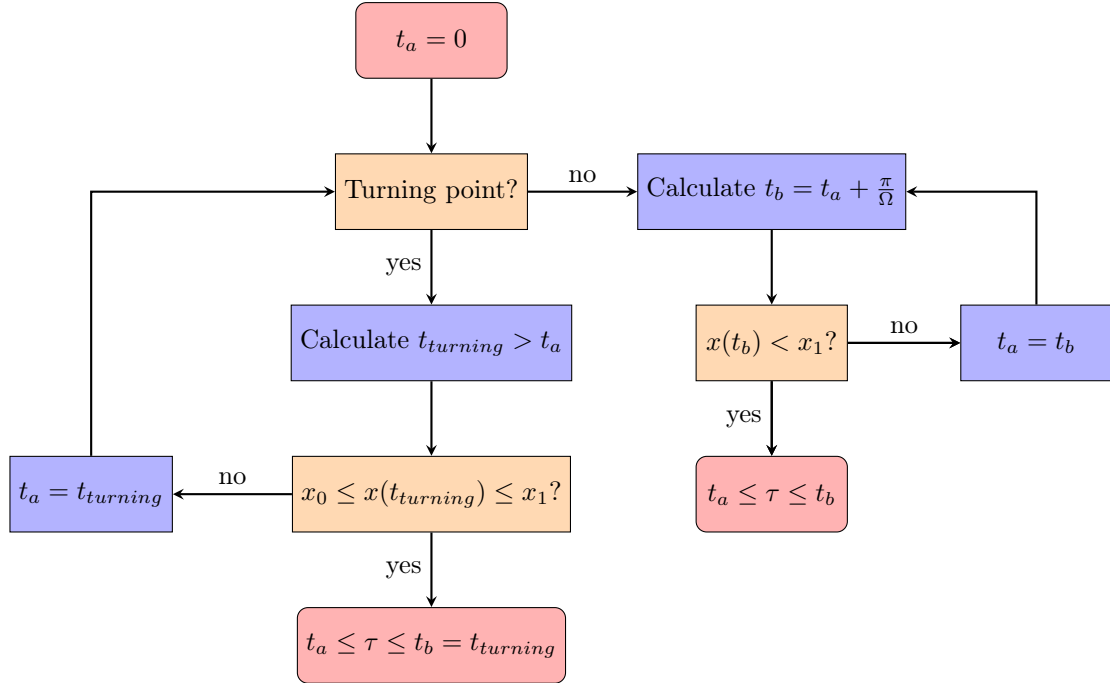


Figure 3.12: Decision flow chart for finding t_a and t_b .

Solving these equations gives the equations for $x(t)$ and $\mathbf{v}(t)$,

$$\begin{aligned}
 x(t) &= -\frac{\cos(\alpha)[2A_2B\sin(\Omega t) + 2A_1B\cos(\Omega t) - 2A_1B]}{2B\Omega} - \sin(\alpha)\left[\frac{\Omega}{2B}\sin(\alpha)\kappa t^2 + v_{\parallel,0}t\right] + x_{in} \\
 v_{x'} &= \sin(\Omega t)A_1 - \cos(\Omega t)A_2 \\
 v_y(t) &= \frac{\kappa}{B}\cos(\alpha) + A_1\cos(\Omega t) + A_2\sin(\Omega t) \\
 v_{\parallel}(t) &= \frac{\Omega}{B}\sin(\alpha)\kappa t + v_{\parallel,0}.
 \end{aligned} \tag{3.54}$$

Here $A_1 = A_1 = v_{y,0} - \frac{\kappa}{B}\cos(\alpha)$, and $A_2 = -v_{x',0}$. One can then directly obtain the density contribution from a single particle, which is obtained by time integrating along the trajectory of basis functions evaluated at the trajectory position, $\int_0^\tau \Lambda^\alpha(x(t))dt$. In case of linear basis functions, there will be 2 non-zero basis functions in each element. It is useful to write the equation linear basis functions given in Equation 3.15 in a local form. Meaning that one looks at one specific element, and defines the basis functions relative to that element. Looking at Figure 3.2 one can see that in each element there are two basis functions, one that goes linearly down from 1 to 0 and one that goes linearly up from 0 to 1. Suppose the length of the element is given by h , then one basis function in this element is defined by $\Lambda_0(x(t)) = \frac{-x(t)+x_1}{h} + 1$, and the other is defined by $\Lambda_1(x(t)) = \frac{x(t)-x_1}{h}$. The integration of these functions in time gives:

$$\begin{aligned}
 \int_0^\tau \Lambda_0(x(t))dt &= \frac{\tau x_1 - \tau x_{in}}{h} + \frac{\sin(\alpha)\tau^2 v_{\parallel,0}}{2h} + \frac{A_1 \cos(\alpha) \sin(\Omega\tau) - A_2 \cos(\alpha) \cos(\Omega\tau) + A_2 \cos(\alpha)}{h\Omega^2} \\
 &\quad + \frac{\sin^2(\alpha)\kappa\Omega\tau^3}{6Bh} + \frac{(h\Omega - A_1\cos(\alpha))\tau}{h\Omega} \\
 \int_0^\tau \Lambda_1(x(t))dt &= \int_0^\tau [1 - \Lambda_0(x(t))]dt = \tau - \int_0^\tau \Lambda_0(x(t))dt.
 \end{aligned} \tag{3.55}$$

However, τ is not a priori known, because it corresponds to the time spent by a particle in a given spatial interval. Calculating τ requires inverting $x(t)$, which is not possible analytically. In the rest of this section, a numerical scheme is devised to calculate τ . To do this it is first important to analyse the different type of velocity trajectories which will be done in the next section.

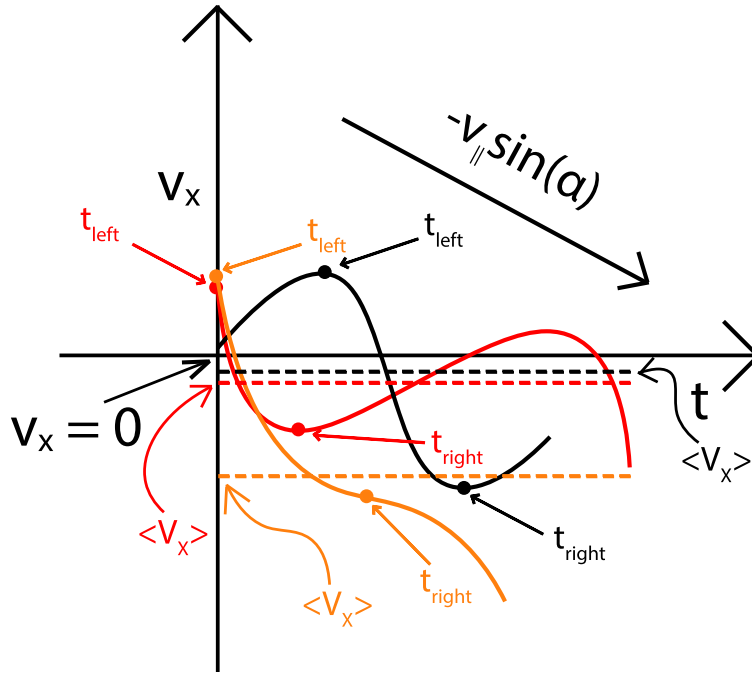


Figure 3.13: Different possible $v_x(t)$ curves with $v_{\parallel} > 0$ and turning points points where $v_x(t) = 0$. These are the three possible curves that are allowed with $v_x(0) > 0$. Note that all curves have $\langle v_x \rangle < 0$, and the positions of t_{left} and t_{right} have been indicated for each curve.

3.7.2.2 Algorithm for distinguishing the different types of trajectories in a grid cell

This scheme is based on a methodical analysis of the particle trajectories in a given grid cell. First note that a root finder can be used if two times are found named t_a and t_b such that $\tau \in [t_a, t_b]$ and there are no turning points in between t_a and t_b , such that $x(\tau)$ is monotonic in the range $\tau \in [t_a, t_b]$. To find t_a and t_b it is insightful to look at Figure 3.11. For the orange and the red trajectory, the time τ is in between 0 and the time of the next turning point (the next turning point is not shown). For the blue and green trajectory τ is in between the time of the first and the second turning point (the second turning point is not shown). Generalising for trajectories with N turning points the time τ will be in between the N -th turning point and the $N + 1$ th turning point. This is only necessary for particles with turning points; particles without turning points are essentially easier to deal with. A particle that does not have turning points anymore, will enter the cell at x_0 and exit it at x_1 . This is because the ion will need to hit the wall and thus will move downwards on average. If the particle does not have a turning point t_b will be increased in steps of $\frac{\pi}{\Omega}$ (half a gyroperiod) until t_a and t_b are found such that $x(t_a) > x_1$ and $x(t_b) < x_1$. Finding t_a and t_b will be the first building block of the numerical algorithm and the decision flow chart is depicted in Figure 3.12.

Note that to find $t_{turning}$ one would need to solve $v_x(t) = 0$. From Equation 3.54 it can be seen that $v_x(t)$ will be sinusoidal function added to a linear function. This function is not analytically invertible and thus a root finder will also need to be used to find $t_{turning}$. This means that again two times need to be found named t_{left} and t_{right} such that $t_{turning}$ is in between t_{left} and t_{right} and $\dot{v}_x \neq 0$ in between t_{left} and t_{right} . To find t_{left} and t_{right} a similar approach is used as to find t_a and t_b . For t_a and t_b one needed to find $t_{turning}$, while now one will need to find the times where $\dot{v}_x = 0$. Solving $\dot{v}_x = 0$ is possible analytically:

$$A_2 \cos(\alpha)\Omega \sin(\Omega t) + A_1 \cos(\alpha)\Omega \cos(\Omega t) - \sin^2(\alpha) \frac{\Omega}{B} \kappa = 0. \quad (3.56)$$

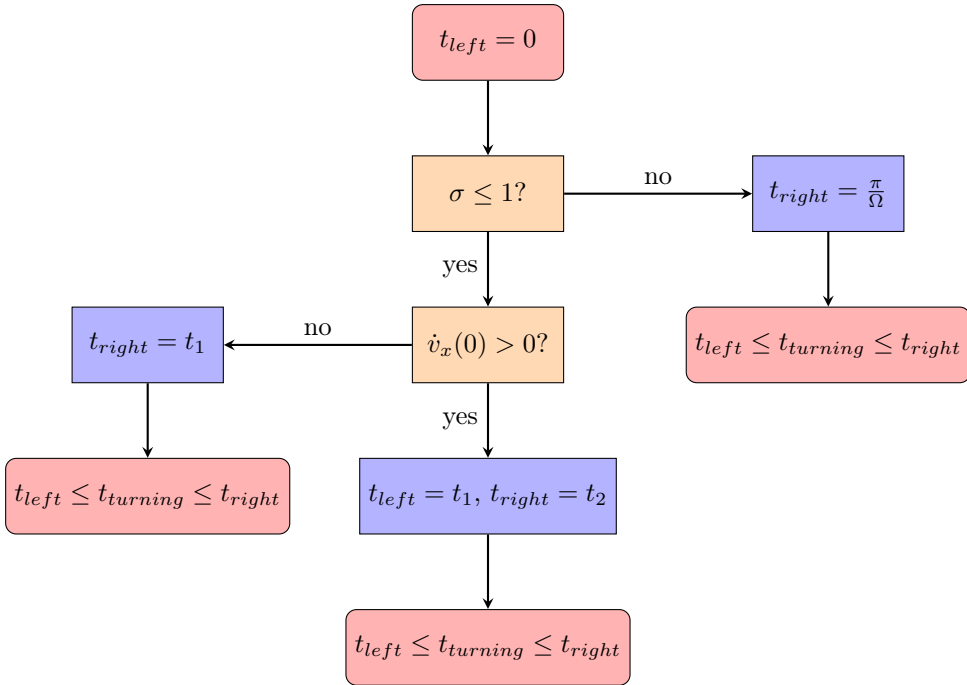


Figure 3.14: Decision flow chart of finding t_{left} and t_{right} for particles with $v_x(0) > 0$.

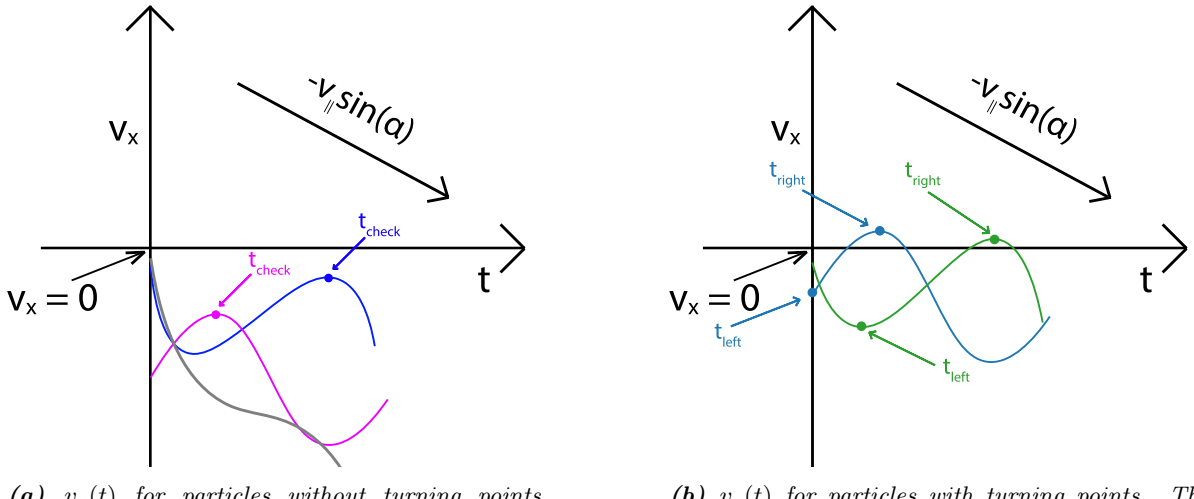
This is solved by

$$\begin{aligned} t_- &= -\frac{1}{\Omega} \left[\arcsin \left(\pm \frac{\sin(\alpha) \tan(\alpha)}{B\kappa \sqrt{A_1^2 + A_2^2}} \right) + \arctan \left(\frac{A_1}{A_2} \right) - \pi \right] + m2\pi \\ t_+ &= \frac{1}{\Omega} \left[\arcsin \left(\pm \frac{\sin(\alpha) \tan(\alpha)}{B\kappa \sqrt{A_1^2 + A_2^2}} \right) - \arctan \left(\frac{A_1}{A_2} \right) \right] + m2\pi, \end{aligned} \quad (3.57)$$

with $m \in \mathbb{Z}$. A solvability condition for this equation is $\sigma = \left| \frac{\sin(\alpha) \tan(\alpha)}{B\kappa \sqrt{A_1^2 + A_2^2}} \right| \leq 1$. Note that this condition is only dependent on quantities that are constant in a grid cell. Thus if a particle has one point where $\dot{v}_x = 0$ it is projected to have an infinite number of them. It will of course leave the grid cell and at that point κ will change. But this analysis is only considering the trajectories inside the grid cell. Now it is more useful to take a look at the $v_x(t)$ curves for different particles. When a particle enters the grid cell it can have a positive or a negative velocity. it is useful to look at the two cases separately. First the positive velocity will be discussed.

Case 1: $v_x(0) > 0$

First, realise particles that will reach the wall must have $v_{||} > 0$. This implies for the $v_x(t)$ curve that the average velocity over one gyro-orbit must be negative i.e. $\langle v_x \rangle < 0$. Particles with $v_x(0) > 0$ will need to have $\langle v_x \rangle < 0$ after one gyro-period, and thus the particle needs to have a turning point within this gyro-period. For $v_x(0) > 0$, there are three types of possible trajectories, and they are depicted in Figure 3.13. Note that all trajectories have $\langle v_x \rangle < 0$. The orange curve does not have any turning points, meaning that $\sigma > 1$. For this curve, one can deduce that $t_{left} = 0$ and $t_{right} = \frac{\pi}{\Omega}$ because if it has a turning point for a time later than half a gyro-period, the curve would have $\langle v_x \rangle > 0$. The times t_{left} and t_{right} have also been indicated on the figure. The red and black curves have turning points. They are distinguished from each other by the value of $\dot{v}_x(0)$. Looking at the red curve first, it has $\dot{v}_x(0) < 0$, which means that v_x is going to be negative in at most half a gyro-period (otherwise $\langle v_x \rangle > 0$). To be more precise, the particle will have a turning point between $t = 0$ and the first time where $\dot{v}_x = 0$, which will be called t_1 . Thus for the red curve, $t_{left} = 0$ and $t_{right} = t_1$; as also indicated in the figure. Note that t_1 can be calculated from Equation 3.57. The black curve has $\dot{v}_x(0) > 0$, meaning that v_x is increasing in the beginning. There will be a time t_1 , where $\dot{v}_x = 0$ for the first time. After that the velocity will be decreasing, and there has to be a turning point between t_1 and the second time where



(a) $v_x(t)$ for particles without turning points. There is one curve (grey) that does not have times where $\dot{v}_x = 0$. The time t_{check} for both curves with times where $\dot{v}_x = 0$ are denoted.

(b) $v_x(t)$ for particles with turning points. The times t_{right} and t_{left} for both type of curves are denoted.

Figure 3.15: Type of Trajectories for $v_x(0) < 0$.

$\dot{v}_x = 0$, which will be called t_2 . Note that if there would not have been a turning point, the average v_x velocity would have been positive. This means that, as indicated in the figure, $t_{left} = t_1$ and $t_{right} = t_2$. Note that this makes it relatively simple to find t_{left} and t_{right} in the case of $v_x(0) > 0$. First check if $\sigma > 1$, if so, $t_{left} = 0$ and $t_{right} = \frac{\pi}{\Omega}$. If $\sigma \leq 1$, check if $\dot{v}_x > 0$, if that is the case $t_{left} = t_1$ and $t_{right} = t_2$, if not $t_{left} = 0$ and $t_{right} = t_1$. This algorithm is been illustrated in a decision flow chart in Figure 3.14.

Case 2: $v_x(0) < 0$

When $v_x(0) < 0$, there can be particles without turning points. That was not the case for particles with $v_x > 0$ because $\langle v_x \rangle < 0$, therefore, there had to be times in a gyro-period where $v_x < 0$. Particles without turning points are handled directly in the decision flow chart in Figure 3.12. The possible trajectories in $v_x(t)$ for particles without turning points are displayed in Figure 3.15a. The grey curve has $\sigma > 1$, $v_x(0) < 0$ and $\dot{v}_x(0) < 0$ thus there cannot be any turning points because there are no locations where $\dot{v}_x > 0$. The other possible curves are the purple and the blue curve. The difference between the blue and the purple curve is the value of $\dot{v}_x(0)$. If $\dot{v}_x(0) > 0$, it means that the maximum of the $v_x(t)$ curve will be at the first root of \dot{v}_x , which is called t_1 . If $v_x(t_1) < 0$ it means that $v_x(t) < 0$ for all $t > 0$. This, in turn, means that the particle does not have turning points in future times. For the blue curve, with $\dot{v}_x(0) < 0$, the maximum is at the second root of \dot{v}_x , which is called t_2 . So in this case if $v_x(t_2) < 0$ it means that $v_x(t) < 0$ for all $t > 0$, and thus there are no turning points in future times. Therefore for particles with $v_x(0) < 0$, one needs to check at a time t_{check} if $v(t_{check}) < 0$. If that is the case, the particle will not have turning points. If $v(t_{check}) > 0$, the particle will have turning points. For the case where $\dot{v}_x(0) < 0$, $t_{check} = t_2$ and for $\dot{v}_x > 0$, $t_{check} = t_1$. Note that the value of t_{check} for both curves is denoted in Figure 3.15a.

Curves for particles with turning points are displayed in Figure 3.15b. The two curves are distinguished by the value of $\dot{v}_x(0)$. The light blue curve has $\dot{v}_x(0) > 0$. It means that this turning point has to be between $t = 0$ and time at which the maximum value of $v_x(t)$ is reached, which is t_1 . Thus for the light blue particle $t_{left} = 0$ and $t_{right} = t_1$. The green curve has $\dot{v}_x(0) < 0$ and has a turning point. This turning point must be between the first root of $\dot{v}_x(t)$ and the second root of $\dot{v}_x(t)$. Therefore $t_{left} = t_1$ and $t_{right} = t_2$. Note that for both the light blue and the green curve, $v_x(t_{check}) > 0$. The decision flow chart to obtain t_{left} and t_{right} is given in Figure 3.16.

3.7.2.3 The final algorithm

Now the separate pieces of the algorithm have been discussed, here the final algorithm that combines everything will be given. The algorithm to find τ is given in pseudo-code in Algorithm 1. First note the

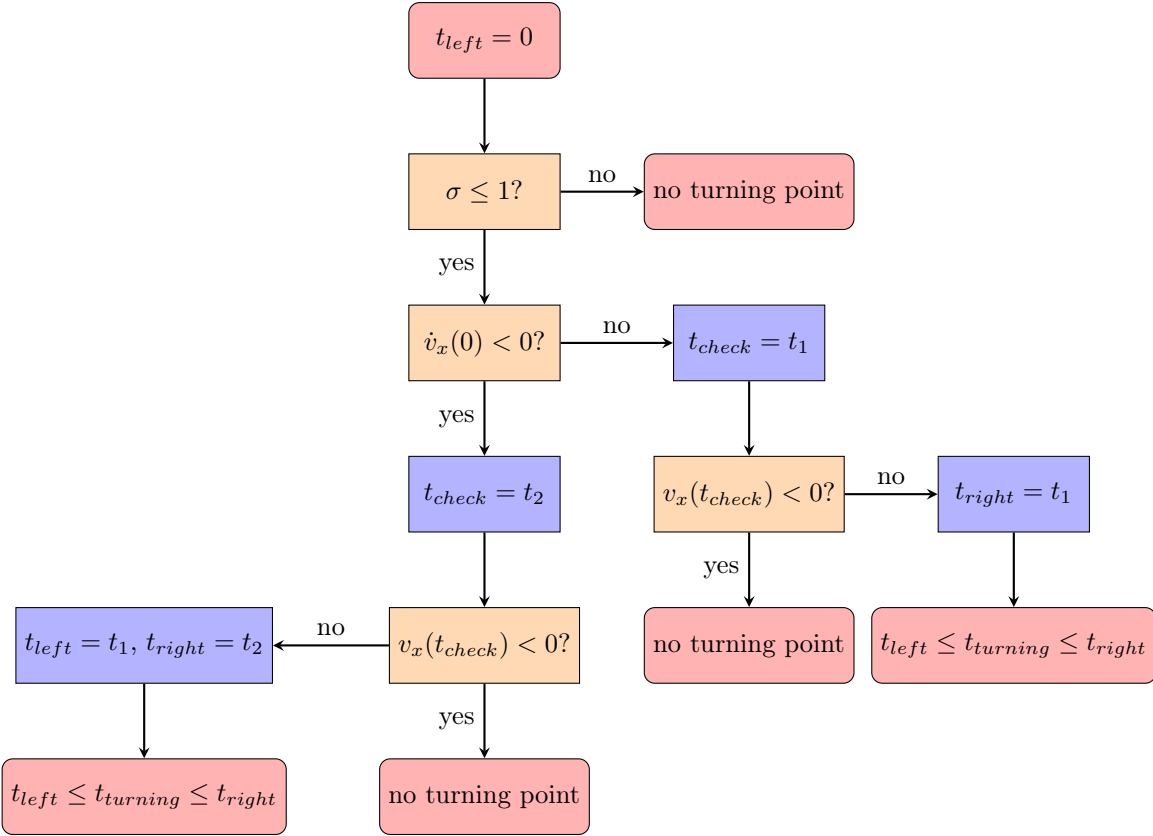


Figure 3.16: Decision flow chart of finding first if a particle has turning points and if so it finds t_{left} and t_{right} for particles with $v_x(0) < 0$.

first check that is done in Operation 1. This check is done to know if there are times where $\dot{v}_x = 0$. The particles that don't have those points will be treated differently. If at that point $v_x(0) > 0$, the particle will have its last turning point and the curve $v_x(t)$ is the orange one in Figure 3.13. In this case the turning points need to be found in ranges of the gyroperiod, as shown in the right branch of the decision flow chart in Figure 3.14. If $v_x(0) < 0$, the particle will not have a turning point anymore and τ can be found like in the right branch of the decision flow chart in Figure 3.12.

If there are times at which $\dot{v}_x = 0$, then the rest of the algorithm will be executed. It should be highlighted that in the code there are cases where $t_{left} = t_{right} = t_0$, this happens at Operation 20 and Operation 26. This is done to deal with the particles that do not have turning points, i.e. the blue and purple curve in Figure 3.15a. The rest of the algorithm is just a combination of the decision flow charts discussed earlier.

There are still some things that are important to discuss about this algorithm. The algorithm is recursive and that the algorithm will only repeat if Operation 42 is executed. This recursivity is coming from the backwards arrow in the decision flow chart of Figure 3.12. It should also be observed that Operations 3, 5, 7, 10, 31, 33, 36, 38, and 40 require a root finder. The root finder used is the Newton-Raphson method [41] because the derivative of the function that the root is supposed to be found of is actually known. However, an addition to the method has to be made. The method works by searching for a root of the function $f(x)$ in between a range, let's say $[x_{left}, x_{right}]$. It is based on the fact that if a guess for a root x_0 is "close" then $x_1 = x_0 - \frac{f(x_0)}{f'(x_0)}$ will be a better guess. So the root for the n -th iteration will be iteratively updated in the following way:

$$x_{n+1} = x_n - \frac{f(x_n)}{f'(x_n)}, \quad (3.58)$$

until a certain tolerance is reached.

This method converges very efficiently, but there are two obvious problems. There is no guarantee that $x_{n+1} \in [x_{left}, x_{right}]$ which is not good in this specific problem setting because there can be another

root outside of the initial range. The second problem is the existence of so called cycles. For example trying to find the root of the function $f(x) = x^3 - 2x + 2$ will give cycles. This is because if you land on $x = 0$ (or close to it). Then the next update will send the root finder to $x = 1$, which will send it back to $x = 0$, and so on. This yields a 2-cycle. In the case of the trajectories the cycles can occur when $\frac{x(t')}{v_x(t')} = -\frac{x(t'')}{v_x(t'')}$ for some times t' and t'' . It has been proven that the cycling behavior only occurs at boundary points of the convergence interval [42]. This leads to some conditions for convergence:

1. The function $f(x)$ is smooth
2. The guess was reasonably good i.e. inside the convergence interval
3. There are no extrema of the function $f(x)$ in between $[x_{left}, x_{right}]$

Condition 1. is satisfied since the particle trajectories are smooth functions, and 3. is ensured to be satisfied by the algorithm. However, 2. definitely is not. There can be particles with $\lambda < \alpha$ that have $f'(x)$ close to zero, and they will give a problem in Equation 3.58 by jumping outside the bounds. Jumping outside the bounds is solved by stating that if $x_{n+1} > x_{right}$ then $x_{n+1} = \frac{x_n + x_{right}}{2}$ and if $x_{n+1} < x_{left}$ then $x_{n+1} = \frac{x_n + x_{left}}{2}$.

Lastly, the cycles are only observed in this problem if x_{left} and x_{right} are very far apart. For the algorithm, this happens when there are no turning points. Because in that case, there is no immediate upper bound on the value of τ . To make sure that t_a and t_b are not too far apart the recursive step on the right of the decision chart in Figure 3.12 is used. One increases t_b with steps of $\frac{\pi}{\Omega}$ until a point is found where $x(t_b) < x_1$, remember that particles can only go out of the grid cell in x_1 because $\langle v_x \rangle < 0$. If that point is found, one can search for τ between t_a and t_b , which is a range of half a gyro-period. This ensures that the cycles do not occur. Using this root finder in combination with the piece-wise analytical trajectories will make the code around $30\times$ faster.

Algorithm 1 Calculate crossing times τ

```

1: if  $\left| \frac{\sin(\alpha) \tan(\alpha)}{B\kappa\sqrt{A_1^2+A_2^2}} \right| > 1$  then
2:   if  $v_x(0) > 0$  then
3:     find  $t_{turning}$  based on gyro period
4:     if  $x(t_{turning}) > x_0$  then
5:       find  $\tau$  for which  $x(\tau) = x_0$  knowing that  $\tau \in [0, t_{turning}]$ 
6:     else  $\{x(t_{turning}) < x_0\}$ 
7:       find  $\tau$  for which  $x(\tau) = x_1$  knowing that  $\tau \in [t_{turning}, \infty]$ 
8:     end if
9:   else  $\{v_x(0) < 0\}$ 
10:    find  $\tau$  for which  $x(\tau) = x_1$  knowing that  $\tau \in [0, \infty)$ 
11:  end if
12: else  $\left\{ \frac{\sin(\alpha) \tan(\alpha)}{B\kappa\sqrt{A_1^2+A_2^2}} \leq 1 \right\}$ 
13:    $t_a = 0$ 
14:   repeat
15:     find  $t_1$  and  $t_2$  analytically
16:     if  $\frac{\dot{v}_x(t_a)}{v_x(t_a)} < 0$  then
17:       if  $\frac{v_x(t_a)}{v_x(t_1)} < 0$  then
18:          $t_{left} = t_a$  and  $t_{right} = t_1$ 
19:       else  $\{ \frac{v_x(t_a)}{v_x(t_1)} > 0 \}$ 
20:          $t_{left} = t_{right} = t_a$ 
21:       end if
22:     else  $\{ \frac{\dot{v}_x(t_a)}{v_x(t_a)} > 0 \}$ 
23:       if  $\frac{v_x(t_2)}{v_x(t_1)} < 0$  then
24:          $t_{left} = t_1$  and  $t_{right} = t_2$ .
25:       else  $\{ \frac{v_x(t_2)}{v_x(t_1)} > 0 \}$ 
26:          $t_{left} = t_{right} = t_a$ 
27:       end if
28:     end if
29:     if  $t_{left} = t_{right}$  then
30:       if  $v_x(t_a) > 0$  then
31:         find  $\tau$  such that  $x(\tau) = x_0$  with  $\tau \in [t_a, \infty)$  (this shouldn't be allowed)
32:       else  $\{v_x(t_a) < 0\}$ 
33:         find  $\tau$  such that  $x(\tau) = x_1$  with  $\tau \in [t_a, \infty]$ 
34:       end if
35:     else  $\{t_{left} \neq t_{right}\}$ 
36:       find  $t_{turning}$  knowing that  $t_{turning} \in [t_{left}, t_{right}]$ 
37:       if  $x(t_{turning}) > x_0$  then
38:         find  $\tau$  such that  $x(\tau) = x_0$  with  $\tau \in [t_a, t_{turning}]$ 
39:       else if  $x(t_{turning}) < x_1$  then
40:         find  $\tau$  such that  $x(\tau) = x_1$  with  $\tau \in [t_a, t_{turning}]$ 
41:       else  $\{x_1 > x(t_{turning}) > x_0\}$ 
42:          $t_a = t_{turning}$ 
43:       end if
44:     end if
45:   until  $\tau$  is found such that  $x(\tau) = x_0$  or  $x(\tau) = x_1$ 
46: end if

```

4 Results and discussion

In this section, the results will be displayed and discussed. The results are split into three sections. First there will be a section on purely analytical results: Section 4.1. In that section, two main results will be proven. One result is that the potential close to the wall scale like $\phi(x) \sim \sqrt{x}$ for all magnetic field angles α . This is a generalisation of the result by Geraldini [7]. Second, a proof will be given that for a quasi-neutral plasma to exist in the magnetic presheath the plasma must marginally satisfy the Bohm condition at the Debye sheath entrance for all magnetic field angles α . This is again a generalisation of the result by Geraldini [7].

The other two sections will be about the results obtained from simulations with the novel numerical method discussed in Section 3. In Section 4.2 the results for simulations of the scale-separated magnetic presheath will be shown. The simulation results for small magnetic field angles α of both the self-consistent potential field and the distribution functions are consistent with the ones obtained by Geraldini [14]. It is shown that for larger magnetic field angles, the small angle code starts to deviate: it consistently overestimates the potential drop. For angles $\alpha \approx 0.1$ rad the solutions start to deviate considerably. Section 4.3 will present the results of simulations for the entire magnetised sheath. It is demonstrated that for all angles α , a self-consistent potential field was obtained that satisfies Poisson's equation. The self-consistent potential field profiles are consistent with the ones obtained in literature [12, 43]. All simulations give a quasi-neutral magnetic presheath followed by a charged Debye sheath. It is then discussed how for small fractions $\frac{\lambda_D}{\rho_i}$ the solution for the potential profile, as well as the marginalised distribution function, approaches the one of the magnetic presheath. Finally, results for the distribution functions hitting the target are displayed. These results are similar to the ones obtained in various literature [44, 45, 46].

4.1 Shape of potential close to the wall and Bohm condition

The goal of this section is to analytically find the shape of the potential in the magnetic presheath close to the wall and proof the Bohm condition on the magnetic presheath length scale. Restating the equations of motion in the magnetic presheath as given in Equation 2.40:

$$\dot{x} = v_x, \quad (4.1)$$

$$\dot{v}_x = -\frac{\Omega}{B} \frac{d\phi}{dx} + \Omega v_y \cos(\alpha), \quad (4.2)$$

$$\dot{v}_y = -\Omega v_x \cos(\alpha) - \Omega v_z \sin(\alpha), \quad (4.3)$$

$$\dot{v}_z = \Omega v_y \sin(\alpha). \quad (4.4)$$

A particle at position $\delta x \ll 1$ is considered. Thus the particle is close to the wall. The particle is at time t' and will hit the wall in a time $\Delta t \ll \frac{2\pi}{\Omega}$, it then makes sense to expand Equation 4.1 in $\delta t \leq \Delta t \ll \frac{2\pi}{\Omega}$. For the trajectory $x(t)$ the following expansion is obtained:

$$x(t' + \delta t) \simeq \delta x + v_x(t') (\delta t) + \frac{1}{2} \frac{dv_x}{dt} \Big|_{t=t'} (\delta t)^2 + \frac{1}{6} \frac{d^2 v_x}{dt^2} \Big|_{t=t'} (\delta t)^3 + \mathcal{O}(\delta t^4). \quad (4.5)$$

Using the equations of motion and keeping at most second order terms, one obtains:

$$x(t' + \delta t) \simeq \delta x + v_x(t') (\delta t) + \frac{1}{2} \left[-\frac{\Omega}{B} \frac{d\phi}{dx} \Big|_{x=\delta x} + \Omega v_y(t') \cos(\alpha) \right] (\delta t)^2 + \mathcal{O}(\delta t^3). \quad (4.6)$$

This shows that variations in v_y for $x(t)$ only are important from third order on in δt . Similarly for v_z variations only come into the equation for $x(t)$ only in the fourth order terms in δt . So if the particle is close enough to the wall, it can be assumed that v_y and v_z are constant.

With this, it becomes possible to solve the equation for v_x analytically as a function of x . For that, assume that initially, the particle is at position δx . Starting with Equation 4.2:

$$\frac{dv_x}{dt} = v_x \frac{dv_x}{dx} = \frac{1}{2} \frac{dv_x^2}{dx} = -\frac{\Omega}{B} \frac{d\phi}{dx} + \Omega v_y \cos(\alpha). \quad (4.7)$$

Using the fact that v_y is approximately constant approaching the wall, one can directly integrate this equation:

$$v_x^2(x) - v_x^2(\delta x) = 2 \frac{\Omega}{B} (\phi(\delta x) - \phi(x)) + 2\Omega v_y \cos(\alpha) (x - \delta x). \quad (4.8)$$

Here $x < \delta x$ is closer to the wall than δx . Note that the potential difference increases v_x because $\phi(x) < \phi(\delta x)$ and the magnetic force either slows down the particle or accelerates it dependent on v_y at δx . In particular, if v_y at δx is positive, the magnetic force is counteracting electric force. If v_y is negative, the magnetic force is in the same direction as the electric force. Note that particles entering the small region close to the wall will have $v_x < 0$.

So $v_x(x)$ is given by:

$$v_x(x) = -\sqrt{v_x^2(\delta x) + 2 \frac{\Omega}{B} (\phi(\delta x) - \phi(x)) + 2\Omega v_y \cos(\alpha) (x - \delta x)} \quad (4.9)$$

Note that the term $2 \frac{\Omega}{B} (\phi(\delta x) - \phi(x)) + 2\Omega v_y \cos(\alpha) (x - \delta x)$ has a similar influence on the particle trajectory as the effective potential in Equation 2.50. Thus one can define the effective potential close to the wall as

$$\chi(x) := 2 \frac{\Omega}{B} \phi(x) - 2\Omega v_y \cos(\alpha) x. \quad (4.10)$$

If a particle will hit the wall and has a velocity v_x at position x , its velocity at the wall is given by $v_{x,0} = -\sqrt{v_x^2 + \chi(x) - \chi(0)}$. A particle will only hit the wall if there does not exist a location x' in between 0 and x such that $v_x^2 + \chi(x) - \chi(x') < 0$. It is useful to refer to Figure 2.2: note that a particle will hit the wall if it can overcome the maximum effective potential that happens at location x_M . So a particle with velocity v_x at location x will not hit the wall if $\chi(x_M) - \chi(x) > v_x^2$.

Now all the groundwork for analytically investigating the potential close to the wall is laid out. We assume a position $x \ll \rho_i$ such that v_y and v_z are constant to respectively second and third order in Δt in the subsequent trajectory to the wall. The ion density is given by:

$$n_i(x) = n_{i,op}(x) + n_{i,cl}(x) = \int [f_{i,op}(x, v_x, v_y, v_z) + f_{i,cl}(x, v_x, v_y, v_z)] d^3 \mathbf{v}. \quad (4.11)$$

Here $n_{i,op}(x)$ and $n_{i,cl}(x)$ are the open and closed orbit ion densities, and $f_{i,op}(x, v_x, v_y, v_z)$ and $f_{i,cl}(x, v_x, v_y, v_z)$ are the open and closed orbit ion distribution functions. The closed orbits are characterised by turning points at some position $x_b \in [0, x]$, with $x \ll \rho_i$, such that $v_x(x_b) = 0$. Hence, $n_{i,cl}(0) = 0$. So x_b can be determined by:

$$v_x^2(x) + \frac{2\Omega}{B} (\phi(x) - \phi(x_b)) + 2\Omega v_y \cos(\alpha) (x_b - x) = 0. \quad (4.12)$$

Note also that following the trajectories $f_{i,cl}(x, v_x, v_y, v_z) = f_{i,cl}(x_b, 0, v_y, v_z)$ where v_y and v_z are approximately constant. Note also that $f_{i,cl}(x, v_x, v_y, v_z) = f_{i,cl}(x, -v_x, v_y, v_z)$, as each closed orbit particle has a backward-going copy.

It is convenient to define the change in potential $\frac{e\delta\phi}{T_e} = \frac{e}{T_e} (\phi(x) - \phi_0) \ll 1$, where $\phi_0 := \phi(0)$. The leading-order electron density at $x = 0$ is $n_{e,0} = n_{e,\infty} e^{\frac{e\phi_0}{T_e}}$. Then the electron density near $x = 0$ is given by:

$$n_e(x) = n_{e,0} e^{\frac{e\delta\phi}{T_e}}. \quad (4.13)$$

The expanded quasi-neutrality equation near $x = 0$ is given by:

$$n_{e,0} e^{\frac{e\delta\phi}{T_e}} - n_{e,0} = Z (n_{i,cl}(x) + n_{i,op}(x) - n_{i,op}(0)). \quad (4.14)$$

Expanding the electron density in small $\delta\phi$ gives:

$$n_{e,0} e^{\frac{e\delta\phi}{T_e}} - n_{e,0} = n_{e,0} \frac{e\delta\phi}{T_e} + \frac{n_{e,0}}{2} \left(\frac{e\delta\phi}{T_e} \right)^2 + \mathcal{O}(\delta\phi^3). \quad (4.15)$$

It is also desirable to expand the ion density in small $\delta\phi$.

We look at the open orbit ion density first:

$$n_{i,op}(x) = \int f_{i,op}(x, v_x, v_y, v_z) d^3v = \int f_{0,i,op}(v_{x,0}, v_{y,0}, v_{z,0}) dv_x dv_y dv_z, \quad (4.16)$$

where $f_{0,i,op}$ is the open orbit distribution function at $x = 0$. Particles in an open orbit will all hit the wall. Given a velocity at position $x \ll \rho_i$ one can calculate $v_{x,0}$ by inserting $\delta x = x$ and $x = 0$ into Equation 4.9:

$$v_{x,0} = -\sqrt{v_x^2 + \frac{2\Omega}{B}\delta\phi - 2\Omega v_y \cos(\alpha)x}. \quad (4.17)$$

Now we use that v_y and v_z are approximately constant and changing variables in Equation 4.16 from \mathbf{v} to \mathbf{v}_0 :

$$n_{i,op}(x) = - \int dv_{z,0} \int dv_{y,0} \int_{-\infty}^{\infty} \frac{v_{x,0}}{\sqrt{v_{x,0}^2 - \frac{2\Omega}{B}\delta\phi + 2\Omega v_{y,0} \cos(\alpha)x}} f_{0,i,op}(v_{x,0}, v_{y,0}, v_{z,0}) dv_{x,0}. \quad (4.18)$$

Here, Equation 4.17 was used to calculate the Jacobian. This equation can be integrated by parts:

$$\begin{aligned} n_{i,op}(x) &= - \int dv_{z,0} \int dv_{y,0} \left[f_{0,i,op}(v_{x,0}, v_{y,0}, v_{z,0}) \sqrt{v_{x,0}^2 - \frac{2\Omega}{B}\delta\phi + 2\Omega v_{y,0} \cos(\alpha)x} \right]_{-\infty}^{\infty} \\ &\quad + \int dv_{z,0} \int dv_{y,0} \left[\int_{-\infty}^{\infty} \frac{\partial f_{0,i,op}}{\partial v_{x,0}} \sqrt{v_{x,0}^2 - \frac{2\Omega}{B}\delta\phi + 2\Omega v_{y,0} \cos(\alpha)x} dv_{x,0} \right]. \end{aligned} \quad (4.19)$$

Note that $f_{0,i,op}(v_{x,0}, v_{y,0}, v_{z,0})$ is discontinuous in $v_{x,0}$ because there will be some maximum negative velocity $v_{x,0,max}(v_{y,0}, v_{z,0}) < 0$ particles can reach given $v_{y,0}$ and $v_{z,0}$. There will also be $v_{x,0,min}$. At $v_{x,0} > 0$ and $v_{x,0} < v_{x,0,max}(v_{y,0}, v_{z,0})$ the distribution function is zero. At the point where $v_{x,0} = v_{x,0,min}$ and $v_{x,0} = v_{x,0,max}(v_{y,0}, v_{z,0})$ the distribution function jumps from zero to $f_{0,i,op}(v_{x,0,min}, v_{y,0}, v_{z,0})$ and $f_{0,i,op}(v_{x,0,max}, v_{y,0}, v_{z,0})$, respectively. In between these boundaries the function is continuous, because the incoming distribution function at infinity is continuous. This means that inserting the boundary points gives:

$$n_{i,op}(x) = \int dv_{z,0} \int dv_{y,0} \left[\int_{-\infty}^{\infty} \frac{\partial f_{0,i,op}}{\partial v_{x,0}} \sqrt{v_{x,0}^2 - \frac{2\Omega}{B}\delta\phi + 2\Omega v_{y,0} \cos(\alpha)x} dv_{x,0} \right]. \quad (4.20)$$

Again one has to realise that $f_{0,i,op}$ discontinuously jumps from $v_{x,0,min}$ to $f_{0,i,op}(v_{x,0,min}, v_{y,0}, v_{z,0})$ and $f_{0,i,op}(v_{x,0,max}, v_{y,0}, v_{z,0})$ for $v_{x,0} = v_{x,0,min}$ and $v_{x,0} = v_{x,0,max}(v_{y,0}, v_{z,0})$, respectively. This means that $\frac{\partial f_{0,i,op}}{\partial v_{x,0}}$ is a sum of a continuous part and two Dirac δ functions:

$$\begin{aligned} \frac{\partial f_{0,i,op}}{\partial v_{x,0}} &= -f_{0,i,op}(v_{x,0,min}, v_{y,0}, v_{z,0}) \delta(v_x - v_{x,0,min}) \\ &\quad + f_{0,i,op}(v_{x,0,max}, v_{y,0}, v_{z,0}) \delta(v_x - v_{x,0,max}) + \frac{\partial f_{0,i,op}}{\partial v_{x,0}}, \end{aligned} \quad (4.21)$$

where it must be noted that the last term on the right-hand side is only a derivative in the continuous region of $f_{0,i,op}$. One can now make some progress in evaluating Equation 4.20:

$$\begin{aligned} n_{i,op}(x) &= \int dv_{z,0} \int dv_{y,0} f_{0,i,op}(v_{x,0,max}, v_{y,0}, v_{z,0}) \sqrt{v_{x,0,max}^2 + \delta\chi} \\ &\quad - \int dv_{z,0} \int dv_{y,0} f_{0,i,op}(0, v_{y,0}, v_{z,0}) \sqrt{v_{x,0,min}^2 + \delta\chi} \\ &\quad - \int dv_{z,0} \int dv_{y,0} \left[\int_0^{v_{x,0,max}} \frac{\partial f_{0,i,op}}{\partial v_{x,0}} \sqrt{v_{x,0}^2 - \frac{2\Omega}{B}\delta\phi + 2\Omega v_{y,0} \cos(\alpha)x} dv_{x,0} \right], \end{aligned} \quad (4.22)$$

where $\delta\chi$ was conveniently defined as the change in effective potential $\delta\chi = -\frac{2\Omega}{B}\delta\phi + 2\Omega v_{y,0} \cos(\alpha)x$ and it should be noted that the last term on the RHS now is an integral only over the continuous part of $f_{0,i,op}$. Lastly, note that the integration boundaries have been swapped ($v_{x,0,max} < 0$). To find how the density scales as a function of x for small x one has to look at how the equation scales in $\delta\chi$ because

$\delta\chi \rightarrow 0$ when $x \rightarrow 0$. The first term is taylor expandable. The second term on the RHS scales with $\sqrt{\delta\chi}$ when $v_{x,0,min} = 0$. This means that the second term on the RHS is bounded from above by a term that scales with $\sqrt{\delta\chi}$ in small $\delta\chi$, which happens when $v_{x,0,min} = 0$. This term dominates the scaling in small $\delta\chi$ of the second and first term on the RHS. It turns out that the third term scales with $\delta\chi^a$ with $a > \frac{1}{2}$. To see this one has to notice that $\frac{\partial f_{0,i,op}}{\partial v_{x,0}}$ will be a smooth infinite differentiable function in the region where $f_{0,i,op}$ is continuous. This is because $f_{i,\infty}$ is smooth and infinite differentiable, and it is conserved along particle trajectories. This means that $f_{0,i,op}(\mathbf{v}_0) = f_{i,\infty}(\mathbf{v}_\infty(\mathbf{v}_0))$, implying that integrating $\sqrt{v_{x,0}^2 - \frac{2\Omega}{B}\delta\phi + 2\Omega v_{y,0} \cos(\alpha)x}$ will give a lower bound on the order of $\delta\chi$ that the integral depends on. One finds:

$$\int_0^{v_{x,0,max}} \sqrt{v_{x,0}^2 + \delta\chi} dv_{x,0} = \frac{\delta\chi \operatorname{arcsinh}\left(\frac{v_{x,0,max}}{\sqrt{\delta\chi}}\right) + v_{x,0,max} \sqrt{v_{x,0,max} + \delta\chi}}{2}. \quad (4.23)$$

Note that $\operatorname{arcsinh}\left(\frac{v_{x,0,max}}{\sqrt{\delta\chi}}\right)$ scales like $\log(\delta\chi^{-1/2})$ when $\delta\chi \rightarrow 0$. The resulting term scaling like $\delta\chi \log(\delta\chi^{-1/2})$ is subdominant compared with the $\sqrt{\delta\chi}$ scaling of the second term on the RHS of Equation 4.22. The second term in Equation 4.23 will have a Taylor expansion and will have a term that scales with $\delta\chi$ as the lowest order. The first term in Equation 4.22 will also have an existing Taylor expansion which scales with $\delta\chi$ in leading order. And thus Equation 4.22 has a leading term in small $\delta\chi$ that scales with $\sqrt{\delta\chi}$.

Now going to the closed orbit density:

$$n_{i,cl}(x) = \int d^3\mathbf{v} f_{i,cl}(x, v_x, v_y, v_z) \quad (4.24)$$

We note that following the particle trajectory it will reach a point $x_b < x$ where $v_x = 0$, so:

$$n_{i,cl}(x) = \int d^3\mathbf{v} f_{i,cl}(x_b(v_x), 0, v_y, v_z). \quad (4.25)$$

A particle that is about to turn will continuously slow down towards the wall, this means that the closer a particle will turn to the wall the higher its velocity was at the initial location x . Therefore, the maximum velocity a particle will have at location x is the velocity that will make the particle turn at the wall. It will then have a velocity such that $v_{x,0} = 0$ in Equation 4.17, thus $v_{x,max} = \sqrt{-\frac{2\Omega}{B}\delta\phi + 2\Omega v_y \cos(\alpha)x}$ for the particle after it has turned back and $v_{x,min} = -\sqrt{-\frac{2\Omega}{B}\delta\phi + 2\Omega v_y \cos(\alpha)x}$ moving towards the wall. So the closed ion density is given by:

$$n_{i,cl}(x) = \int dv_z \int dv_y \int_{-\sqrt{-\frac{2\Omega}{B}\delta\phi + 2\Omega v_y \cos(\alpha)x}}^{\sqrt{-\frac{2\Omega}{B}\delta\phi + 2\Omega v_y \cos(\alpha)x}} f_{i,cl}(x_b(v_x), 0, v_y, v_z) dv_x \quad (4.26)$$

It is more convenient to write this integral as an integral over x_b . As stated before, during the process of the velocity going from $v_{x,min}$ to $v_{x,max}$, the locations between x_b and x will be crossed twice. To see this note that v_x in Equation 4.12 has two possible values for one x_b . Using the Jacobian the following equation is obtained:

$$n_{i,cl}(x) = -2 \int dv_z \int dv_y \int_0^x \frac{\frac{2\Omega}{B}\phi'(x_b) - 2\Omega v_y \cos(\alpha)}{\sqrt{\frac{2\Omega}{B}(\phi(x_b) - \phi(x)) + 2\Omega v_y \cos(\alpha)(x - x_b)}} f_{i,cl}(x_b, 0, v_y, v_z) dx_b. \quad (4.27)$$

Note that again here the distribution function is not continuous at the boundary points. With the same reasoning one can integrate by parts:

$$\begin{aligned} n_{i,cl}(x) &= -2 \int dv_z \int dv_y \left[\sqrt{\frac{2\Omega}{B}(\phi(x_b) - \phi(x)) + 2\Omega v_y \cos(\alpha)(x - x_b)} f_{i,cl}(x_b, 0, v_y, v_z) \right]_0^x + \\ &\quad 2 \int dv_z \int dv_y \int_0^x \sqrt{\frac{2\Omega}{B}(\phi(x_b) - \phi(x)) + 2\Omega v_y \cos(\alpha)(x - x_b)} \frac{\partial f_{i,cl}}{\partial x_b} dx_b \\ &= 2 \int dv_z \int dv_y \sqrt{-\frac{2\Omega}{B}\delta\phi + 2\Omega v_y \cos(\alpha)x} f_{i,cl}(0, 0, v_y, v_z) + \\ &\quad 2 \int dv_z \int dv_y \int_0^x \sqrt{\frac{2\Omega}{B}(\phi(x_b) - \phi(x)) + 2\Omega v_y \cos(\alpha)(x - x_b)} \frac{\partial f_{i,cl}}{\partial x_b} dx_b. \end{aligned} \quad (4.28)$$

Note that the second term on the RHS is not integrating the boundary points such that $\frac{\partial f_{i,cl}}{\partial x_b}$ does not contain Dirac δ functions. To find how this equation scales in $\delta\chi$ in lowest order one again has to analyse the second term on the RHS. Note that it can be written as an integral over v_x instead of x_b :

$$\begin{aligned} 2 \int dv_z \int dv_y \int_0^x \sqrt{\frac{2\Omega}{B} (\phi(x_b) - \phi(x)) + 2\Omega v_y \cos(\alpha) (x - x_b)} \frac{\partial f_{i,cl}}{\partial x_b} dx_b = \\ - \int dv_z \int dv_y \int_{-\sqrt{-\frac{2\Omega}{B} \delta\phi + 2\Omega v_y \cos(\alpha)x}}^{\sqrt{-\frac{2\Omega}{B} \delta\phi + 2\Omega v_y \cos(\alpha)x}} v_x \frac{\partial f_{i,cl}}{\partial v_x} dv_x \end{aligned} \quad (4.29)$$

Now note that $f_{i,cl}$ must be an even function to lowest order in the expansion in $\delta\phi$ because the two particles at (x, v_x) and $(x, -v_x)$ are the same, just at different points of their orbit. If $f_{i,cl}$ is even in v_x then $\frac{\partial f_{i,cl}}{\partial v_x}$ is odd. This means that to lowest order in $\delta\chi$ the integral becomes:

$$\int dv_z \int dv_y \int_{-\sqrt{\delta\chi}}^{\sqrt{\delta\chi}} v_x \frac{\partial f_{i,cl}}{\partial v_x} dv_x \sim \int dv_z \int dv_y \int_{-\sqrt{\delta\chi}}^{\sqrt{\delta\chi}} v_x^2 dv_x \sim \delta\chi^{3/2} \quad (4.30)$$

This means that the first term on the RHS of Equation 4.28 is the leading order term, it scales with $\sqrt{\delta\chi}$.

Close to zero the following holds: $n_\infty e^{\frac{e\delta\phi}{T_e}} = n_\infty \left[1 + \frac{e}{T_e} \delta\phi + \frac{1}{2} \frac{e^2}{T_e^2} \delta\phi^2 + \mathcal{O}(\delta\phi^3) \right] = n_i(x)$. The largest variation in the electron density scales with $\delta\phi$ in the electron density is the linear term and this means that the ion density term that scales with $\sqrt{\delta\chi}$ has to disappear:

$$\left[2 \int dv_y \int dv_z f_{i,cl}(0, 0, v_y, v_z) - \int dv_{z,0} \int dv_{y,0} f_{0,i,op}(0, v_{y,0}, v_{z,0}) \right] \sqrt{\delta\chi} = 0. \quad (4.31)$$

Note that $f_{i,cl}(0, 0, v_y, v_z) = f_{0,i,op}(0, v_{y,0}, v_{z,0})$ because if a particle hits the wall with 0 velocity it is on the edge of being passing and closed. Hence, the distribution functions describe the same particles with the same initial conditions and thus they have to be equal. This gives:

$$\int dv_y \int dv_z f_{0,i,op}(0, v_y, v_z) \sqrt{\delta\chi} = 0. \quad (4.32)$$

Note that this integral describes the density of particles with $v_{x,0} = 0$. Because $f_{0,i,op}$ is strictly positive the condition implies that the integrand has to be zero. This means that there cannot be particles hitting the wall with 0 velocity. Note that Equation 4.17 gives $v_{x,0}$. If $v_{x,0} \neq 0$ it means that $\frac{2\Omega}{B} \delta\phi - 2\Omega v_y \cos(\alpha) x > -v_x^2$ for $x \rightarrow 0$. This can only be guaranteed if $\delta\phi$ scales with x in such a way that it is larger than x for small x . Thus $\delta\phi \sim x^a$ with $a < 1$. This means that $\phi'(0) \rightarrow \infty$. A diverging electric field means that close to the wall all ion orbits are open because the electric force becomes so strong that the magnetic force cannot compete. This implies that the closed ion orbit density is exponentially small i.e. $n_{i,cl}(x) \simeq 0$. To see this note that particles with a turning point very close to the wall need to have a location of the maximum of $\delta\chi$ close to the wall. Given $\delta\phi \sim x^a$, $\delta\chi = \frac{2\Omega}{B} \kappa x^a - 2\Omega v_y \cos(\alpha) x$ and it can be shown that:

$$x_M = \left(\frac{a\kappa}{v_y \cos(\alpha) B} \right)^{\frac{1}{1-a}}. \quad (4.33)$$

Note that for x_M to be small v_y has to become large. In particular $x_M \rightarrow 0$ when $v_y \rightarrow \infty$. Assuming the distribution function to exponentially decay at large energies, which is usually the case, there exist exponentially few particles with large v_y , and thus $f_{i,cl}(x_b, 0, v_y, v_z)$ goes exponentially to zero for smaller and smaller x_b . This in turn means that close to the wall $n_{i,cl} \simeq 0$.

Returning back to the equation for the open ion density Equation 4.18 one can now see that the integral is carried out from some $v_{x,0,min} > 0$ to $v_{x,0,max}$ where $v_{x,0,min}$ is the absolute value of some negative velocity:

$$n_{i,op}(x) = \int dv_{z,0} \int dv_{y,0} \int_{v_{x,0,min}}^{v_{x,0,max}} \frac{v_{x,0}}{\sqrt{v_{x,0}^2 - \frac{2\Omega}{B} \delta\phi + 2\Omega v_{y,0} \cos(\alpha)x}} f_{0,i,op}(v_{x,0}, v_{y,0}, v_{z,0}) dv_{x,0}. \quad (4.34)$$

Particles with low $v_{x,0}$ are also particles that surpassed a maximum in the effective potential very close to the wall. The same argument holds as in the closed orbit particle density close to the wall. Those

particles became passing at very small x . Thus they will have x_M close to zero. But as established before x_M scales with $\frac{1}{v_y}$. This implies that particles with low $v_{x,0}$ will have large v_y . There are exponentially few particles with high v_y , as well as exponentially few with low $v_{x,0}$. This means that it is justified to assume the density contribution from these particles to be negligible compared with the total density. It is thus justified to Taylor expand $\frac{v_{x,0}}{\sqrt{v_{x,0}^2 - \frac{2\Omega}{B}\delta\phi + 2\Omega v_{y,0} \cos(\alpha)x}}$ in small $\delta\chi$ to obtain:

$$n_{i,op}(x) = \int dv_{z,0} \int dv_{y,0} \int_{v_{x,0,min}}^{v_{x,0,max}} \left[\frac{v_{x,0}}{v_{x,0}} - \frac{v_{x,0}}{2v_{x,0}^3} \delta\chi + \frac{3v_{x,0}}{8v_{x,0}^5} \delta\chi^2 + \mathcal{O}(\delta\chi^3) \right] f_{0,i,op}(v_{x,0}, v_{y,0}, v_{z,0}) dv_{x,0}. \quad (4.35)$$

Note that the integral is from $v_{x,0,min} < 0$ to $v_{x,0,max} < 0$ with $|v_{x,0,max}| > |v_{x,0,min}|$. The first term represents $n_i(0)$. Continuing with the quasi-neutrality equation as in Equation 4.14 it is desirable to compare every order in $\delta\phi$. As argued before the open ion density is approximately equal to the total ion density, the leading term in the quasi-neutrality equation now is of order $\delta\phi$:

$$\begin{aligned} n_{e,0} \frac{e\delta\phi}{T_e} &= \frac{\Omega}{B} \delta\phi Z \int dv_{z,0} \int dv_{y,0} \int_{v_{x,0,min}}^{v_{x,0,max}} \frac{f_{0,i,op}(v_{x,0}, v_{y,0}, v_{z,0})}{v_{x,0}^2} dv_{x,0} \\ &\quad - \Omega Z x \int dv_{z,0} \int dv_{y,0} v_{y,0} \cos(\alpha) \int_{v_{x,0,min}}^{v_{x,0,max}} \frac{f_{0,i,op}(v_{x,0}, v_{y,0}, v_{z,0})}{v_{x,0}^2} dv_{x,0} \end{aligned} \quad (4.36)$$

One obtains then for $\delta\phi(x)$:

$$\delta\phi(x) = \frac{x}{q_1}, \quad (4.37)$$

with q_1 given by:

$$q_1 = \frac{\frac{ZT_e\Omega}{Be} \int dv_{z,0} \int dv_{y,0} \int_{v_{x,0,min}}^{v_{x,0,max}} \frac{f_{0,i,op}(v_{x,0}, v_{y,0}, v_{z,0})}{v_{x,0}^2} dv_{x,0} - n_{e,0}}{\frac{ZT_e}{e} \Omega x \int dv_{z,0} \int dv_{y,0} v_{y,0} \cos(\alpha) \int_{v_{x,0,min}}^{v_{x,0,max}} \frac{f_{0,i,op}(v_{x,0}, v_{y,0}, v_{z,0})}{v_{x,0}^2} dv_{x,0}}. \quad (4.38)$$

Note that Equation 4.37 implies that $\phi'(0) = \frac{1}{q_1}$, but as a result of Equation 4.32 $\phi'(0) \rightarrow \infty$. This means $q_1 = 0$, which implies that the numerator in Equation 4.38 has to go to zero:

$$Zv_B^2 \int dv_{z,0} \int dv_{y,0} \int_{v_{x,0,min}}^{v_{x,0,max}} \frac{f_{0,i,op}(v_{x,0}, v_{y,0}, v_{z,0})}{v_{x,0}^2} dv_{x,0} = n_{e,0}, \quad (4.39)$$

where the definition of the Bohm velocity was used. It is clear that this is identical to the marginally satisfying the kinetic Bohm condition Equation 2.54. So, this shows that if a plasma is quasi-neutral the plasma has to marginally satisfy the kinetic Bohm condition at the Debye sheath entrance on the magnetic presheath scale.

The first-order variation of the quasi-neutrality equation is now the one that scales with $\delta\phi^2$:

$$\begin{aligned} n_{e,0} \frac{1}{2} \frac{e^2 \delta\phi^2}{T_e^2} &= -\Omega Z x \int dv_{z,0} \int dv_{y,0} v_{y,0} \cos(\alpha) \int_{v_{x,0,min}}^{v_{x,0,max}} \frac{f_{0,i,op}(v_{x,0}, v_{y,0}, v_{z,0})}{v_{x,0}^2} dv_{x,0} \\ &\quad + \int dv_{z,0} \int dv_{y,0} \int_{v_{x,0,min}}^{v_{x,0,max}} \frac{3f_{0,i,op}(v_{x,0}, v_{y,0}, v_{z,0})}{8v_{x,0}^4} \delta\chi^2 dv_{x,0}. \end{aligned} \quad (4.40)$$

Note that only the lowest non-zero orders of the terms going with x and $\delta\phi$ are considered. This then gives:

$$\begin{aligned} n_{e,0} \frac{1}{2} \frac{e^2 \delta\phi^2}{T_e^2} &= -\Omega Z x \int dv_{z,0} \int dv_{y,0} v_{y,0} \cos(\alpha) \int_{v_{x,0,min}}^{v_{x,0,max}} \frac{f_{0,i,op}(v_{x,0}, v_{y,0}, v_{z,0})}{v_{x,0}^2} dv_{x,0} \\ &\quad + Z \frac{4\Omega^2}{B^2} \delta\phi^2 \int dv_{z,0} \int dv_{y,0} \int_{v_{x,0,min}}^{v_{x,0,max}} \frac{3f_{0,i,op}(v_{x,0}, v_{y,0}, v_{z,0})}{8v_{x,0}^4} dv_{x,0}. \end{aligned} \quad (4.41)$$

This gives:

$$\delta\phi(x) = q_{1/2}^{-\frac{1}{2}} \sqrt{x}, \quad (4.42)$$

with $q_{1/2}$ given by:

$$q_{1/2} = \frac{3Zv_B^4 \int dv_{z,0} \int dv_{y,0} \int_{v_{x,0,min}}^{v_{x,0,max}} \frac{f_{0,i,op}(v_{x,0}, v_{y,0}, v_{z,0})}{v_{x,0}^4} dv_{x,0} - n_{e,0}}{2\Omega Z \int dv_{z,0} \int dv_{y,0} v_{y,0} \cos(\alpha) \int_{v_{x,0,min}}^{v_{x,0,max}} \frac{f_{0,i,op}(v_{x,0}, v_{y,0}, v_{z,0})}{v_{x,0}^2} dv_{x,0}}. \quad (4.43)$$

This shows that the potential scales like \sqrt{x} close to the wall. This proof generalises the result that Geraldini obtained for small angles α as discussed in Section 2.6.2.3. It was also derived that a plasma must marginally satisfy the Bohm condition at the Debye sheath entrance as a condition for a quasi-neutral plasma near $x = 0$ in the magnetic presheath. This is again a generalisation of the result obtained by Geraldini for small angles α (see Section 2.6.2.3). Note that in Section 2.6.1, the Bohm condition (not necessarily in its marginal form) was obtained from fluid theory on the scale of the magnetic presheath. In Section 2.5 it was also shown that the Bohm condition must be satisfied (not necessarily in its marginal form) at the Debye sheath entrance both in kinetic and fluid form from the scale of the Debye sheath. The result in this section, therefore, adds to those results and this improves our understanding of the scale separated magnetic presheath and Debye sheath system.

The derivation is only valid for small x i.e. close to the wall. The derivation also is only valid when $\delta\phi \ll T_e/e$. To say something about the validity of the result, one has to realise that Equation 4.39 holds universally because it says something about the distribution function at the sheath entrance. It is independent on x as long as one can find an x such that $\delta\phi$ is sufficiently small, which is generally the case. The same holds for the Equation 4.42, the potential will always follow a \sqrt{x} dependence, for very small x . The location where this \sqrt{x} dependence starts to develop is dependent on the potential profile.

4.2 Magnetic presheath simulations

In this section, results of the numerical method are described. In particular, the results for the magnetic presheath are displayed and discussed. In the simulations $Z = 1$ and thus ions with charge 1 are considered. This means that at the quasi-neutral presheath entrance $n_{e,\infty} = n_{i,\infty} := n_\infty$. In the simulations for the magnetic presheath quadratic basis functions are used, as defined in Equation 3.16.

It is first useful to compare the results from the simulation to existing results. For that the semi-analytical model by Geraldini [14] is used. The model by Geraldini is only valid for small angles of the magnetic field with the wall α . In Figure 4.1 the results for the simulation of an angle of $\alpha = 1.8^\circ$ are displayed. In Figure 4.1a the self consistent potential field is displayed in blue. The self consistent potential field obtained by the small angle code of Geraldini is displayed in orange. The difference between the two potential fields is calculated by evaluating:

$$\frac{\sqrt{\int_0^{x_\infty} |\phi_{numerical}(x) - \phi_{small\ angle}(x)|^2 dx}}{\sqrt{\int_0^{x_\infty} |\phi_{numerical}(x)|^2 dx}} \times 100\%,$$

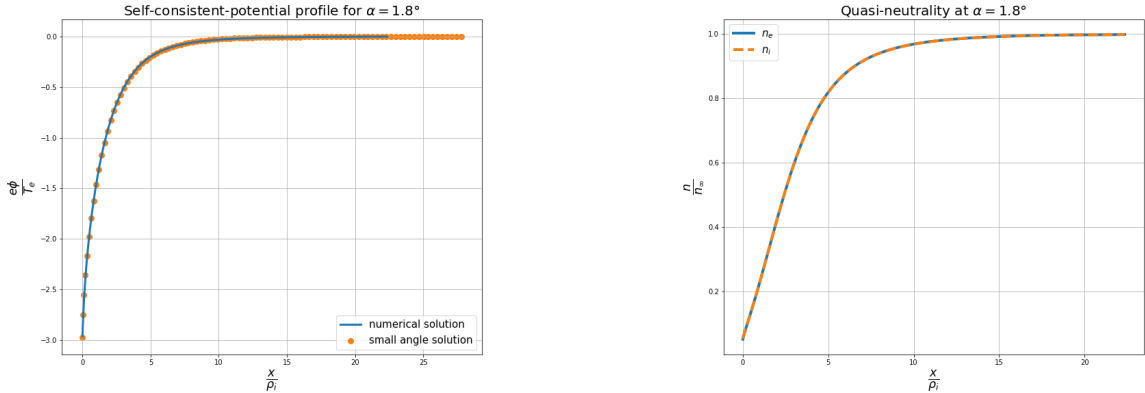
with $\phi_{numerical}(x)$ the potential obtained from the numerical method discussed in this report and $\phi_{small\ angle}(x)$ the solution obtained from the small angle code of Geraldini. This difference evaluates to 1.6%. Thus both quantitatively and qualitatively the two methods give almost the same result, implying that the numerical method works for small magnetic field angles α .

In Figure 4.1b the electron (blue) and ion densities (orange) for the self consistent potential are displayed. The error from quasi neutrality is calculated by evaluating:

$$E_{QN} = \sqrt{\frac{\int_0^{x_\infty} (n_e - n_i)^2 dx}{\int_0^{x_\infty} n_e^2 dx}} \times 100\%, \quad (4.44)$$

where E_{QN} stands for the error from quasi-neutrality and $n_e = n_\infty e^{\frac{e\phi}{T_e}}$. The error from the profiles shown in Figure 4.1b is 0.02%.

This comparison suggests that the numerical method correctly obtains the solution of the self-consistent potential field for small values of α . Motivated by this, the results for the magnetic presheath for different values of α will be displayed and discussed.



(a) The blue plot gives the self consistent potential obtained with the numerical method described in Section 3. The orange plot gives the solution obtained by the small angle code of Geraldini [14] with the same α .

(b) Electron and ion densities for the self consistent potential displayed in Figure 4.1a. The blue plot gives the electron density and the orange plot gives the ion density.

Figure 4.1: Simulation results for $\alpha = 1.8^\circ$. For the grid definition (Equation 3.50) $\delta = 0.3$ and $\kappa = 1.0$ were used. A weight w of 0.2 was used in the update of the potential (Section 3.5.1). For the sampling of velocity $m_{\lambda,1} = 10$, $m_{\lambda,2} = 20$, $m_{\theta,1} = 801$, $m_{\theta,2} = 101$, and $m_v = 10$. $v_{max} = 5v_{th}$ (Section 3.4). For the time integration: the time steps were chosen such that there are at least 10 time steps per grid cell.

In Figure 4.2 results for the simulations of the magnetic presheath are displayed. For all angles α $E_{QN} < 0.1\%$.

It can be seen that the potential drop increases when the angle α decreases. The size of the magnetic presheath that is characterised by the region where $\phi \neq 0$ also increases when the angle α decreases. To understand this, it is convenient to look at the density without an electric field: consider a gyroring about to hit the wall. The gyroring is oriented perpendicular to the magnetic field line, and thus it penetrates with a distance $\rho_i \cos(\alpha)$ in the x direction. Note that this means that the gyro-orbit starts to hit the wall when $x = \rho_i \cos(\alpha)$. Thus the density starts to drop further away from the wall for small α . The results for small magnetic field angle up to $\alpha = 10^\circ$ are comparable to the ones obtained in [14]. The density of the ions and thus the electrons are smaller for small angles.

Something needs to be noted about the profiles. The self-consistent potential profiles satisfy the requirement that the potential should scale with \sqrt{x} from the first grid cell. However, the profiles do not satisfy the expected \sqrt{x} dependence in the first grid cell. This cannot be seen in Figure 4.2 because it happens very close to the wall. It only becomes visible when plotting the profiles in \sqrt{x} . As discussed before, the finite element method cannot resolve the \sqrt{x} dependence close to $x = 0$. It is observed that the profile flattens in the first grid cell, just as shown in Figure 3.9. It happens only in the first grid cell, where $x = 0$ is included. This implies that making the grid finer close to the wall would make this problem less prominent. However, it is found that making the grid cell too small will cause numerical instabilities to occur. The potential drop in the grid cell becomes so small that a small numerical error can make the potential decrease (instead of increase) from the wall to the first grid point. If that happens, the profile becomes non-monotonic, and a potential well develops. Particles can get stuck in the potential well, and this breaks the iteration procedure. It means that the smallest possible stable first grid cell is related to the potential drop in the first grid cell. The potential drop is larger for more shallow magnetic field angles. Therefore, a larger grid spacing in x must be used for larger magnetic field angles α .

Another reason why the allowed grid spacing must depend on α is the fact that instabilities can occur if there are not enough particles with turning points in a specific grid cell, as discussed in Section 3.4. Note that for small angle α particles spend more time in the magnetic presheath because $v_{||}$ has almost no x component and v'_x is almost equal to v_x . Particles that spend more time in the magnetic presheath will also have more turning points. This means that for larger magnetic field angles α , the grid spacing or the resolution in velocity space must be increased.

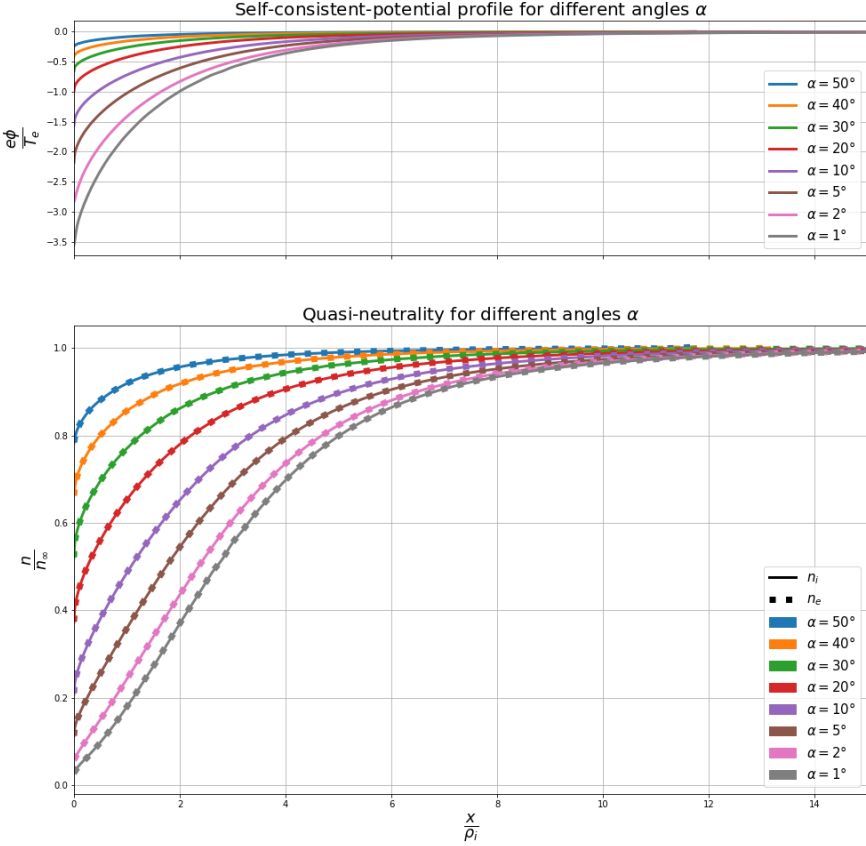


Figure 4.2: The results for self consistent-potential fields in the magnetic presheath for different magnetic field angles α is given on top. The results for ion and electron densities in the magnetic presheath for different angles α is given in the lower plot. The sampling of velocities in all the simulations were the same. For the sampling of velocity $m_{\lambda,1} = 20$, $m_{\lambda,2} = 20$, $m_{\theta,1} = 801$, $m_{\theta,2} = 101$, and $m_v = 10$. $v_{max} = 5v_{th}$ (Section 3.4). The x grid is different for each simulation: $\delta = 0.6$ for $\alpha = 50^\circ$, $\delta = 0.4$ for $\alpha = 40^\circ$ and $\delta = 0.3$ for all the other values of α . For the time integration: the time steps were chosen such that there are at least 10 time steps per grid cell.

It is also interesting to look at the distribution functions obtained for the self-consistent potential. This distribution function is obtained using a semi-lagrangian method [47, 48, 49]. This consists in integrating the particles backward in time towards the sheath entrance. This method is based on the fact that the distribution function is conserved along the particle trajectory. One can assign at any x , v_x , v_y , v_z , the value of $f_\infty(\mathbf{v}_\infty)$ that one obtains by integrating the particles at x backward to the sheath entrance. The distribution functions obtained at $x = 0$ (the wall or the Debye sheath entrance) can be seen in Figure 4.3. In this figure the marginalised distribution function $\int_{-\infty}^{\infty} \int_{-\infty}^{\infty} dv_{y,0} dv_{z,0} f_0(v_{x,0}, v_{y,0}, v_{z,0})$ is plotted, for several angles α . On this distribution function, several tests were performed. First, the distribution function integrated over velocity space should give the density at the wall as obtained in Figure 4.2. Second, the flux should be conserved:

$$\int d^3 \mathbf{v}_0 v_{x,0} f_0(\mathbf{v}_0) = \int d^3 \mathbf{v}_\infty v_{x,\infty} f_\infty(\mathbf{v}_\infty).$$

Lastly the kinetic Bohm condition was checked. In Table 1 it is shown that the Bohm condition is never exactly marginally satisfied, but the flux is conserved, and the density at $x = 0$ is as expected, in the table the yes means that the condition is satisfied with an error of less than 1%. Note that it is not trivial to marginally satisfy the Bohm condition, and it might not even be something expected

angle	Bohm condition satisfied	Flux conservation satisfied	density satisfied
1°	10% over satisfied	Yes	Yes
2°	15% over satisfied	Yes	Yes
5°	9% over satisfied	Yes	Yes
10°	6% over satisfied	Yes	Yes
20°	11% over satisfied	Yes	Yes
30°	14% over satisfied	Yes	Yes
40°	15% under satisfied	Yes	Yes
50°	116% under satisfied	Yes	Yes

Table 1: Conditions for the distribution functions plotted in Figure 4.3. the density condition and flux conservation conditions are basic conditions that need to be satisfied. The Bohm condition is a more non trivial condition. If **yes** is indicated it means that the condition is satisfied with < 1%.

from the numerical method. This is because, as proven in the previous section, the Bohm condition is paired with a singularity in the electric field. This singularity cannot be resolved with the numerical method as explained in Section 3.6. This singularity will accelerate the particles in the first grid cell. Because the singularity cannot be numerically resolved, it cannot be expected that the Bohm condition is satisfied.

Note also that since the integrand in the Bohm condition has a factor of $\frac{1}{v_x^2}$, the high energy tail of the distribution will not make a large difference. The Bohm condition is related to the steep falling-off of the distribution function at low v_x because those particles will contribute the most. So a small shift of the boundary where f_0 becomes 0 for small v_x has a lot of impact on the value of the Bohm condition. This all makes marginally satisfying the Bohm condition non-trivial.

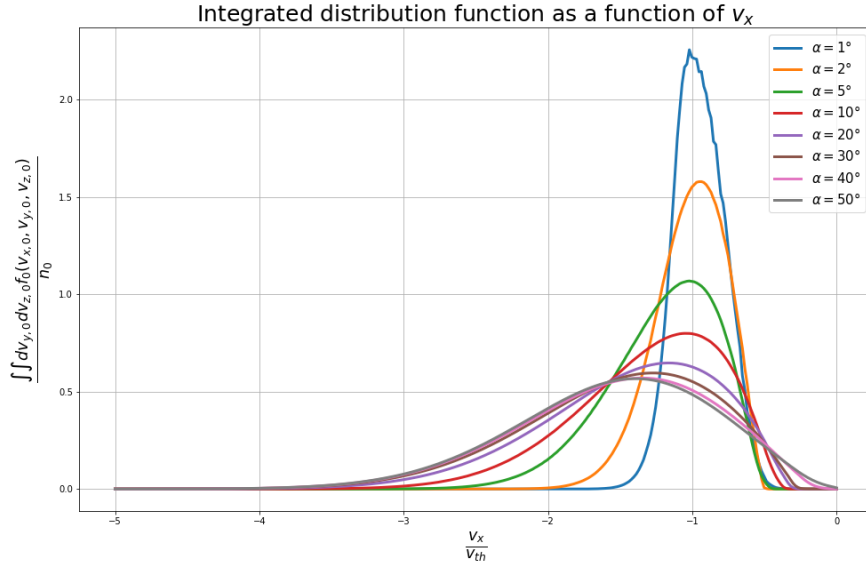


Figure 4.3: Result for distribution function integrated over v_y and v_z at $x = 0$ for different angles α with the self consistent potential from Figure 4.2. The quantity on the y axis is $\frac{\int \int dv_{y,0} dv_{z,0} f_0(\mathbf{v}_0)}{n_0}$. The velocities were sampled on a cartesian grid. The velocity in the x direction is sampled from $-5v_{th}$ to 0 in 400 grid points. The velocity in the z and y direction were both sampled from $-5v_{th}$ to $5v_{th}$ with 200 grid points. The distribution function was obtained using a semi-Lagrangian method.

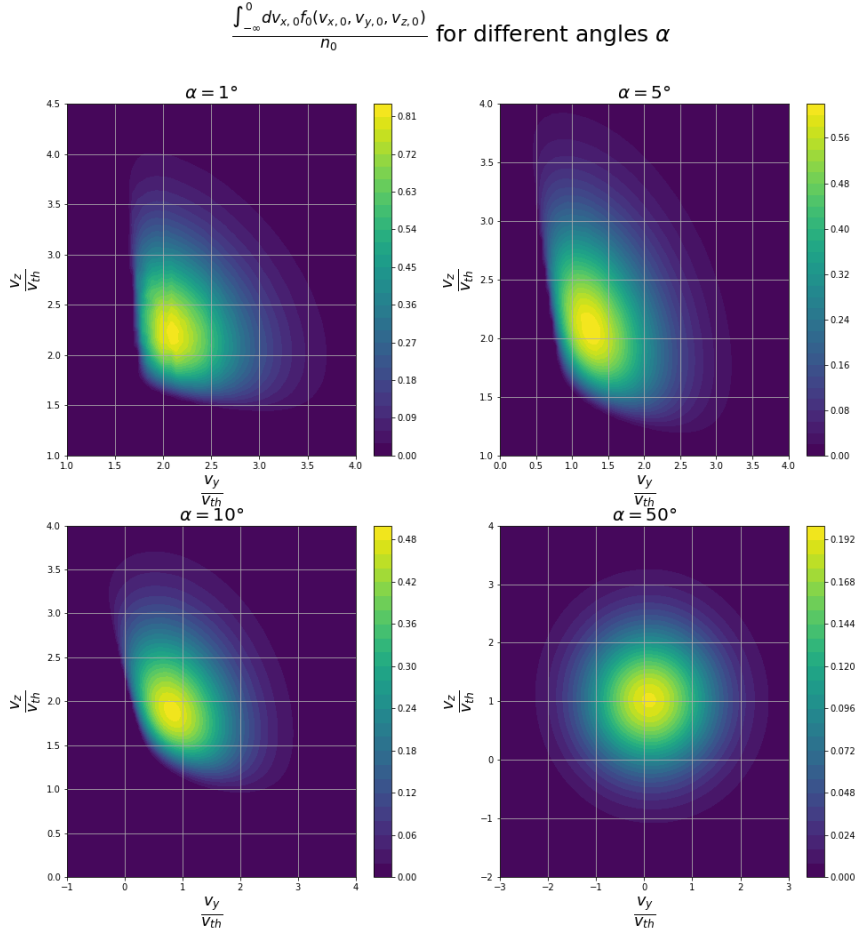


Figure 4.4: Result for the distribution function integrated over v_x at $x = 0$ for different angles α with the self consistent potential from Figure 4.2. The quantity plotted is $\frac{\int_{-\infty}^0 dv_{x,0} f_0(v_0)}{n_0}$. The velocities were sampled on a cartesian grid. The velocity in x direction is sampled from $-5v_{th}$ to 0 in 400 grid points. The velocity in the z and y direction were both sampled from $-5v_{th}$ to $5v_{th}$ with 200 grid points. The distribution function was obtained using a semi-Lagrangian method.

It is insightful to look at how the distribution function at the wall (or Debye sheath entrance) differs from the one that was used as a boundary condition at the magnetic presheath entrance. Remember, Figure 3.1 shows the distribution function at the magnetic presheath entrance. A modified Maxwellian was used that was independent of gyrophase. In Figure 4.4 the distribution function at the wall integrated in v_x is displayed as a function of v_y and v_z for several magnetic field angles α . In Figure 4.5 the distribution function at the wall integrated in v_y as a function of v_x and v_z is displayed for several magnetic field angles α . Figure 4.3 and Figure 4.5 show that the distribution function becomes more localised in v_x when α becomes smaller. Note that the particle flux onto the wall is smaller for smaller α because the flux is conserved. For decreasing values of α , the average flow velocity to the wall gets reduced. In Figure 4.4, observe that, especially for shallow angles, the particles hit the wall with positive z and y velocities. The velocity in z is positive because v_{\parallel} is almost parallel to v_z for small angles, and because particles hitting the wall must have a positive v_{\parallel} . Note that for small α , the gyro-orbit is approximately perpendicular to the z axis. Particles will hit the wall while their velocity in x is negative. Even with an electric field they will tend to hit the wall in the lower part of their gyro-orbit. Because at that point, they are closest to the wall. Particles in the lower part of their gyro-orbit with $v_x < 0$ will mostly have $v'_x < 0$, $v'_x > 0$, and thus $v_y > 0$. This effect is weakened when α increases because at that point v'_x is less and less aligned with v_x .

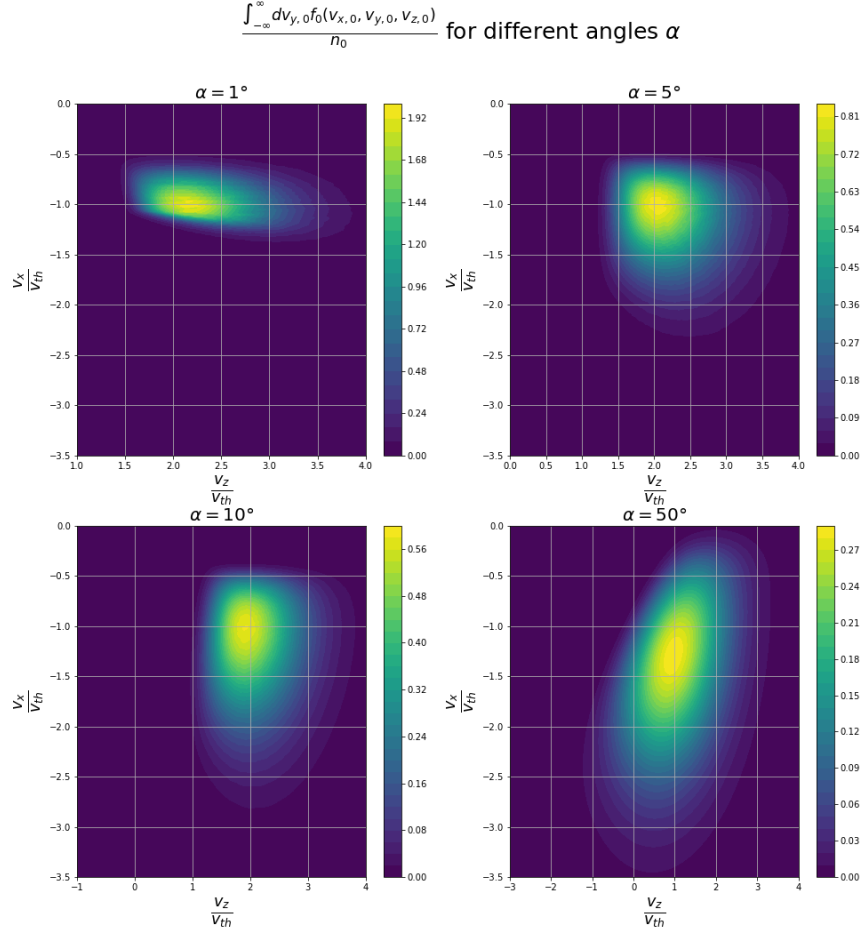


Figure 4.5: Result for the distribution function integrated over v_y at $x = 0$ for different angles α with the self consistent potential from Figure 4.2. The quantity plotted is $\frac{\int_{-\infty}^{\infty} dv_y, 0 f_0(v_0)}{n_0}$. The velocities were sampled on a cartesian grid. The velocity in x direction is sampled from $-5v_{th}$ to 0 in 400 grid points. The velocity in the z and y direction were both sampled from $-5v_{th}$ to $5v_{th}$ with 200 grid points. The distribution function was obtained using a semi-Lagrangian method.

There is another effect that causes particles to have a positive v_y throughout the sheath: they are accelerated by an $\mathbf{E} \times \mathbf{B}$ drift. Since the \mathbf{E} field is only in the x direction and the \mathbf{B} field only in the z and x direction, the $\mathbf{E} \times \mathbf{B}$ drift only has a y component. The $\mathbf{E} \times \mathbf{B}$ drift is equal to $\frac{E}{B} \cos(\alpha) \mathbf{e}_y$ (see Equation 2.8 for the definition of the $\mathbf{E} \times \mathbf{B}$ drift velocity). This means that particles will get accelerated in the positive y direction while they are traveling throughout the system, as the electric field and the associated drift increase. The size of the velocity increase is dependent on the magnetic field angle α : a small α means a larger v_y and a large α means a lower v_y . These are the reasons that particles will mostly hit the wall with positive v_y . It can be seen in the figure that both effects indeed are weakened when α increases because the particles tend to hit the wall with a lower v_y .

Lastly, it is interesting to investigate for which angle the small angle code by Geraldini gives a significantly different self-consistent potential solution compared with the numerical method from this report. As already discussed and shown in Figure 4.1a for an angle $\alpha = 1.8^\circ$, the methods give the same self-consistent potential. Figure 4.6 displays how for increasing magnetic field angles the two numerical methods start to deviate. For $\alpha = 3.6^\circ$, a negligible difference between the two solutions can be seen. For $\alpha = 3.6^\circ$ the difference as calculated before is 4%. In particular, the numerical method from this report gives a slightly less negative value for the potential. When the angle gets larger, this difference starts to grow: the potential obtained from the new numerical method becomes less negative than the potential from the small angle code. For an angle of $\alpha = 9^\circ$, the solution of the small angle code is already

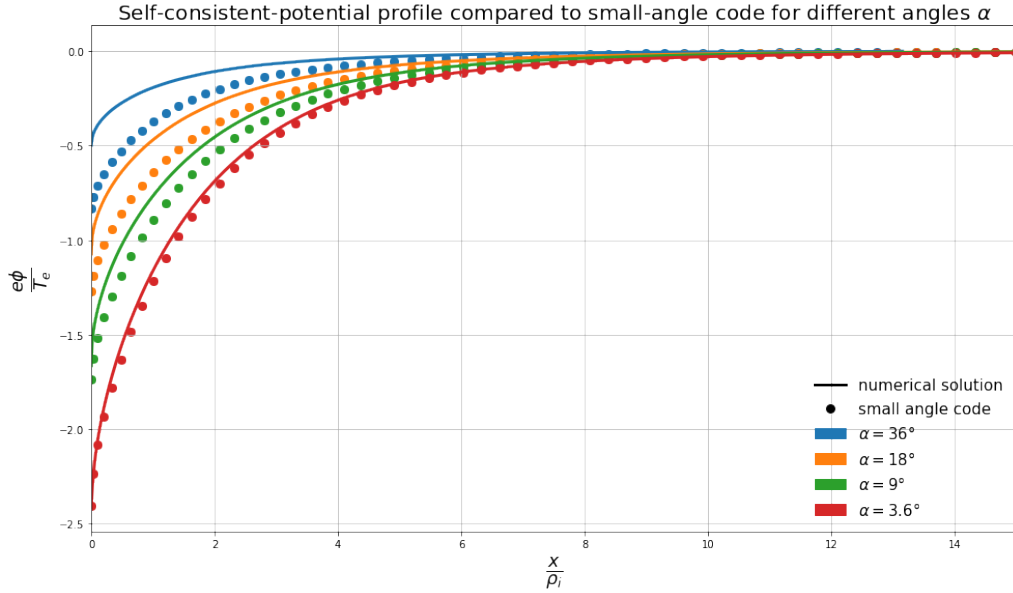


Figure 4.6: Results for the self-consistent potential profile for different magnetic field angles α compared to the ones obtained from the small angle code. The grid in the simulation for $\alpha = 3.6^\circ$ was defined with $\delta = 0.4$. The grid for the other simulations was defined with $\delta = 0.3$. The sampling of velocities in all the simulations were the same. For the sampling of velocity $m_{\lambda,1} = 20$, $m_{\lambda,2} = 20$, $m_{\theta,1} = 801$, $m_{\theta,2} = 101$, and $m_v = 10$. $v_{max} = 5v_{th}$ (Section 3.4). For the time integration: the time steps were chosen such that there are at least 10 time steps per grid cell.

considerably different (13%). It is actually observed that the difference between the two solutions scales linearly with $\sin(\alpha)$. So it would probably not be wise to use the small angle code for angles bigger than 9° . Note that the small angle code is based on an expansion of $\alpha \ll 1$ and $9^\circ \approx 0.15 \text{ rad} \lesssim 1$. It thus seems that the small angle code overestimates the potential drop. Considering higher order terms in the small α expansion will likely lower the expected potential drop. Lastly, it is important to realise that not only the absolute difference between the two algorithms increases with increasing α ; the relative difference increases even more because the potential drop decreases with larger α .

4.3 Magnetised sheath simulations

Now the results of simulations of the entire magnetised sheath will be shown and discussed. The method used is the one discussed in Section 3.5.2. Note that in contrast to the magnetic presheath simulations the iterative scheme solves a second-order differential equation. This requires two boundary conditions on $\phi(x)$. One will be ϕ_∞ , and the other will be ϕ_0 . Thus the potential drop in the simulations below is artificially set. In the simulations $Z = 1$, so single charged ions are considered. In the simulations linear basis functions are used as defined in Equation 3.15. Note that this means that the speedup owing to the analytical treatment of a particle in a piece-wise constant electric field (see Section 3.7.2) is also used.

In Figure 4.7 the results for the self-consistent potential field in the magnetised sheath together with the electron and ion densities are displayed. The value of ϕ_0 was chosen in such a way that it was lower than the ϕ_0 from the magnetic presheath simulations in Figure 4.2. The simulations were carried out with $\gamma = \frac{\lambda_D}{\rho_i} = \frac{1}{50}$, which is a realistic value of γ in a nuclear fusion reactor as was shown in [7] with data from [50]. This means that there will be a very small Debye sheath where the electric force dominates over the magnetic force. It can also be seen in the figure that up to very close to the wall the solution is quasi-neutral. In Figure 4.8 a zoom of the density plot in Figure 4.7 can be seen. This highlights the charged region very close to the wall. Note that the axis is now given in units of $\frac{x}{\lambda_D}$. The fact that the numerical solution gives a quasi-neutral magnetic presheath and a charged Debye sheath with the size of a few λ_D indicates that the correct physics is reproduced with the numerical method. The potential profiles obtained are consistent with the literature, see for example Chodura [12] and Coulette et al. [43].

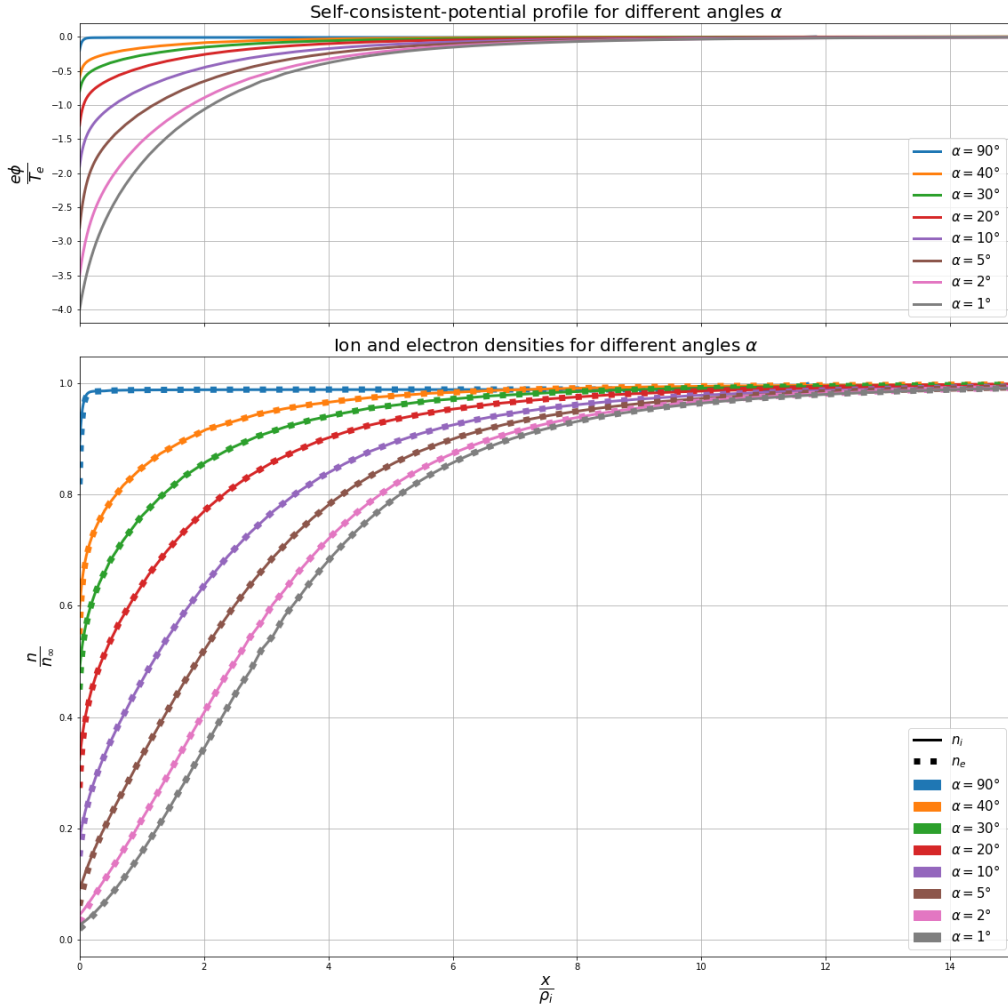


Figure 4.7: Results for self-consistent potential (above) and the accompanying ion and electron densities (below) in the magnetised sheath for different α . The sampling of velocities in all the simulations were the same. For the sampling of velocity $m_{\lambda,1} = 20$, $m_{\lambda,2} = 20$, $m_{\theta,1} = 1601$, $m_{\theta,2} = 201$, and $m_v = 10$. $v_{max} = 5v_{th}$ (Section 3.4). The value of $\gamma = 0.02$ in these simulations, meaning that the Debye length is 50 times smaller than the ion gyroradius. For each simulation an x grid like the one in Equation 3.51 was used, all simulation had $m = 40$, all simulations had $\Delta x_{ds} = 0.5\lambda_D$, the value of $\kappa = 1$. The value of δ was different for all the simulations: for $\alpha = 90^\circ$ $\delta = 0.7$ was used, for $\alpha = 50^\circ$ $\delta = 0.8$ was used, for $\alpha = 40^\circ$ and $\alpha = 30^\circ$ $\delta = 0.7$ was used, for $\alpha = 20^\circ$ and $\alpha = 10^\circ$ $\delta = 0.6$ was used, for $\alpha = 5^\circ$ $\delta = 0.5$ was used, and for $\alpha = 1^\circ$ and $\alpha = 2^\circ$ $\delta = 0.3$ was used. In the lower plot the colors indicate the different angles and the dotted line represents the electron density while the solid line is the ion density.

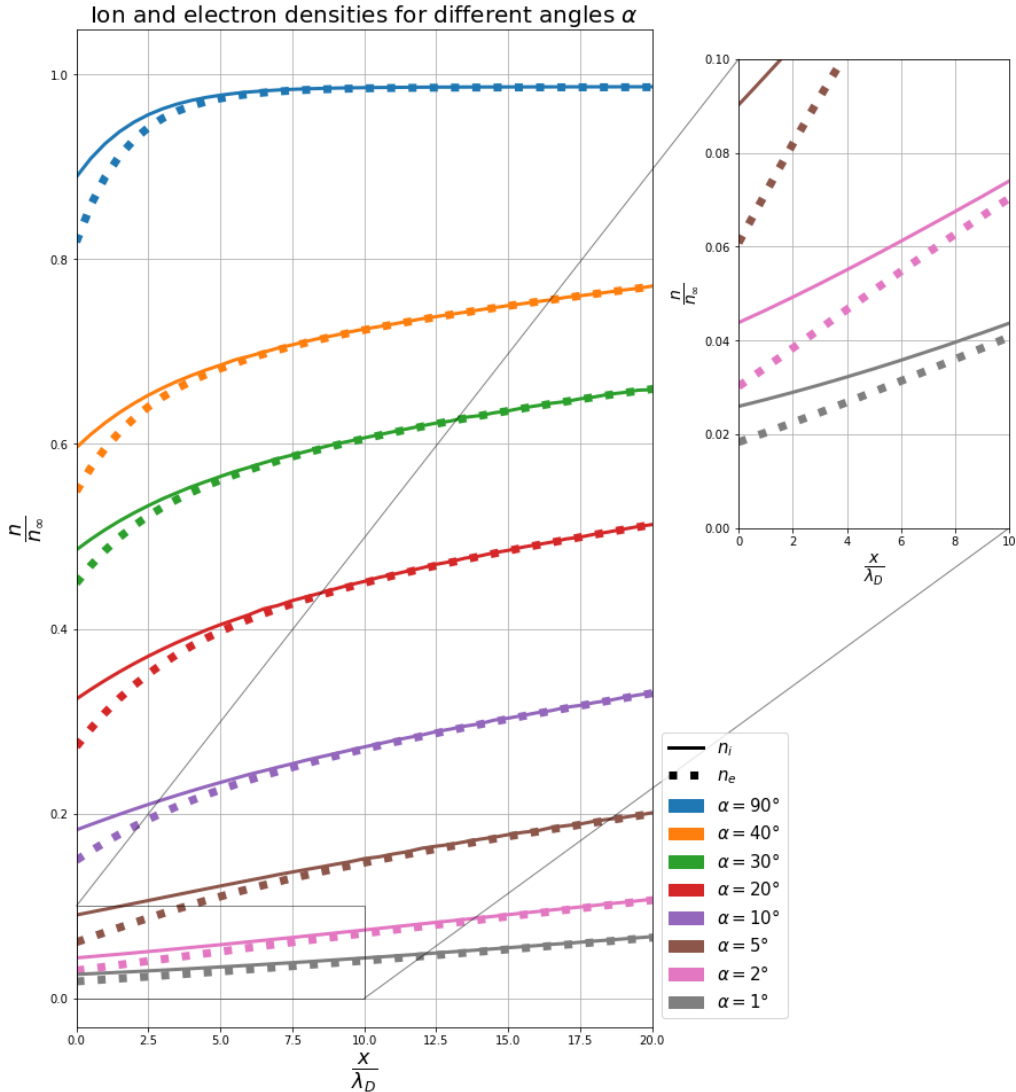


Figure 4.8: A zoom of the ion and electron density in Figure 4.7. Here it is clear that a charged region of a few λ_D develops, which is the Debye sheath.

The size of the Debye sheath compared with the magnetic presheath is dependent on the value of γ . Figure 4.9 illustrates that the self consistent potential of the magnetised sheath approaches the solution of the magnetic presheath when $\gamma \rightarrow 0$.

As explained before, the magnetic presheath simulation is based on a scale separation. The location $x = 0$ is related to particles hitting the wall. But in reality, before the wall, there is an infinitesimally⁷ small region: the Debye sheath. This scale separation is what gives rise to the Bohm condition derived in Section 4.1 as well as the shape of the potential. When the Debye sheath is included in the calculation, the Bohm condition is not necessarily satisfied, and the Debye sheath entrance is a fuzzy region instead of a point, as was discussed in Section 2.3. It is interesting to compute the distribution function of the magnetised sheath simulation in this region, to see whether it is similar to the distribution function at the wall that was obtained in the simulations of the magnetic presheath. One would also want to see how the distribution function in the Debye sheath entrance changes for $\gamma \rightarrow 0$. It should go towards the distribution function of the magnetic presheath just like the potential of the magnetised sheath goes to the potential of the magnetic presheath for $\gamma \rightarrow 0$. But for that, an approximation of the location of the Debye sheath entrance must be carried out.

⁷or at least it is assumed to be infinitesimally small

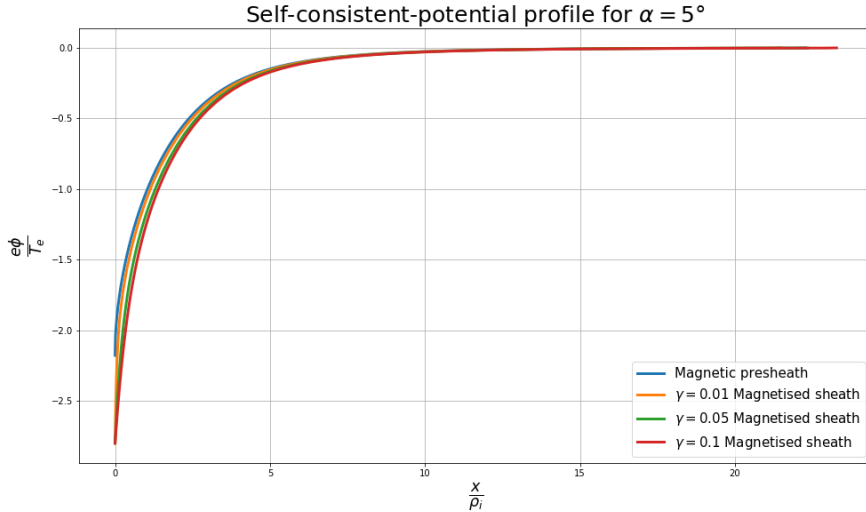


Figure 4.9: In blue the self-consistent field of the magnetic presheath simulation with $\alpha = 5^\circ$ taken from Figure 4.2 is displayed. In the other three colors the results of the self-consistent potential field at the same α for different values of γ is displayed. It can be seen that when $\gamma \rightarrow 0$ the potential field tends to go to the potential field solution of the magnetic presheath. In the simulation of the magnetised sheath the same velocity sampling and grid spacing was used as in Figure 4.7 for $\alpha = 5^\circ$.

To find the location of the Debye sheath entrance, it is useful to refer to Figure 2.1. First, it is important to note that λ_D changes as a function of x because n_e decreases. This means that γ also changes as a function of x . γ increases moving closer to the wall because λ_D increases with decreasing electron density. To not cause confusion $\gamma := \frac{\lambda_{D,\infty}}{\rho_i}$ with $\lambda_{D,\infty}$ the value of λ_D at the magnetic presheath entrance. To obtain a guess of the value of x_{dse} in Figure 2.1 one will need to estimate the region where the solution goes from following the quasi-neutral solution in the magnetic presheath to the charged solution in the Debye sheath. It thus makes sense to define the Debye sheath entrance at a point where the charge density is a certain percentage of the local value of the electron density. It turns out that the potential in the Debye sheath entrance is of the order of $\left(\frac{\lambda_{D,dse}}{\rho_i}\right)^{2/5} \frac{T_e}{e}$ [9], where $\lambda_{D,dse}$ is the local value of λ_D at the Debye sheath entrance. Note that λ_D scales with the square root of the density and thus $\lambda_{D,dse} \sim \sqrt{\frac{n_\infty}{n_{dse}}} \lambda_{D,\infty}$, with n_{dse} the density at the Debye sheath entrance. It also turns out that $x_{dse} \sim \left(\frac{\lambda_{D,dse}}{\rho_i}\right)^{4/5} \rho_i$ [9]. Using Poisson's equation:

$$\phi''_{dse} \sim \rho_{dse} \sim \frac{T_e \left(\frac{\lambda_{D,dse}}{\rho_i}\right)^{2/5}}{e \left(\frac{\lambda_{D,dse}}{\rho_i}\right)^{8/5} \rho_i^2} \sim \left(\frac{\lambda_{D,dse}}{\rho_i}\right)^{-6/5} \frac{T_e}{e \rho_i^2} \sim \left(\frac{\lambda_{D,dse}}{\rho_i}\right)^{4/5} \frac{T_e}{e \lambda_{D,dse}^2}. \quad (4.45)$$

Note that $\frac{T_e}{e \lambda_{D,dse}^2} \sim \phi''_{dse}$. Now note that $\phi''_{dse} \sim n_{dse}$ because ρ depends on the ion density, which does not drop much in the Debye sheath (only a factor of unity) and the electron density, which drops rapidly in the Debye sheath. Thus the charge density scales with the electron density at the Debye sheath entrance. This now gives with the scalings of $\lambda_{D,dse}$:

$$\rho_{dse} \sim \left(\frac{\lambda_{D,dse}}{\rho_i}\right)^{4/5} n_{dse} \sim \left(\frac{\lambda_{D,\infty}}{\rho_i}\right)^{4/5} \left(\frac{n_\infty}{n_{dse}}\right)^{2/5} n_{dse} \quad (4.46)$$

And thus the Debye sheath entrance in the simulations is considered to be at the location where

$$\frac{\rho_{dse}}{n_{dse}} = \gamma^{4/5} \left(\frac{n_\infty}{n_{dse}}\right)^{2/5}. \quad (4.47)$$

Or in words, the location where the charge density is approximately a fraction $\gamma^{4/5} \left(\frac{n_\infty}{n_{dse}}\right)^{2/5}$ of the

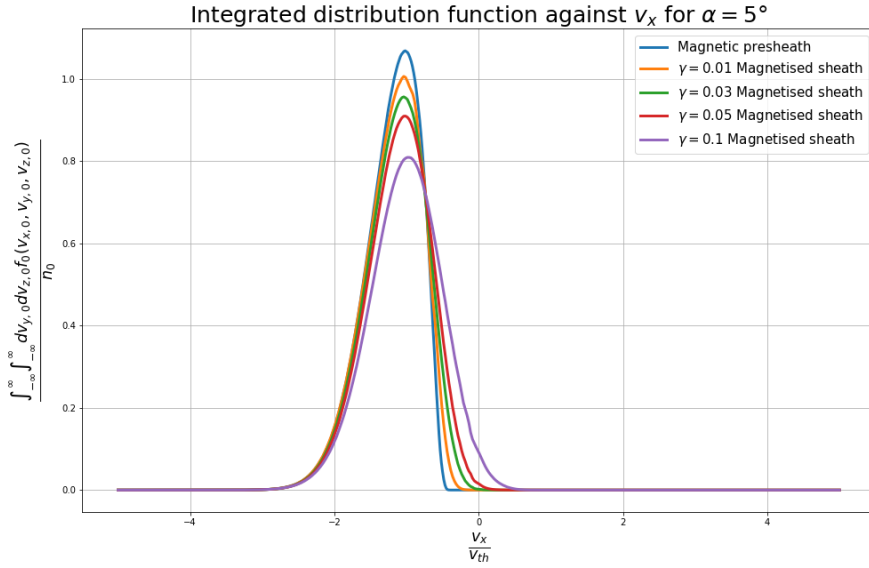


Figure 4.10: In blue the distribution function at $x = 0$ of the magnetic presheath simulation with $\alpha = 5^\circ$, taken from Figure 4.3, is displayed. In the other three colors the results of potential distribution at the location where Equation 4.47 is satisfied for the same α and for different values of γ is displayed. It can be seen that when $\gamma \rightarrow 0$ the distribution function tends to go to the distribution function of the magnetic presheath that tends to satisfy the Bohm condition. The distribution function for the magnetised sheath was obtained with a semi-Lagrangian approach and the same velocity sampling as in Figure 4.3 was used. The potential profile used to obtain these distribution functions are the ones of Figure 4.9

electron density. Note that this is a scaling, so a numerical factor of order unity should not make a difference.

Figure 4.10 shows the distribution function at the location that was just derived in the magnetised sheath for different values of γ compared to the distribution function at the wall of the magnetic presheath simulation. The distribution function of the magnetic presheath simulation tends to satisfy the Bohm condition, and it can be seen that for $\gamma \rightarrow 0$, the distribution tends to the one of the magnetic presheath. This lends support to the fact that the Bohm condition tends to being satisfied in the limit of an infinitesimally small Debye sheath. Note that for $\gamma = 0.1$ the distribution seems to not exactly follow the trend of the other values of γ in Figure 4.10: its peak seems to be shifted a bit. The reason for this is that the region of the Debye sheath entrance becomes so large that the potential drop in this region becomes significant (see again Figure 2.1 for reference). Because of this significant potential drop, the distribution function considerably changes over the fuzzy region that is the Debye sheath entrance. This makes that picking a point in this region can lead to very different distribution functions. It also makes sense that the distribution function does not even approximately satisfy the Bohm condition because for $\gamma = 0.1$, the scale separation of magnetic presheath and Debye sheath does not hold. In that case, the Debye sheath starts to become of comparable size to the magnetic presheath, especially for small α when $\lambda_{D,dse}$ is much larger than $\lambda_{D,\infty}$.

It is interesting to look at the distribution of incoming ions at the target. This will give insight into how the ions will hit the wall, and that will be helpful for understanding plasma wall interactions. Figure 4.11 shows the distribution function integrated over v (the magnitude of the velocity of the particle) at the target obtained from the magnetised sheath simulation. It illustrates how particles tend to hit the solid target. The angles in the labels of the figure are related to the velocity the particles have at the target:

$$\begin{aligned} v_{x,0} &= -v \cos(\theta) \\ v_{y,0} &= v \sin(\theta) \sin(\psi) \\ v_{z,0} &= v \sin(\theta) \cos(\psi) \end{aligned} \tag{4.48}$$

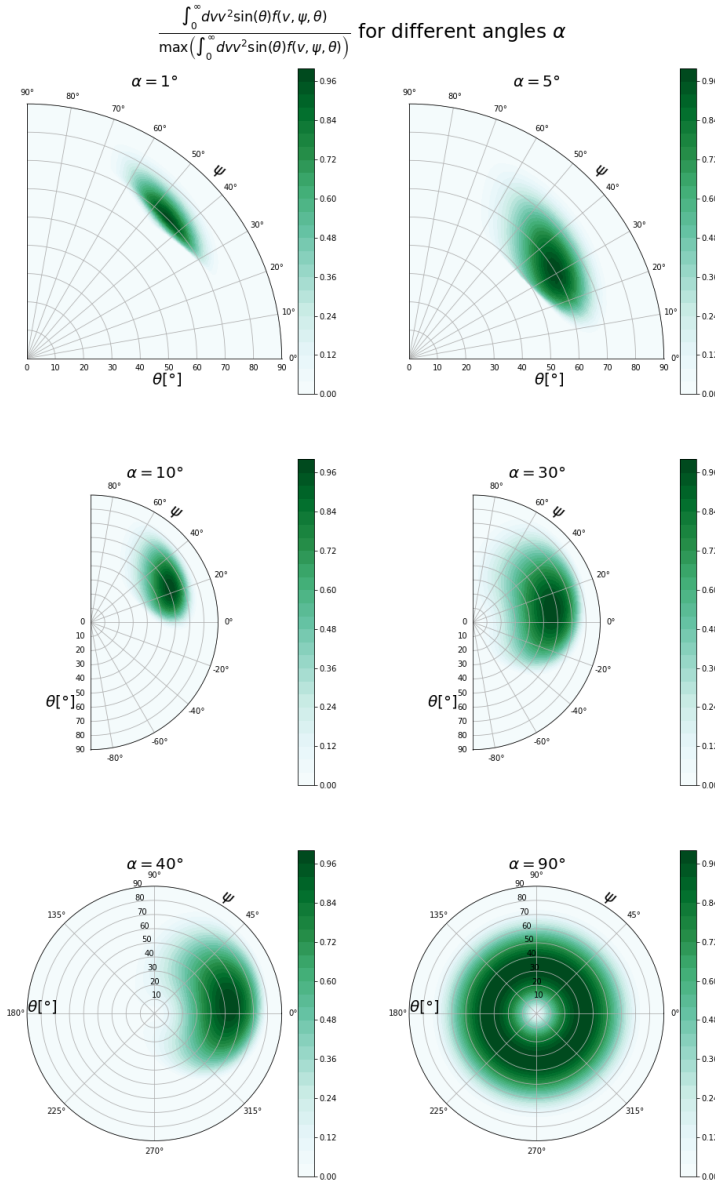


Figure 4.11: Results of the distribution function in the magnetised sheath when hitting the target, for the potential profile in Figure 4.7. The quantity plotted is $\frac{\int_0^\infty dv v^2 \sin(\theta) f(v, \psi, \theta)}{\max(\int_0^\infty dv v^2 \sin(\theta) f_0(v, \psi, \theta))}$ for different magnetic field angles α . The profiles were obtained by sampling 400 particles in ψ where ψ goes from 0 to 2π , 200 particles were sampled in v where v goes from 0 to $5v_{th}$, θ was sampled from 0 to $\frac{\pi}{2}$ with 200 particles. The distribution function was obtained with a semi-Lagrangian method.

Thus note that $\theta = 0^\circ$ means that the particles hit the solid target perpendicular to it. When θ is larger, the particles graze the wall. Note that the distribution function is highly localised, especially for small angles. Again for small α , all particles hit the wall in only the upper right quadrant, where v_y and v_z are both positive. This was already discussed in the previous section. Note that for $\alpha = 90^\circ$, circular

contours are observed in the distribution function. This is expected because if $\alpha = 90^\circ$, the particles will have a gyro-orbit oriented parallel to the wall. The particles can have any velocity angle ψ . The entire magnetised sheath system becomes 1D 1V if $\alpha = 90^\circ$, which is also observed by the fact that the circular contours are observed as this indicates complete symmetry over ψ .

It is valuable to look at the distribution function at the target for a specific magnitude of the velocity v . In Figure 4.12 the distribution at the target for $v = 4v_{th}$ is shown. As can be seen many particles hit the wall, which makes sense because the energy gain in the magnetised sheath is significant. Interestingly, the particles with this specific velocity at the target all were sampled with the same velocity at the magnetic presheath entrance. This is because the value of the velocity is determined by the total energy gain in the system. In the case of the magnetised sheath, the energy gain is proportional to the potential difference. All particles have felt the same potential traveling through the sheath. The fact that there are different hues of green along lines of constant θ in the plot is related to the fact that a modified Maxwellian distribution function was used as the distribution function at the sheath entrance. If a Maxwellian distribution would have been used, the non-zero portions of the plot along lines of constant θ would have had all the same hues. For the modified Maxwellian, v_{\parallel} is the only quantity that determines the value of the distribution function at constant v . So the different hues along lines of constant θ in the figure are related to different values of v_{\parallel} of the particles at the sheath entrance. For smaller ψ , the value of the distribution function becomes larger because the v_z component is larger while the v_y component is smaller. Therefore, particles with a higher v_{\parallel} at the sheath entrance, which are more numerous at fixed v , will also tend to hit the wall with a higher v_{\parallel} and smaller ψ .

What can we learn from this for a reactor, for example what does this tell us about sputtering. For sputtering, it is most insightful to look at the sputtering angle and impact energy at the target. In Figure 4.13 the distribution function integrated over ψ is shown as a function of sputtering angle and energy. Note that the axes indicate $90^\circ - \theta$ i.e. 90° means that the particles hit the wall perpendicular to the wall. For smaller angles, the particles hit the wall at a more shallow angle. The particles will also hit the wall with higher energy. Note that similar plots have been obtained by Geraldini [44], Khaziev and Curreli [46], and Coulette and Manfredi [43]. Several works have looked into how impact angle and impact energy influence sputtering. Normally the impact of sputtering is quantified in the sputtering yield, which is defined as the number of sputtered particles divided by the number of particles impacting the wall. A good review of sputtering yields for different materials and different impact ions can be found in Eckstein et al. [51]. It highlights the complexity of sputtering. The sputtering yield mainly depends on the ion species hitting the wall, the material of the target, the impact angle, and the impact energy. It becomes clear that for sputtering to occur, the impact energy has to be above a certain threshold. Below it, the material won't be damaged. Above the threshold, the sputtering yield rapidly increases, after which it slowly falls because, for energies that are too high, the particles will penetrate too deep into the material and will not deposit as much energy close to the surface. The sputtering yield as a function of incident angle and incident energy has been studied both numerically and experimentally [52, 53, 54]. In general, a trend is observed for large angles between the target and the incoming ions the sputtering yield is low. It then slowly increases for more shallow angles until a maximum is reached. The reasoning for this is that when the particles hit the wall head-on, most of the energy will be deposited far into the material and not close to the surface, and thus less sputtering will occur⁸. After the maximum, it falls rapidly. Eventually, it will drop to zero. So there is some threshold where the particles hit the wall with such a shallow angle that they will not sputter. This is because for more and more shallow angles, the probability of reflection increases. The angle at which the threshold occurs depends on the ion species and the target species. For fusion applications, one is interested in the sputtering of deuterium on a Beryllium Tungsten alloy. To see why note that the divertor plate in a nuclear fusion reactor is made out of Tungsten, and the first wall is made from Beryllium. Beryllium that is sputtered from the first wall can, therefore, be transported and deposited on Tungsten [56]. And thus, the sputtering at the divertor is expected to be deuterium on a Tungsten Beryllium alloy. In [52], this sputtering of deuterium on this alloy was studied. Given the plots in Figure 4.13, it is expected that for smaller angles between the magnetic field and the wall α , the sputtering yield increases because the particles will hit the wall with a more shallow angle and with higher energies. However, it should be noted that the particles can hit the plates at shallow enough angles that the sputtering yield is zero, because the angle is below the threshold.

⁸It is, in fact, the case that when the energy gets deposited deeper into the material a different type of sputtering will occur: non-linear sputtering where the sputtering happens after multiple collisions of the target atoms inside the solid target [55].

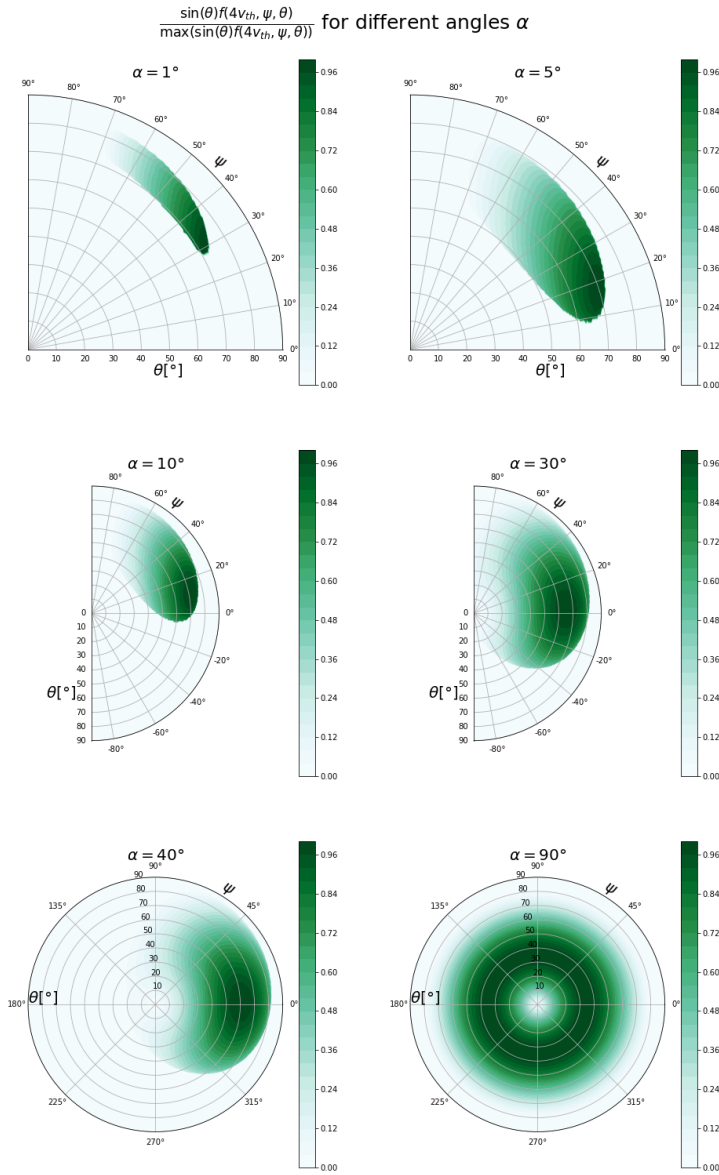


Figure 4.12: Results of the distribution function in the magnetised sheath when hitting the target with $v = 4v_{th}$ for different magnetic field angles α . The quantity plotted is $\frac{\sin(\theta)f(4v_{th},\psi,\theta)}{\max(\sin(\theta)f_0(4v_{th},\psi,\theta))}$. The potential from Figure 4.10 was used to obtain the results. The profiles were obtained by sampling 400 particles in ψ where ψ goes from 0 to 2π , 200 particles were sampled in v where v goes from 0 to $5v_{th}$, θ was sampled from 0 to $\frac{\pi}{2}$ with 200 particles. The distribution function was obtained with a semi-Lagrangian method.

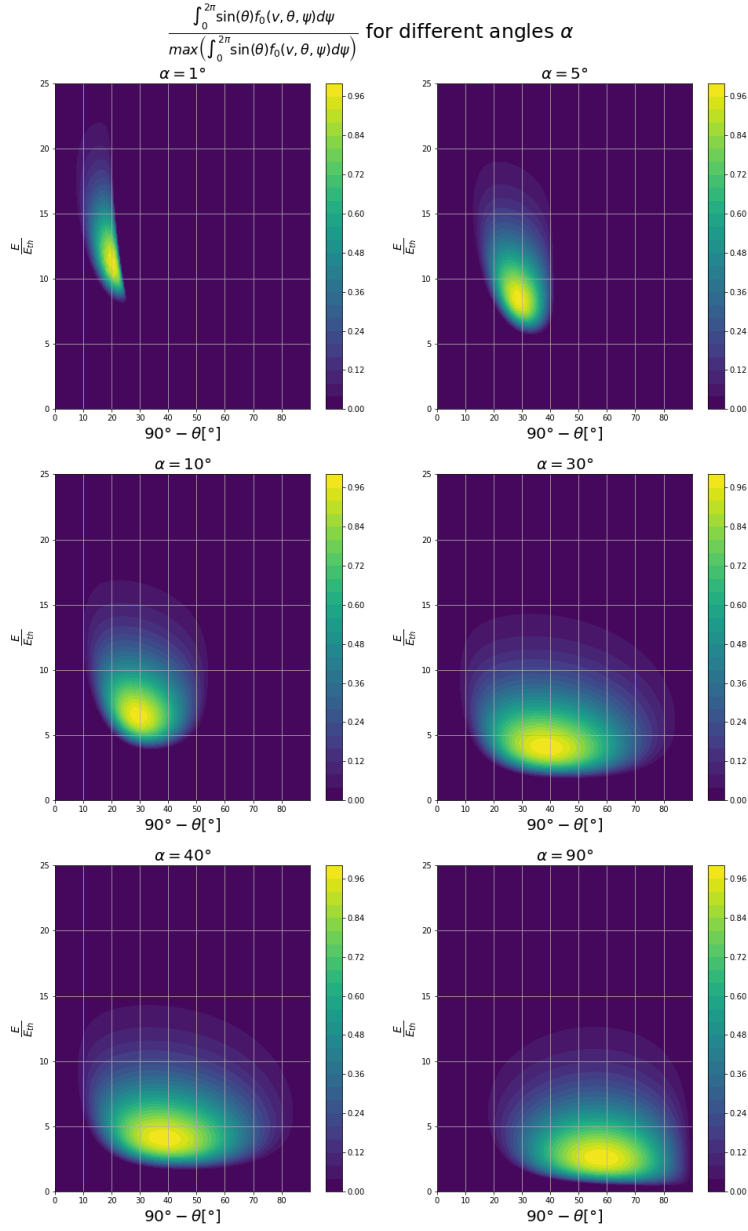


Figure 4.13: Result for distribution at the target compared as a function of impact angle and impact energy for different magnetic field angles α . In the simulation the potential profiles from Figure 4.10 was used. The quantity that is plotted is $\frac{\int_0^{2\pi} \sin(\theta) f(v, \theta, \psi) d\psi}{\max(\int_0^{2\pi} \sin(\theta) f(v, \theta, \psi) d\psi)}$. The profiles were obtained by sampling 400 particles in ψ where ψ goes from 0 to 2π , 200 particles were sampled in v where v goes from 0 to $5v_{th}$, θ was sampled from 0 to $\frac{\pi}{2}$ with 200 particles. The distribution function was obtained with a semi-Lagrangian method. The energy is normalised with respect to $E_{th} = \frac{1}{2}v_{th}^2$.

4.4 General discussion

Some general remarks must be discussed about the numerical method. It was highlighted before that the \sqrt{x} behavior cannot be resolved in the first grid cell using the finite element method. It should be mentioned that two approaches were tried to solve this problem.

One approach was to use basis functions expressed in $g := \sqrt{x}$. This would make the behaviour in \sqrt{x} linear in g , and that makes it possible to resolve the \sqrt{x} behaviour with the finite element method. In practice this is done by rewriting $\phi(x)$ to $\phi(g)$, but that also implies that $\mathbf{E} = \frac{d\phi}{dx}\mathbf{e}_x = \frac{1}{g}\frac{d\phi}{dg}\mathbf{e}_x$. The \mathbf{E} field diverges when g (or x) tends to zero. For integrating the particle trajectories, which cannot be done analytically if the system is expressed in g , the divergence means that the force becomes infinite close to the wall. It makes integrating the particle trajectories correctly close to the wall difficult. This causes a problem for small magnetic field angles α , where the ion density is low. Note that an absolute error in the ion density close to the wall gives a large change in ϕ because ϕ changes with $\log(n_i)$, which becomes very steep for small n_i . The divergence in the force has an impact on the accuracy of calculating the time a particle spends close to the wall, which has an impact on the value of n_i . To be precise, the divergence in the electric force makes the time a particle spends in the first grid cell smaller, thus decreasing n_i . This lowers the potential, and the self-consistent potential drop obtained becomes too large.

Another approach used the effective potential from Equation 4.10. As explained in Section 4.1; with the effective potential, one can predict if a particle close to the wall will hit the wall. If it is known that a particle will hit a wall one can calculate $v_{x,0}$ with Equation 4.17 and then obtain $n_{i,0}$ by evaluating the integral: $\int d^3\mathbf{v}_\infty v_{x,\infty} \frac{f_\infty}{v_{x,0}}$ directly, which should not give any problems because as proven in Section 4.1 there are no particles with $v_{x,0} = 0$. The method didn't give correct results. The reason for that is unknown. It might be the case that particles with small $v_{x,0}$ hit the wall, which drives the ion density at the wall up. Including the Debye sheath will get rid of the \sqrt{x} dependence close to the wall. A code that can solve for the entire magnetised sheath is more complete than a code that can solve the magnetic presheath. Because it was possible to resolve the Debye sheath, trying to make a code that can deal with the \sqrt{x} dependence was not further pursued.

The new method described in this report has the potential to become the new state-of-the-art method to find the steady state of a magnetised sheath. The current methods used are PIC codes or Eulerian codes. PIC codes sample from a distribution function giving statistical noise. Therefore, one needs to simulate a lot of particles. They also have to resolve the smallest plasma length, i.e. the Debye length or the electron Larmor radius, and the smallest time scale, i.e. the electron Larmor frequency, the plasma frequency, or the upper hybrid frequency everywhere in the entire system. Eulerian codes do not have the problem of statistical noise but are computationally less efficient [57, 58].

The method presented in this report has a two-fold improvement on PIC codes. It is not prone to statistical noise because it integrates the distribution function directly in velocity space. It also gives a speedup compared to PIC codes. Now the speedup will be discussed. For that an equation to estimate the number of operations is given: $N_{operations} \sim N_v N_x N_{steps}$. A PIC code uses a different algorithm so the meaning of N_v , N_x and N_{steps} is not necessarily the same in both codes. In a PIC code N_v particles are released in each N_x grid points. After one time step (or iteration) the particles have deposited their charge on the grid and the fields are calculated. With the newly calculated fields this process is repeated until a steady state is reached. So, for the PIC code N_{steps} is related to the number of time-steps it takes for the system to reach equilibrium. In the new code discussed in this report, N_v particles are released at the sheath entrance, they are followed until they reach the wall, after that the new field is calculated. This process is repeated N_{steps} times until a steady state is reached. Note that the particles in this code also deposit their charge in each grid cell N_x by calculating the time it takes for a particle to cross a grid cell. Which is done semi-analytically with linear basis functions.

In PIC codes N_v is the number of particles that are released in each grid cell. This is usually around 1000 particles. The new code discussed in this report gives correct results with 10 particles sampled from v , 20 particles sampled from λ and around 50 particles sampled from θ . This is 10^4 particles. It is convenient to define $N_{v,p} = 1000$ as the number of particles sampled per grid cell in PIC codes and $N_{v,n} = 10^4$ as the number of particles sampled in the new method.

Now for the value of N_x one has to realise that in PIC codes the Debye length has to be resolved everywhere. The number of grid points in a PIC code scales with $\rho_i/\lambda_D = 1/\gamma$ because the Debye length has to be resolved in a system that has the size of a few ρ_i . The numerical method presented in this

report only has to resolve the Larmor radius and thus the number of grid points needed scales with ρ_i/ρ_i . Note, however, that particles cross a grid point after the time of crossing τ has been found, and thus there are per grid cell 10 iterations needed on average to find τ . So, in actuality N_x in the code from this simulation scales with $10\rho_i/\rho_i$.

The real time gain in the method from this report is the number of steps needed to reach a steady state. The simulations presented in the results were all done with a weight of 0.2, in that case around 70 steps are needed to reach a steady state. In the magnetised sheath system it is possible to use a weight of 0.5, which means that only 20 steps are needed. A PIC code, on the other hand, needs step size related to resolving the smallest time scale in the plasma. The smallest time scale in the plasma is the plasma frequency. A magnetised sheath system is equilibrated in the characteristic time an ion takes to cross the magnetised sheath system. Thus the number of steps is given by:

$$N_{steps,p} \sim \frac{\rho_i}{\frac{1}{20} T_{pe} v_{th,i} \sin(\alpha)},$$

where T_{pe} is the period of the plasma frequency and $\rho_i/(v_{th,i} \sin(\alpha))$ is the characteristic time an ion takes to cross the magnetised sheath. The factor of 1/20 is included because the plasma frequency has to be resolved [46]. Using the definition of T_{pe} as discussed in Section 2.2 one obtains:

$$N_{steps,p} \sim \frac{20}{\sin(\alpha)} \frac{\rho_i}{\lambda_D} \sqrt{\frac{m_i}{m_e}}.$$

Combining everything, the estimated speedup in this method compared to the PIC codes will be approximately

$$\frac{N_{operations,p}}{N_{operations,n}} \sim \frac{N_{v,p} N_{x,p} N_{steps,p}}{N_{v,n} N_{x,n} N_{steps,n}} \sim \frac{1000 \times \frac{\rho_i}{\lambda_D} \times \frac{20}{\sin(\alpha)} \frac{\rho_i}{\lambda_D} \sqrt{\frac{m_i}{m_e}}}{10^4 \times 10 \times 20} \quad (4.49)$$

where the subscript n stands for the new method discussed in the report and the subscript p stands for PIC codes. Taking a realistic value of $\gamma = \frac{1}{50}$ and a shallow angle $\alpha \simeq 0.1$, which is the one of interest for fusion reactors, this computes to a speedup of 10^4 .

5 Conclusion

In this report, a new numerical algorithm to simulate the magnetised sheath, as well as the scale-separated magnetic presheath, was presented. The main goal of this research was to develop a numerical algorithm that exploits a fixed point iteration to directly solve for the steady state of a collisionless magnetised sheath for general magnetic field angles. This has been done successfully. The results obtained show, in both the magnetic presheath and the magnetised sheath, self-consistent potential profiles that agree with the literature. Simulations of the magnetic presheath with small magnetic field angle are consistent with the solution of the small angle expansion of Geraldini [13, 14]. The potential profiles satisfy quasi-neutrality with an integrated error calculated with Equation 4.44 of less than 0.1% for all magnetic field angles α . The self-consistent potential field close to the wall (with the exclusion of the first element) follows the predicted \sqrt{x} behaviour. The simulations in the magnetised sheath show a self-consistent potential field that is consistent with literature [43, 12]. It gives a solution that is quasi-neutral for $x \gg \lambda_D$ and charged for $x \sim \lambda_D$ as expected. It was also shown that the solution in the entire magnetised sheath converges to the solution of the magnetic presheath when $\frac{\lambda_D}{\gamma} \rightarrow 0$.

There were some other question that arose with this research. They will be answered below:

- **How does the distribution function of ions reaching the solid target differ from that of ions entering the magnetised plasma sheath?**

It can be concluded that the distribution function in both the magnetised sheath and the magnetic presheath becomes highly localised when the target (or in the case of the magnetic presheath, the infinitesimally small Debye sheath) is hit. In particular, the distribution gets shallow as a function of v_x , depending on the magnetic field angle α . When α is smaller, the distribution function is more localised. The particles hit the target mostly with $v_y > 0$ and $v_z > 0$.

- **Above what value of magnetic field angle does the existing magnetised sheath model by Geraldini, which requires a small angle between magnetic field and target, become invalid [13] [14]?**

It was shown that the potential profile of the small angle expansion starts to deviate significantly from the numerical method for $\alpha \sim 0.1$ rad.

- **Can the steady-state solution of the magnetised sheath be applied to develop boundary conditions for models used to simulate plasma in a fusion device?**

This question cannot be answered conclusively, but in the end, it is a question of numerical efficiency. The numerical method presented in this report is projected to be more efficient for simulating the steady state magnetised sheath system than other numerical methods. The code should be able to include more physics e.g. adding collisions, adding dimensions, adding surface roughness, and multiple ion species. The combination of speed and the ability to include more physics lends itself to potentially employing the numerical method to obtain boundary conditions for gyrokinetic simulations.

- **What functional dependency does the self consistent potential profile of a quasi-neutral magnetic presheath follow analytically close to the target?**

It was shown analytically that the potential profile scales with \sqrt{x} close to the wall for all magnetic field angles α .

- **Can the Bohm condition be derived from the quasi neutrality condition of the magnetic presheath?**

It was shown that the Bohm condition must be marginally satisfied on the scale of the magnetic presheath. This condition arises from the condition that the plasma has to be quasi-neutral for $x \rightarrow 0$. It is paired with a field singularity in the electric field.

6 Outlook

The code developed in this report has a lot of potential. Some ideas for future research will be highlighted here.

First, the speedup for the piece-wise constant electric field can be extended to a piece-wise linear electric field, which would allow the speedup to extend to second order basis functions. The equations of motion in a linear electric field are a set of 4 first-order linear ordinary differential equations. They can be solved to obtain $x(t)$ and $\mathbf{v}(t)$ inside a grid cell. A similar numerical algorithm can be devised that, just like the one from Section 3.7.2, solves the time a particle spends in the grid cell τ . If the same sort of algorithm is used one would need to look at times where $\ddot{v}_x = 0$ instead of $\dot{v}_x = 0$. In principle, the idea stays the same. It just involves one additional step: one can look for the time range in which the root of \dot{v}_x lays. With the times where $\dot{v}_x = 0$, one can see the range where turning points happen, and after that, τ can be found. This would make it possible to work with second-order basis functions in the fully optimised code exploiting piece-wise analytical trajectories.

The feature that is most straightforward to add is kinetic electrons. In that case, the electrons will be described by their own distribution function $f_e(x, v_x, v_y, v_z)$. The electron density will then be calculated similarly to the ion density. The updating scheme for the potential will stay the same, the only difference is that $n_e = \int d^3\mathbf{v} f_e$ instead of $n_\infty e^{\frac{e\phi}{kT_e}}$. It should be noted that the electron particle trajectories need to be resolved. Straightforwardly doing this would slow down the code. It would require the electron-gyro-frequency time-scale to be resolved. This would be counterproductive because the goal of the code is to be efficient. There are two ways in which adding kinetic electrons will not slow down the code. First, piece-wise analytical trajectories can be calculated for the electrons as well. In that case, resolving the electron cyclotron frequency is not needed. If the piece-wise analytical trajectories are not used, one can use a scheme that conserves the gyro-motion. An example of such a scheme is the Boris' integration [59], which has been shown to conserve the guiding center motion for large $\omega_{ce}\Delta T$ i.e. time steps that do not resolve the electron cyclotron frequency [60]. However, Boris' algorithm cannot be used without equidistant time stepping. Adaptive time stepping is an important feature of the numerical method that was discussed in this report. The code needs to resolve the Debye sheath time scales in the Debye sheath, and it shouldn't resolve these timescales in the magnetic presheath. A solution could be the Crank-Nicolson method, which will also conserve energy and the electron cyclotron orbit [61], [62]. However, the scheme is implicit: it requires an iterative procedure to obtain mid-point field values [63]. Adding kinetic electrons has the big advantage that it will allow for calculation of the electron current. It is then possible to make a scheme that updates the potential in such a way that the boundary condition of the potential at the wall is determined by the ambipolarity condition. This would make it possible to find the self-consistent field that satisfies ambipolarity, something that was not possible with the implementation of the code up to now.

Then it is possible to add spatial dimensions to the code, to simulate a system that is either 2D3V or even 3D3V. This would have multiple possible applications. It would be possible to simulate surface roughness the wall could be described as a function of the other variables such that $x_{wall} = g(z, y)$ describes the location of the wall in x as a function of y and z . Another possibility would be to simulate other geometries, for example, a probe system. Probes are used to do measurements in the plasma boundary layer. Something else would be to add turbulence. This can be done by adding a turbulent electric field in the y ($\mathbf{E} \times \mathbf{B}$) direction. It would be most interesting to look at turbulence in the $\mathbf{E} \times \mathbf{B}$ direction because a weak electric field in that direction could pull or push particles towards or away from the wall. PIC codes can also do these simulations, but it would take a lot more time to simulate these systems. Note that adding dimensions increases the computational time of the system. If there are n_z grid points in the z -direction and n_y grid points in the y -direction, then the computational time is increased by a factor of $n_z \times n_y$. Something else that should be noted is that by adding another dimension the symmetry in the system is broken. This means that $\nabla^2\phi \neq \frac{d^2\phi}{dx^2}$, and thus there is no guarantee that the iterative scheme used in this report will work. It might be the case that another iterative scheme has to be devised. Lastly, new boundary conditions have to be included in the dimensions that were added.

It is also possible to add multiple ion species, this means that Poisson's equation has to be written as:

$$\epsilon_0 \frac{d^2\phi}{dx^2} = -e \left(\sum_s Z_s \int f_s(x, \mathbf{v}) d^3\mathbf{v} - \int f_e(x, \mathbf{v}) d^3\mathbf{v} \right). \quad (6.1)$$

Where \sum_s indicates a sum over all ion species. It is important to add multiple ion species because the magnetised sheath region in a fusion reactor contains deuterium, tritium and several impurity species. The energy threshold for sputtering and the sputtering yield depends on the ion species and the angle of incidence of the ions [64]. Sputtering by impurities usually has a lower kinetic energy threshold than sputtering by the main ion species [65], and therefore it is especially important to understand the velocity distribution at the target for impurities. Adding the distribution functions is straightforward, but the particle trajectories of each ion species have to be integrated towards the wall. The code will be slowed down by a factor that scales with the number of ion species.

Lastly, one could add collisions. For example, Coulomb collisions between multiple ion species or charge exchange collisions between ions and neutrals could be simulated in the magnetised sheath system. Since the same \mathbf{v}_∞ will not necessarily lead to the same \mathbf{v}_0 depending on the collisions, it would probably mean that the number of particles that need to be sampled will have to be increased.

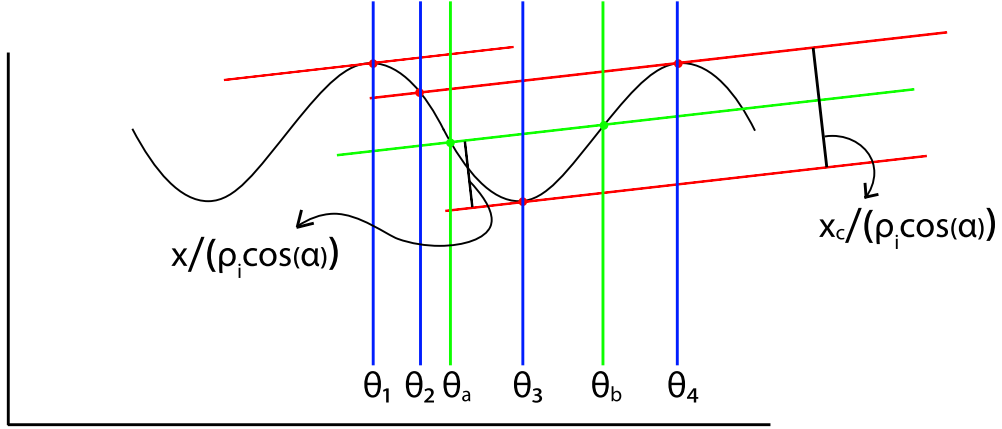


Figure A.1: Schematic drawing for calculating gyroring density contribution. The linear parallel lines are the critical intersections of the wall at different times, such that it encompasses one entire gyroring. The gyrophase angles at which these intersections happen are denoted by $\theta_1, \theta_2, \theta_3$ and θ_4 . The green line is the intersection at a certain position x with the wall. Then there will be gyrophase angles θ_a and θ_b , such that $\theta \in [\theta_a, \theta_b]$ already have intersected with the wall.

A Density Contribution Single Gryo-Ring

To benchmark the code it is useful to first look at the density contribution of something that can be calculated analytically for all angles α . In this case it was chosen to look at the density contribution of a single gyroring in a potential field $\phi(x) = 0$. In light of the numerical method this is given by:

$$M^{\alpha\beta} \mathcal{N}_{i,gyro}^{\alpha} = \frac{1}{2\pi} \int_0^{2\pi} d\theta_{\infty} \int_0^{\tau_i} dt v_{x,\infty} \Lambda(x(t, \theta_{\infty})). \quad (\text{A.1})$$

Analytically the density can be calculated by looking at which fraction of the gyroring is occupied. Let us look first at the case where $\alpha < \lambda$. Before particles start hitting the wall, all particles are still in the system and thus the entire gyroring is completely filled with particles meaning that before particles hit the wall, $n_i(x) = n_{i,\infty}$. When particles hit the wall, some gyro-angles start to become empty because at that angle the particle has hit the wall already. Remember that for a given angle α the particle trajectory in a flat potential is given by Equation 3.26. Thus the gyrophase angle at a given time is just given by $\theta(t) = \Omega t + \theta_0$. So we can rewrite Equation 3.26:

$$x(\theta) = \frac{v_{\perp}}{\Omega} \cos(\alpha) [\sin(\theta) - \sin(\theta_0)] - a\theta + b. \quad (\text{A.2})$$

Here a and b are constants, $a = \sin(\alpha) \frac{v_{\perp}}{\Omega}$ and $b = x_{\infty} - \sin(\alpha) \frac{v_{\perp}}{\Omega} \theta_0$. Rewriting it like this highlights that the problem can be viewed as a particle moving in a sinusoidal function in θ while the wall is moving towards it as a linear function. See Figure A.1 for a reference. The red line indicates the wall moving towards the particle intersecting with the curve at different angles. And the black line indicates the particles gyrating around the magnetic field line. Note that in particular the black line is just $\frac{v_{\perp}}{\Omega} \cos(\alpha) [\sin(\theta) - \sin(\theta_0)]$ (the sinusoidal part of Equation A.2) and the red line is just $-a\theta + b$ the linear part of Equation A.2. The blue lines indicate intersections of and the sinusoidal curve at important locations. The locations are defined by the lowest and highest points on the sinusoidal where the red lines start to intersect with the black curve. This happens when the red line is tangent to the black line. The lowest point where that happens indicates when particles start hitting the wall. Meaning θ_3 is the gyrophase where the first particles start hitting the wall, this happens at some distance x_c from the wall. Note that when the particles start hitting the wall, the gyroring starts to empty for $\theta < \theta_3$ and $\theta > \theta_3$ simultaneously. But graphically it happens by moving the red line upwards in the direction perpendicular to its slope. The gyrophase when the particle hits the wall will be the highest point of intersection which is θ_4 , the gyrophase on the other side of θ_3 will then be θ_2 . The gyroring from θ_2 to θ_4 has been emptied. Thus x_c can be calculated using $x_c = x(\theta_4) - x(\theta_3)$:

$$\frac{x_c}{\rho_i \cos(\alpha)} = \sin(\theta_4) - \left[\sin(\theta_3) + \tan(\alpha) \frac{v_{\perp}}{\Omega} (\theta_4 - \theta_3) \right]. \quad (\text{A.3})$$

Here $\rho_i = \frac{v_\perp}{\Omega}$ was used. This equation can be solved for x_c , to do this first note that $\theta_4 = \theta_1 + 2\pi$, and that $\theta_3 - 2\pi = 2\theta_1$. This should be clear from Figure A.1 and the fact that θ_4 and θ_1 are exactly one phase away from each other, θ_3 will be exactly half a phase away from θ_4 and θ_1 . One obtains:

$$\frac{x_c}{\rho_i \cos(\alpha)} = \sin(\theta_1) - \sin(\theta_3) - \tan(\alpha) \frac{v_\parallel}{v_\perp} (2\theta_1). \quad (\text{A.4})$$

Now note that since the red line touches the black curve at θ_3 and θ_1 and thus their derivatives with respect to θ should be equal, i.e. $\cos(\theta_{1,3}) = \tan(\alpha) \frac{v_\parallel}{v_\perp}$. Using this one obtains finally:

$$\frac{x_c}{\rho_i} = 2\sqrt{1 - \tan^2(\alpha) \left(\frac{v_\parallel}{v_\perp} \right)^2} - 2 \tan(\alpha) \frac{v_\parallel}{v_\perp} \arccos \left(\tan(\alpha) \frac{v_\parallel}{v_\perp} \right) \quad (\text{A.5})$$

This gives the location x where the gyroring starts to empty. This in turn means that $n_i(x) = 1$ for $x < x_c$.

Now for the region when $0 \leq n(x) \leq 1$, then there particle is in an intermediate range, this is denoted by the green lines. In the green lines the gyrophase from θ_a to θ_b have already intersected with the wall. This happens at some location x and thus one can write x as a function of θ_a or θ_b :

$$\sin(\theta_{a,b}) - \tan(\alpha) \frac{v_\parallel}{v_\perp} \theta_{a,b} = \sin(\theta_3) - \tan(\alpha) \frac{v_\parallel}{v_\perp} \theta_3 + \frac{x}{\rho_i \cos(\alpha)} \quad (\text{A.6})$$

At this point all gyrophases from θ_a to θ_b have been emptied, and thus the density fraction has been reduced by a fraction of $1 - \frac{\theta_b - \theta_a}{2\pi}$. This gives semi analytical solution for the density of a single gyroring without an electric field:

$$n_i(x) = \begin{cases} n_\infty & \text{for } x > x_c \\ n_\infty \left(1 - \frac{\theta_b - \theta_a}{2\pi}\right) & \text{for } x \leq x_c \end{cases} \quad (\text{A.7})$$

Where θ_a and θ_b are calculated by solving Equation A.6 under the condition that $\theta_a \in [\theta_2, \theta_3]$ and $\theta_b \in [\theta_3, \theta_4]$. Now if $\alpha > \lambda$ note already that the equation for x_c does not have a solution because $\theta(\theta_{1,3}) = \frac{\tan(\alpha)}{\tan(\lambda)} > 1$. So there is no case where the linear curve is tangent to the sinusoidal curve. This means that the gyroring remains filled up to the wall and thus $n_i(x) = 1$ for $x \in [0, x_\infty]$. This concludes the analytical calculation of the density of a gyroring in the case that there is no electric field.

References

- [1] IPCC. ‘2021: Summary for Policymakers.’ In: *In: Climate Change 2021: The Physical Science Basis. Contribution of Working Group I to the Sixth Assessment Report of the Intergovernmental Panel on Climate Change*. Ed. by V.P. Zhai (eds.) Masson-Delmotte. Cambridge, United Kingdom and New York, NY, USA: Cambridge University Press, 2021. Chap. SPM, pp. 1–39.
- [2] Mike Berners-Lee. In: *There Is No Planet B: A Handbook for the Make or Break Years*. Cambridge University Press, 2019.
- [3] Barry W. Brook et al. ‘Why nuclear energy is sustainable and has to be part of the energy mix’. In: *Sustainable Materials and Technologies* 1-2 (2014), pp. 8–16. ISSN: 2214-9937. DOI: <https://doi.org/10.1016/j.susmat.2014.11.001>. URL: <https://www.sciencedirect.com/science/article/pii/S2214993714000050>.
- [4] Jeffrey P. Freidberg. *Plasma Physics and Fusion Energy*. Cambridge University Press, 2007. DOI: [10.1017/CBO9780511755705](https://doi.org/10.1017/CBO9780511755705).
- [5] Mitsuru Kikuchi et al. *Fusion physics*. International Atomic Energy Agency, 2012.
- [6] N. J. Lopes Cardozo. *Fusion reactors: extreme materials, intense plasma-wall interaction*. unpublished, 2017.
- [7] Alessandro Geraldini. ‘Kinetic treatment of magnetized and collisionless plasma near a wall’. PhD thesis. Merton College University of Oxford, 2018.
- [8] F. Jenko and The GENE development team. *The gene code*. URL: <https://genecode.org/>.
- [9] K -U Riemann. ‘The Bohm criterion and sheath formation’. In: *Journal of Physics D: Applied Physics* 24.4 (Apr. 1991), pp. 493–518. DOI: [10.1088/0022-3727/24/4/001](https://doi.org/10.1088/0022-3727/24/4/001). URL: <https://doi.org/10.1088/0022-3727/24/4/001>.
- [10] David Bohm. *The characteristics of electrical discharge in Magnetic Fields*. McGraw-Hill, 1949.
- [11] E R Harrison and W B Thompson. ‘The Low Pressure Plane Symmetric Discharge’. In: *Proceedings of the Physical Society* 74.2 (Aug. 1959), pp. 145–152. DOI: [10.1088/0370-1328/74/2/301](https://doi.org/10.1088/0370-1328/74/2/301). URL: <https://doi.org/10.1088/0370-1328/74/2/301>.
- [12] R. Chodura. ‘Plasma-wall transition in an oblique magnetic field’. In: *Physics of Fluids* 25.9 (Sept. 1982), pp. 1628–1633. DOI: [10.1063/1.863955](https://doi.org/10.1063/1.863955).
- [13] Alessandro Geraldini, Felix Parra and Fulvio Militello. ‘Gyrokinetic treatment of a grazing angle magnetic field’. In: *Plasma Physics and Controlled Fusion* 59 (Aug. 2017). DOI: [10.1088/1361-6587/59/2/025015](https://doi.org/10.1088/1361-6587/59/2/025015).
- [14] A Geraldini, F I Parra and F Militello. ‘Solution to a collisionless shallow-angle magnetic presheath with kinetic ions’. In: *Plasma Physics and Controlled Fusion* 60.12 (Oct. 2018), p. 125002. ISSN: 1361-6587. DOI: [10.1088/1361-6587/aae29f](https://doi.org/10.1088/1361-6587/aae29f). URL: <http://dx.doi.org/10.1088/1361-6587/aae29f>.
- [15] T.M. Tran et al. ‘DAPHNE, a 2D axisymmetric electron gun simulation code’. In: (1994).
- [16] M. Martinez-Sanchez and J. E. Pollard. ‘Spacecraft Electric Propulsion-An Overview’. In: *Journal of Propulsion and Power* 14.5 (1998), pp. 688–699. DOI: [10.2514/2.5331](https://doi.org/10.2514/2.5331). eprint: <https://doi.org/10.2514/2.5331>. URL: <https://doi.org/10.2514/2.5331>.
- [17] I. H. Hutchinson. *Principles of Plasma Diagnostics*. 2nd ed. Cambridge University Press, 2002. DOI: [10.1017/CBO9780511613630](https://doi.org/10.1017/CBO9780511613630).
- [18] A. Anders, S. Anders and I. Brown. ‘Transport of vacuum arc plasmas through magnetic macro-particle filters’. In: *Plasma Sources Science and Technology* 4 (1995), pp. 1–12.
- [19] J D Lawson. ‘Some Criteria for a Power Producing Thermonuclear Reactor’. In: *Proceedings of the Physical Society. Section B* 70.1 (Jan. 1957), pp. 6–10. DOI: [10.1088/0370-1301/70/1/303](https://doi.org/10.1088/0370-1301/70/1/303). URL: <https://doi.org/10.1088/0370-1301/70/1/303>.
- [20] Michael A. Lieberman and Allan J. Lichtenberg. ‘Principles of Plasma Discharges and Materials Processing: Lieberman/Plasma 2e’. In: 2005.
- [21] Francis F Chen et al. *Introduction to plasma physics and controlled fusion*. Vol. 1. Springer, 1984.
- [22] Lewi Tonks and Irving Langmuir. ‘Oscillations in Ionized Gases’. In: *Phys. Rev.* 33 (2 Feb. 1929), pp. 195–210. DOI: [10.1103/PhysRev.33.195](https://doi.org/10.1103/PhysRev.33.195). URL: <https://link.aps.org/doi/10.1103/PhysRev.33.195>.
- [23] J. W. Cipolla and M. B. Silevitch. ‘On the temporal development of a plasma sheath’. In: *Journal of Plasma Physics* 25.3 (1981), pp. 373–389. DOI: [10.1017/S0022377800026179](https://doi.org/10.1017/S0022377800026179).

- [24] K-U Riemann. ‘Kinetic analysis of the collisional plasma–sheath transition’. In: *Journal of Physics D: Applied Physics* 36.22 (Oct. 2003), pp. 2811–2820. DOI: [10.1088/0022-3727/36/22/007](https://doi.org/10.1088/0022-3727/36/22/007). URL: <https://doi.org/10.1088/0022-3727/36/22/007>.
- [25] K-U Riemann et al. ‘The plasma–sheath matching problem’. In: *Plasma Physics and Controlled Fusion* 47.11 (Oct. 2005), pp. 1949–1970. DOI: [10.1088/0741-3335/47/11/006](https://doi.org/10.1088/0741-3335/47/11/006). URL: <https://doi.org/10.1088/0741-3335/47/11/006>.
- [26] Davison E. Soper. *Classical field theory / Davison E. Soper*. English. Wiley New York, 1976. ISBN: 0471813680.
- [27] V.I. Arnold. *Mathematical methods of classical mechanics*. Vol. 60. Springer, 1989.
- [28] L.P. Pitaevskii and E.M. Lifshitz. *Physical Kinetics: Volume 10*. v. 10. Elsevier Science, 2012. ISBN: 9780080570495. URL: <https://books.google.nl/books?id=DTHxPDfV0fQC>.
- [29] Richard L. Liboff. *Kinetic theory : classical, quantum, and relativistic descriptions*. 2003.
- [30] F. F. Chen. *Introduction to plasma physics*. New York: Plenum Press, 1974.
- [31] P.C. Stangeby and J. E. Allen. ‘Plasma boundary as a Mach surface’. In: *Journal of Physics A: General Physics* 3 (1970), pp. 304–308.
- [32] J. Andrews and P. G. Stangeby. ‘Generalization of the sheath criterion in an anisotropic plasma’. In: *Journal of Physics A: General Physics* 3 (1970).
- [33] C.-D. Munz. ‘A tracking method for gas flow into vacuum based on the vacuum Riemann problem’. In: *Mathematical Methods in the Applied Sciences* 17.8 (1994), pp. 597–612. DOI: <https://doi.org/10.1002/mma.1670170803>. eprint: <https://onlinelibrary.wiley.com/doi/pdf/10.1002/mma.1670170803>. URL: <https://onlinelibrary.wiley.com/doi/abs/10.1002/mma.1670170803>.
- [34] K.-U. Riemann. ‘Kinetic theory of the plasma sheath transition in a weakly ionized plasma’. In: *The Physics of Fluids* 24.12 (1981), pp. 2163–2172. DOI: [10.1063/1.863332](https://doi.org/10.1063/1.863332). eprint: <https://aip.scitation.org/doi/pdf/10.1063/1.863332>. URL: <https://aip.scitation.org/doi/abs/10.1063/1.863332>.
- [35] K.-U. Riemann. ‘Theory of the collisional presheath in an oblique magnetic field’. In: *Physics of Plasmas* 1 (1994), pp. 552–558.
- [36] A Loarte et al. ‘Chapter 4: Power and particle control’. In: *Nuclear Fusion* 47.6 (June 2007), S203–S263. DOI: [10.1088/0029-5515/47/6/s04](https://doi.org/10.1088/0029-5515/47/6/s04). URL: <https://doi.org/10.1088/0029-5515/47/6/s04>.
- [37] Susanne C. Brenner and Larkin R. Scott. *The Mathematical Theory of Finite Element Methods*. Vol. 15. Texts in Applied Mathematics. Springer, 2008. ISBN: 9780387759333. DOI: [10.1007/978-0-387-75934-0](https://doi.org/10.1007/978-0-387-75934-0). URL: <http://dx.doi.org/10.1007/978-0-387-75934-0>.
- [38] T.J.R. Hughes. *The Finite Element Method: Linear Static and Dynamic Finite Element Analysis*. Dover Civil and Mechanical Engineering. Dover Publications Incorporated, 2003. ISBN: 9780486411811. URL: <https://books.google.nl/books?id=E9IoAwAAQBAJ>.
- [39] C. de Boor. *A Practical Guide to Splines*. Applied Mathematical Sciences. Springer New York, 2001. ISBN: 9780387953663. URL: https://books.google.nl/books?id=m0QDJvBI%5C_ecC.
- [40] Christian Terboven and Michael Klemm. *Programming OpenMP An Overview Of OpenMP*. Jan. 2021. URL: https://indico.euro-fusion.org/event/688/attachments/854/1856/OpenMP_Webinar_1_2021-01-27.pdf.
- [41] William H. Press et al. *Numerical Recipes in C (2nd Ed.): The Art of Scientific Computing*. USA: Cambridge University Press, 1992. ISBN: 0521431085.
- [42] Marcia Ascher. ‘Cycling in the Newton-Raphson Algorithm’. In: *International Journal of Mathematical Education in Science and Technology* 5.2 (1974), pp. 229–235. DOI: [10.1080/0020739740050213](https://doi.org/10.1080/0020739740050213). eprint: <https://doi.org/10.1080/0020739740050213>. URL: <https://doi.org/10.1080/0020739740050213>.
- [43] David Coulette and Giovanni Manfredi. ‘Kinetic simulations of the Chodura and Debye sheaths for magnetic fields with grazing incidence’. In: *Plasma Physics and Controlled Fusion* 58.2 (Jan. 2016), p. 025008. DOI: [10.1088/0741-3335/58/2/025008](https://doi.org/10.1088/0741-3335/58/2/025008). URL: <https://doi.org/10.1088/0741-3335/58/2/025008>.
- [44] Alessandro Geraldini. ‘Large gyro-orbit model of ion velocity distribution in plasma near a wall in a grazing-angle magnetic field’. In: *Journal of Plasma Physics* 87.1 (2021), p. 905870113. DOI: [10.1017/S002237782000166X](https://doi.org/10.1017/S002237782000166X).
- [45] S Devaux and G Manfredi. ‘Magnetized plasma–wall transition—consequences for wall sputtering and erosion’. In: *Plasma Physics and Controlled Fusion* 50.2 (Jan. 2008), p. 025009. DOI: [10.1088/0741-3335/50/2/025009](https://doi.org/10.1088/0741-3335/50/2/025009). URL: <https://doi.org/10.1088/0741-3335/50/2/025009>.

- [46] Rinat Khaziev and Davide Curreli. ‘Ion energy-angle distribution functions at the plasma-material interface in oblique magnetic fields’. In: *Physics of Plasmas* 22 (Apr. 2015), p. 043503. DOI: [10.1063/1.4916910](https://doi.org/10.1063/1.4916910).
- [47] C.Z Cheng and Georg Knorr. ‘The integration of the vlasov equation in configuration space’. In: *Journal of Computational Physics* 22.3 (1976), pp. 330–351. ISSN: 0021-9991. DOI: [https://doi.org/10.1016/0021-9991\(76\)90053-X](https://doi.org/10.1016/0021-9991(76)90053-X). URL: <https://www.sciencedirect.com/science/article/pii/002199917690053X>.
- [48] A Ghizzo et al. ‘A Vlasov code for the numerical simulation of stimulated raman scattering’. In: *Journal of Computational Physics* 90.2 (1990), pp. 431–457. ISSN: 0021-9991. DOI: [https://doi.org/10.1016/0021-9991\(90\)90174-Y](https://doi.org/10.1016/0021-9991(90)90174-Y). URL: <https://www.sciencedirect.com/science/article/pii/002199919090174Y>.
- [49] M. Shoucri and R. Gagné. ‘Splitting schemes for the numerical solution of a two-dimensional Vlasov equation’. In: *Journal of Computational Physics* 27 (1978), pp. 315–322.
- [50] F Militello and W Fundamenski. ‘Multi-machine comparison of drift fluid dimensionless parameters’. In: *Plasma Physics and Controlled Fusion* 53.9 (July 2011), p. 095002. DOI: [10.1088/0741-3335/53/9/095002](https://doi.org/10.1088/0741-3335/53/9/095002). URL: <https://doi.org/10.1088/0741-3335/53/9/095002>.
- [51] Wolfgang Eckstein. ‘Sputtering Yields’. In: *Sputtering by Particle Bombardment: Experiments and Computer Calculations from Threshold to MeV Energies*. Berlin, Heidelberg: Springer Berlin Heidelberg, 2007, pp. 33–187. ISBN: 978-3-540-44502-9. DOI: [10.1007/978-3-540-44502-9_3](https://doi.org/10.1007/978-3-540-44502-9_3). URL: https://doi.org/10.1007/978-3-540-44502-9_3.
- [52] L. Chen et al. ‘Sputtering of the beryllium tungsten alloy Besub2/subW by deuterium atoms: molecular dynamics simulations using machine learned forces’. In: *Nuclear Fusion* 61.1 (Dec. 2020), p. 016031. DOI: [10.1088/1741-4326/abc9f4](https://doi.org/10.1088/1741-4326/abc9f4). URL: <https://doi.org/10.1088/1741-4326/abc9f4>.
- [53] H. L. Bay and J. Bohdansky. ‘Sputtering yields for light ions as a function of angle of incidence’. In: *Applied Physics* 19.4 (Aug. 1979), pp. 421–426. DOI: [10.1007/bf00930106](https://doi.org/10.1007/bf00930106). URL: <https://doi.org/10.1007/bf00930106>.
- [54] W. Ensinger. ‘An apparatus for sputter coating the inner walls of tubes’. In: *Review of Scientific Instruments* 67.1 (Jan. 1996), pp. 318–321. DOI: [10.1063/1.1146588](https://doi.org/10.1063/1.1146588). URL: <https://doi.org/10.1063/1.1146588>.
- [55] Andrew H. Simon. ‘4 - Sputter Processing’. In: *Handbook of Thin Film Deposition (Third Edition)*. Ed. by Krishna Seshan. Third Edition. Oxford: William Andrew Publishing, 2012, pp. 55–88. ISBN: 978-1-4377-7873-1. DOI: <https://doi.org/10.1016/B978-1-4377-7873-1.00004-8>. URL: <https://www.sciencedirect.com/science/article/pii/B9781437778731000048>.
- [56] I. Bykov et al. ‘Studies of Be migration in the JET tokamak using AMS with 10 Be marker’. In: *Nuclear Instruments and Methods in Physics Research Section B: Beam Interactions with Materials and Atoms* 371 (Mar. 2016), pp. 370–375. DOI: [10.1016/j.nimb.2015.12.007](https://doi.org/10.1016/j.nimb.2015.12.007). URL: <https://doi.org/10.1016/j.nimb.2015.12.007>.
- [57] G. Manfredi and F. Valsaque. ‘Vlasov simulations of plasma-wall interactions in a weakly collisional plasma’. In: *Computer Physics Communications* 164.1 (2004). Proceedings of the 18th International Conference on the Numerical Simulation of Plasmas, pp. 262–268. ISSN: 0010-4655. DOI: <https://doi.org/10.1016/j.cpc.2004.06.037>. URL: <https://www.sciencedirect.com/science/article/pii/S0010465504002905>.
- [58] S. Devaux and G. Manfredi. ‘Vlasov simulations of plasma-wall interactions in a magnetized and weakly collisional plasma’. In: *Physics of Plasmas* 13.8 (Aug. 2006), p. 083504. DOI: [10.1063/1.2244533](https://doi.org/10.1063/1.2244533). URL: <https://doi.org/10.1063/1.2244533>.
- [59] Jay P Boris et al. ‘Relativistic plasma simulation-optimization of a hybrid code’. In: *Proc. Fourth Conf. Num. Sim. Plasmas*. 1970, pp. 3–67.
- [60] S.E Parker and C.K Birdsall. ‘Numerical error in electron orbits with large $\omega_{ce}\Delta t$ ’. In: *Journal of Computational Physics* 97.1 (Nov. 1991), pp. 91–102. DOI: [10.1016/0021-9991\(91\)90040-r](https://doi.org/10.1016/0021-9991(91)90040-r). URL: [https://doi.org/10.1016/0021-9991\(91\)90040-r](https://doi.org/10.1016/0021-9991(91)90040-r).
- [61] G. Chen and L. Chacón. ‘An energy- and charge-conserving, nonlinearly implicit, electromagnetic 1D-3V Vlasov–Darwin particle-in-cell algorithm’. In: *Computer Physics Communications* 185.10 (Oct. 2014), pp. 2391–2402. DOI: [10.1016/j.cpc.2014.05.010](https://doi.org/10.1016/j.cpc.2014.05.010). URL: <https://doi.org/10.1016/j.cpc.2014.05.010>.
- [62] G. Chen and L. Chacón. ‘A multi-dimensional, energy- and charge-conserving, nonlinearly implicit, electromagnetic Vlasov–Darwin particle-in-cell algorithm’. In: *Computer Physics Communications*

- 197 (Dec. 2015), pp. 73–87. DOI: [10.1016/j.cpc.2015.08.008](https://doi.org/10.1016/j.cpc.2015.08.008). URL: <https://doi.org/10.1016/j.cpc.2015.08.008>.
- [63] T. C. Genoni, R. E. Clark and D. R. Welch. ‘A Fast Implicit Algorithm for Highly Magnetized Charged Particle Motion’. In: *The Open Plasma Physics Journal* 3.1 (May 2014), pp. 36–41. DOI: [10.2174/1876534301003010036](https://doi.org/10.2174/1876534301003010036). URL: <https://doi.org/10.2174/1876534301003010036>.
- [64] W. Eckstein et al. ‘Threshold energy for sputtering and its dependence on angle of incidence’. In: *Nuclear Instruments and Methods in Physics Research Section B: Beam Interactions with Materials and Atoms* 83.1-2 (Oct. 1993), pp. 95–109. DOI: [10.1016/0168-583x\(93\)95913-p](https://doi.org/10.1016/0168-583x(93)95913-p). URL: [https://doi.org/10.1016/0168-583x\(93\)95913-p](https://doi.org/10.1016/0168-583x(93)95913-p).
- [65] N Mellet et al. ‘Magnetic sheath effect on the gross and net erosion rates due to impurities’. In: *Physica Scripta* T167 (Jan. 2016), p. 014064. DOI: [10.1088/0031-8949/t167/1/014064](https://doi.org/10.1088/0031-8949/t167/1/014064). URL: <https://doi.org/10.1088/0031-8949/t167/1/014064>.